

# MicroBooNE

---

**A.N. Author<sup>1</sup>**

<sup>1</sup>*Institution 1, City, State 12345*

**ABSTRACT:** This paper describes the design and construction of the MicroBooNE liquid argon time projection chamber and associated systems. Details of design specifications, assembly procedures, and acceptance tests are reported.

**KEYWORDS:** Time projection chambers; Noble-liquid detectors; Data analysis.

---

## Contents

<b>1. Introduction and Physics Motivation</b>	<b>3</b>
<b>2. Experiment Overview</b>	<b>5</b>
2.1 The LArTPC Technique	6
2.2 MicroBooNE LArTPC Implementation	8
<b>3. Cryogenic System</b>	<b>9</b>
3.1 Cryostat Design Overview	10
3.2 Liquid Argon Purification Subsystem	12
3.3 Nitrogen Refrigeration	15
3.4 Controls and Purity Monitoring	16
<b>4. Liquid Argon Time Projection Chamber</b>	<b>17</b>
4.1 Cathode	18
4.2 Field Cage	19
4.2.1 Resistor Divider Chain	21
4.3 Anode	26
4.3.1 Mechanical structure	26
4.3.2 Wire winding and quality assurance	26
4.3.3 Wire installation and tension measurements	28
4.4 Parts Preparation	28
4.4.1 Cleaning stainless steel	29
4.4.2 Cleaning G-10	30
4.5 Assembly	31
4.6 High Voltage System	31
<b>5. Light Collection System</b>	<b>33</b>
5.1 Motivation and General Design	34
5.2 The Primary Light Collection System	38
5.2.1 Photomultiplier Tubes and Bases	39
5.2.2 Wavelength-Shifting Plates	41
5.2.3 UV Light Protection for the Wavelength-Shifting Plates	42
5.2.4 Cryogenic Mu Metal Shields	43
5.2.5 Implementation of the Primary System	45
5.3 The Bo Vertical Slice Tests	46
5.4 Acrylic Light Guides as a Secondary System for R&D	47
5.5 Flasher System	49
5.6 Testing Coupling of PMT Signals to the Anode Wires	51
5.7 Initial Performance of the MicroBooNE Light Collection System	51

<b>6. Electronics and Readout Systems</b>	<b>52</b>
6.1 Cryogenic Low-Noise Electronics	52
6.1.1 CMOS ASIC	52
6.1.2 Cold Motherboards	55
6.1.3 Cold Cables	56
6.1.4 Electronic Calibration	57
6.1.5 Performance Tests	57
6.2 Warm Electronic Amplification	58
6.3 LArTPC Readout Electronics	60
6.3.1 LArTPC Data Digitization	61
6.3.2 LArTPC Data Handling	61
6.3.3 LArTPC Compression Schemes	63
6.4 PMT Readout Electronics	64
6.4.1 Signal Amplification and Shaping	66
6.4.2 PMT Data Digitization	67
6.4.3 Data Handling and PMT Trigger Generation	67
6.5 Level-1 Trigger Generation	68
6.6 DAQ Design	69
6.7 High-level software trigger	73
<b>7. Infrastructure and Monitoring Systems</b>	<b>73</b>
7.1 Electronics Infrastructure at LArTF	74
7.1.1 AC Power Distribution and Grounding for Low-Noise LArTF Data-taking	74
7.1.2 DC Power Distribution to the MicroBooNE Detector	77
7.1.3 Network, Timing, and Data Distribution for Low-Noise LArTF Data-taking	78
7.1.4 Interlocks and Safety Systems	78
7.1.5 Performance Measurements	79
7.2 Slow monitoring and control system	79
7.3 Beam Monitoring	80
<b>8. UV Laser System</b>	<b>82</b>
8.1 UV Laser Calibration	84
8.2 Laser Source and Optics	84
8.3 Steering System	86
8.4 Performance Tests and Initial Operation	87
<b>9. Conclusion</b>	<b>88</b>

---

<sup>1</sup> Date: June 17, 2016; Paper Version: 1.0

## 1. Introduction and Physics Motivation

2 Neutrino detection is entering a new era with a number of large precision neutrino detectors, specifically  
3 Liquid Argon Time Projection Chambers (LArTPCs), now in design and construction both for  
4 long and short baseline neutrino oscillation experiments. The **Micro Booster Neutrino Experiment**,  
5 henceforth referred to as MicroBooNE, will be the first large ( $\sim 100$  tons) LArTPC to operate in the  
6 United States and the second only after ICARUS to operate worldwide. LArTPC detectors com-  
7 bine fine-grained tracking with total absorption calorimetry to provide excellent signal efficiency  
8 and background rejection.

9 The MicroBooNE experiment combines physics goals of short-baseline oscillations and neu-  
10 trino cross-section measurements with development goals to inform larger scale construction of  
11 LArTPCs for the long-baseline program. MicroBooNE's principal physics goal is to address long  
12 standing unsolved puzzles generated by short-baseline neutrino oscillation results from past exper-  
13 iments. The LSND collaboration measured an oscillation rate of antimuon neutrinos to antielectron  
14 neutrinos not compatible with the solar or atmospheric oscillation parameters [?]. The size of the  
15 observed signal suggests a mass squared difference of neutrino masses of the order of about 1 eV,  
16 which could only be accommodated with an additional neutrino mass eigenstate. Since the weak  
17 interaction only couples to three neutrino eigenstates, an additional neutrino is called sterile, i.e.  
18 not coupling to other fermions except via the oscillation mechanism.

19 Other hints come from a re-analysis of the expected reactor antineutrino flux that suggests a  
20 deficit of reactor neutrinos [?], and the analysis of calibration data taken by GALLEX and SAGE  
21 [?]. The MiniBooNE experiment [?] also investigated (anti)muon- to (anti)electron-neutrino os-  
22 cillations and found a further significant deviation from the expectation in the number of electron  
23 (anti)neutrino candidates at low energy. The excess of electromagnetic-like events can be attributed  
24 to electrons or single photons since these are indistinguishable in the MiniBooNE Cerenkov imag-  
25 ing detector.

26 While each of the above results taken alone does not reach the statistical significance to claim  
27 a discovery, combining them together can provide indication for oscillations or other unexpected  
28 phenomena. Definitive evidence for sterile neutrinos would constitute a revolutionary discovery,  
29 with strong implications for particle physics as well as for cosmology. Proposals to address these  
30 signals by employing reactor, accelerator, and radioactive source experiments are in the planning  
31 stages or underway worldwide.

32 MicroBooNE will address this issue at Fermi National Accelerator Laboratory (Fermilab)  
33 with the same beam and baseline as MiniBooNE but by employing the LArTPC technology to  
34 efficiently separate electrons from photons. In addition to MicroBooNE's signature oscillation  
35 analyses, a suite of precision cross-section measurements will be performed, critical both for fu-  
36 ture LArTPC oscillation experiments and for what can be learned about neutrino interactions in  
37 general. In the energy range of interest, multiple interaction processes (quasi-elastic, resonances,  
38 deep inelastic scattering) are possible, and complicated nuclear effects in neutrino interactions on  
39 argon result in a variety of final states. These can range from the emission of several nucleons  
40 to more complex topologies with multiple pions, all in addition to the leading lepton in charged-  
41 current events. The LArTPC technology employed by MicroBooNE is particularly well suited to  
42 this purpose because of its excellent particle identification capability and calorimetric energy re-

1 construction down to very low detection thresholds. MicroBooNE will also be supernova live and  
2 capable of detecting a galactic supernova, and prepare the analysis of the search for proton decays.  
3 For the latter analysis the experiment will not have a competitive sensitivity due to too small target  
4 mass. However, this will be an important scientific goal towards future measurements in larger  
5 detectors.

6 On a longer time scale, a phased program is being pursued at Fermilab centered around the  
7 existing Booster Neutrino Beam (BNB) and the Neutrinos from the Main Injector (NuMI) beam.  
8 The MicroBooNE experiment is located 470 m from the BNB production target and 600 m from  
9 the NuMI production target. MicroBooNE began operations in late 2015 for a  $\sim$ 3 year time period,  
10 extending into the era of the full Short Baseline Neutrino (SBN) program beginning in 2018 with  
11 the commencement of operations of the SBND [?] and ICARUS experiments, located at 100m and  
12 600m respectively from the BNB production target. MicroBooNE will definitively address whether  
13 or not the MiniBooNE low energy excess in neutrino mode is due to electrons or photons. SBND  
14 will look for this low energy excess at the near location (100m) from the production target, and the  
15 three detectors combined will cover the entire LSND allowed region in neutrino parameter space  
16 to  $5\sigma$  through  $\nu_e$  appearance.

17 As mentioned above, the LArTPC technique will be used by MicroBooNE at a relatively  
18 large scale, so far only surpassed by the ICARUS T600 detector. The potential of liquified noble  
19 gases to be employed as the detection media in particle detectors with high spatial resolution was  
20 recognized already in the 1960's (see, e.g., Ref. [1]). Large calorimeters for the measurement of  
21 particle energy were then realized by using cryogenic noble liquids as active components (see, e.g.,  
22 Ref. [2]). Furthermore, the LArTPC was proposed at CERN by C. Rubbia in 1977 [3] as a detector  
23 capable of providing uniform and precise imaging of large volumes.

24 The original LArTPC idea was extensively developed by an intense ICARUS R&D program.  
25 Various prototype detectors were realized and operated to develop the systems needed for larger  
26 physics experiments such as purification methods, signal readout electronics, and cryogenics. The  
27 largest ICARUS test device had a mass of about 3 tons of LAr [4, 5] and allowed for the collection  
28 of large samples of cosmic-ray events. In parallel, a smaller volume detector (50 liters of LAr) was  
29 exposed to the CERN WANF neutrino beam allowing the detection of neutrino interaction events  
30 for the first time in a LArTPC [6].

31 The largest LArTPC detector built so far is the 600-ton ICARUS T600 detector, which was  
32 also tested with cosmic rays at the surface [7]. Measurements from this activity showed that the  
33 technique can successfully operate at large scales with a drift length as long as 1.5 m [8–12].  
34 The T600 was then moved to LNGS, and subsequently operated in the CNGS neutrino beam for a  
35 muon- to tau-neutrino oscillation search.

36 The success of the construction of the T600 motivated several follow up ideas aimed at reaching  
37 even higher target masses (see, e.g., Ref. [13]). A monolithic magnetized large mass device was  
38 proposed in [14], based on the scaling up of the ICARUS approach. The ICARUS experience led  
39 then to the broader development of the LArTPC concept. A LArTPC design envisioning a single  
40 cylindrical volume of 70 m diameter and 20 m height, called GLACIER, was discussed in [15, 16],  
41 based on a double-phase readout. This approach eventually evolved to the LAGUNA [17] proposal  
42 and to the LAGUNA LBNO [18, 19] conceptual design, aimed at a large detector placed along a  
43 long-baseline beam from CERN to an European underground site. A test device is currently under

1 construction at CERN, in the framework of the WA105 R&D project [20]. In the United States,  
2 an analogous multi-kton detector was proposed using conventional single-phase wire readout for  
3 the LBNE project [21], aimed at a long-baseline neutrino beam sent from Fermilab to the Sanford  
4 Laboratory in South Dakota.

5 In parallel, LArTPCs were also considered for short-baseline neutrino experiments, motivat-  
6 ing the use of relatively smaller size devices. A first proposal was submitted for the T2K neutrino  
7 beam [22, 23]. These ideas were backed by vigorous R&D programs still in progress in Bern [24 –  
8 27], at ETH Zurich [28 – 31], as well as in the United States [32]. At Fermilab, the first LArTPC to  
9 be successfully operated in the NuMI beam was the ArgoNeuT detector [33 – 37] that, despite the  
10 relatively small mass of  $\sim 170$  kg, has been able to perform a series of detailed studies on the inter-  
11 action of medium-energy neutrinos[?]. Other critical development projects are currently underway  
12 at Fermilab such as [38 – 42], all geared towards development of the technology and of analyzing  
13 particle interactions in the detectors. The goal of the development in the near term is towards the  
14 SBN program experiments, and in the farther term, following the recent recommendations of the  
15 P5 panel [43], the LBNF project and the DUNE experiment which envisions an internationally co-  
16 ordinated effort for the realization of an intense neutrino beam facility at Fermilab and a far large  
17 mass neutrino detector in a long-baseline configuration ( $> 1000$  km).

18 More information on the LArTPC technology can be found in existing reviews (see, e.g., [44]  
19 and references therein).

20 **Organization of Document** This document describes the design, construction, and technical de-  
21 tails of the MicroBooNE experiment. Section 2 gives a brief review of the LArTPC technique  
22 and its implementation in MicroBooNE. Section 3 describes the design and construction of the  
23 cryogenic and purification systems which are required for maintaining a stable volume of highly  
24 purified liquid argon. The LArTPC detector described in section 4 is the centerpiece of the experi-  
25 ment, providing fine-grained images of neutrino interactions. A light collection system, described  
26 in section 5, provides precise timing information by viewing the detector volume and recording  
27 signals from the scintillation light that is produced therein. Signals from the light collection system  
28 and from the LArTPC are amplified, sampled, and recorded by a custom-designed electronic and  
29 readout system, as described in section 6. Section 7 describes the auxiliary instrumentation that  
30 monitor and control the detector and all of its associated systems, as well as provide an electrically  
31 quiet environment for the experiment to operate. Finally, one of the main calibration sources for  
32 the experiment is an ultraviolet laser system, described in section 8, that provides the capability to  
33 map out the performance of the LArTPC detector.

## 34 2. Experiment Overview

35 MicroBooNE is hosted at Fermilab in Batavia, Illinois and is located on-axis to the BNB, which  
36 delivers a beam of predominantly muon-type neutrinos with energies peaking at 700 MeV. The  
37 characteristics of this beamline have been well-understood by MiniBooNE [45], which operates  
38 directly downstream of the MicroBooNE location. MicroBooNE will also record neutrino inter-  
39 actions from an off-axis component of the NuMI beamline [?]. Figure 1 shows the arrangement  
40 of MicroBooNE with respect to the BNB and NuMI beamlines at Fermilab. The physics program

1 of MicroBooNE will utilize both BNB and NuMI samples, as well as data collected out-of-time  
2 with either beam, which will be useful for developing analyses (e.g. development of proton decay  
3 searches) relevant for next-generation detectors. The primary detector technology employed by  
4 MicroBooNE is the LArTPC , whose operating principle is described in this section.

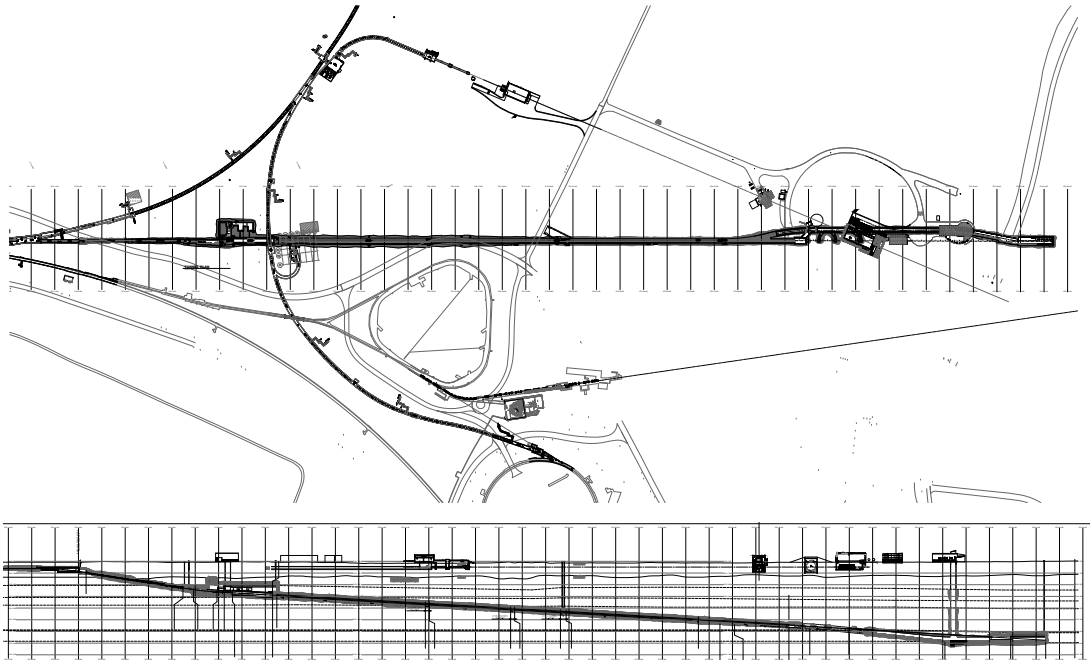


Figure 1: Plan (top) and cross-sectional (bottom) views of MicroBooNE. MicroBooNE is on-axis to the BNB, and off-axis to the NuMI beam.

## 5    2.1 The LArTPC Technique

6 In a LArTPC , charged particles traversing a volume of highly-purified liquid argon leave trails of  
7 ionization electrons in their wake and also create prompt vacuum ultraviolet (VUV) scintillation  
8 photons. The ionization trails are transported practically undistorted over distances of the order  
9 of meters [46] under the influence of a uniform electric field in the detector volume, until they  
10 reach anode planes located along one side of the active volume. The uniform electric field is  
11 created by introducing voltage onto a cathode plane and gradually stepping that voltage down in  
12 magnitude across a field cage, which is formed from a series of equipotential rings surrounding the  
13 drift volume. The anode planes are arranged parallel to the cathode plane, and are composed of  
14 wires with a characteristic pitch, held at a predetermined bias voltage, that continuously sense the  
15 signals induced by the ionization electrons drifting towards them. The electrostatic potentials of the  
16 sequence of anode planes allow ionization electrons to pass undisturbed by the first planes before  
17 ultimately ending their trajectory on a wire in the last plane. The drifting ionization thus induces  
18 signals on the first planes (referred to as Induction planes) and directly contributes to the signals in  
19 the final plane (referred to as the Collection plane). Figure 2 depicts a simplified arrangement for a  
20 LArTPC.

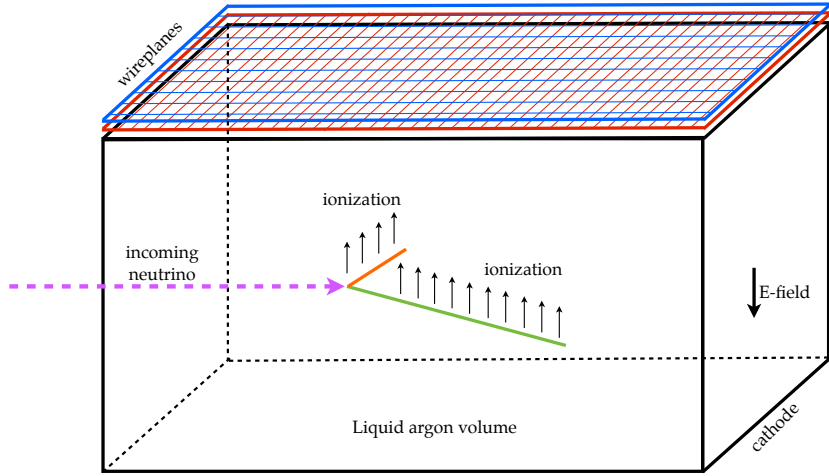


Figure 2: Operational principle of a LArTPC.

1        The charged particle trajectory is reconstructed using the known positions of the anode plane  
 2        wires and the recorded drift time of the ionization. The drift time is the difference between the  
 3        arrival times of ionization signals on the wires and the time the interaction took place in the detector  
 4        ( $t_0$ ) which is provided by an accelerator clock synced to the beam (e.g. - BNB or NuMI) or from  
 5        a trigger provided by the light collection system. The characteristics of the waveforms observed  
 6        by each wire provide a measure of the energy deposition of the traversing particles near that wire,  
 7        which, when taken as a whole for each contained particle's trajectory, allow for determination of  
 8        momentum and particle identity.

9        The scintillation photons are detected by a light collection system that is immersed in the  
 10      liquid argon and faces into the detector volume. This system provides signals that can establish the  
 11      event  $t_0$  and supplies trigger information to an electronic readout system. The precision timing of  
 12      a typical light collection device relative to that of the comparatively coarser beam structure means  
 13      that  $t_0$  derived from the light collection system is more precise, and hence the knowledge of the  
 14      drift coordinate is more precise. The light collection system signals are vital in distinguishing  
 15      detector activity that is in-time with the beam (e.g. originating from beam interactions) from that  
 16      which is out-of-time (e.g. likely not originating from beam-related interactions), benefiting event  
 17      reconstruction. Spatial information transverse to the drift direction can also be inferred from the  
 18      light collection signals, further aiding in the reconstruction of the activity occurring inside the  
 19      detector.

20       The choice of liquid argon as both the neutrino target and detector medium in LArTPCs is well  
 21      motivated, though not without introducing unique considerations for experimental design. Liquid  
 22      argon as a target for neutrinos is attractive due to its density, allowing a more compact detector with  
 23      a substantial boost in event rate over a comparable detector using less dense media, such as water.  
 24      A tradeoff to this aspect is the short radiation length (14 cm) and that the complicated structure  
 25      of the argon atom, relative to simpler targets such as hydrogen or helium, does introduce nuclear  
 26      effects that must be considered during data analysis. The cryogenic temperatures at which the  
 27      noble elements are in the liquid phase also introduces the need for additional design considerations

1 to ensure stable and safe operations.

2 Table 1 lists some of the salient properties of liquid argon. The noble liquids are all char-  
3 acterized by their excellent dielectric properties, able to maintain high voltages without suffering  
4 electrical breakdown. The long drift lengths over which ionization electrons must travel in large  
5 LArTPC detectors requires the presence of a uniform electric field over that distance. This is  
6 achieved via the introduction of extremely high voltage ( $\mathcal{O}(100\text{ kV})$  magnitude) onto the LArTPC cath-  
7 ode; this voltage is suitably maintained due to the dielectric properties of liquid argon and by ensur-  
8 ing the detector components have no sharp edges. The noble liquids are all very bright scintillators,  
9 with wavelengths deep in the UV, and also produce copious amounts of ionization. Both the scin-  
10 tillation and the ionization signals are necessary for a robust accounting of the activity occurring  
11 inside the LArTPC. Finally, the desire to build LArTPCs on increasingly larger scales, such as  
12 those necessary in neutrino experiments, is bolstered by the abundance (1% of atmosphere) and  
13 low cost of argon.

Table 1: Liquid argon properties.

Property	Value
Boiling Point [K]	87.3
Density [g/cm <sup>3</sup> ]	1.4
Scintillation $\lambda$ [nm]	128
Rad. Length [cm]	14

14 The successful implementation of the LArTPC technique depends critically on several factors.  
15 The liquid argon must be purified of any electronegative contaminants, such as water or oxygen, to  
16 accommodate the very long drift path of ionization through a MicroBooNE-sized LArTPC without  
17 significant charge loss. The signals that the ionization electrons create on the anode wires are very  
18 small, requiring low-noise electronics to discern signal pulses. The MicroBooNE collaboration  
19 has designed and constructed an experiment that addresses all of these considerations, providing  
20 critical technological development for the next generation of LArTPC experiments to build upon.

## 21 **2.2 MicroBooNE LArTPC Implementation**

22 MicroBooNE’s LArTPC active volume, which is defined as the volume immediately within the  
23 confines of the LArTPC field cage, is a rectangular liquid argon volume with dimensions 2.3 m  
24 vertical x 2.5 m horizontal x 10.4 m along the beam direction. This is the maximum volume that  
25 can be used for physics analyses. The cathode (anode) defines the beam-left (beam-right) side of  
26 the active volume. The end of the LArTPC that the beam first encounters is referred to as the  
27 “upstream” end, while the opposite end is referred to as “downstream”. Anode plane-to-plane  
28 spacing is 3 mm, and each plane has 3 mm wire pitch. The induction plane wires are oriented at  
29  $\pm 60^\circ$  relative to vertical, and the collection plane has vertically oriented wires. Field cage loops  
30 are employed to maintain uniformity of the electric field across the entire width of the detector,  
31 and these loops also act to define the top, bottom, upstream, and downstream sides of the active  
32 volume.

33 MicroBooNE uses a right-handed Cartesian coordinate system, with the origin defined to be  
34 located on the upstream face of the LArTPC, centered halfway up the vertical height of the active

1 volume and horizontally centered on the anode plane closest to the cathode (the innermost anode  
2 plane). In this system,  $x$  ranges from 0.0 m at the innermost anode plane to +2.5 m at the cathode,  
3  $y$  ranges from -1.15 m on the bottom of the active volume to +1.15 m at the top of the active  
4 volume, and  $z$  ranges from 0.0 m at the upstream end of the active volume to +10.4 m at the  
5 downstream end.

6 The light collection system, which is an array of photomultiplier tubes and scintillator pads  
7 dles, is located directly behind the anode planes on beam-right, facing the detector volume through  
8 the anode planes. The LArTPC and light collection system are immersed in liquid argon con-  
9 tained within a single-walled cryostat with a 170 ton capacity. Electronics mounted directly on the  
10 LArTPC amplify the signals on the wires, which are then passed out of the cryostat for further pro-  
11 cessing and storage on disk. Table 2 lists the primary detector design parameters of MicroBooNE,  
12 and figure 3 depicts the detector arrangement. Details of these design parameters and construction  
13 of all detector subsystems will be provided in the subsequent sections.

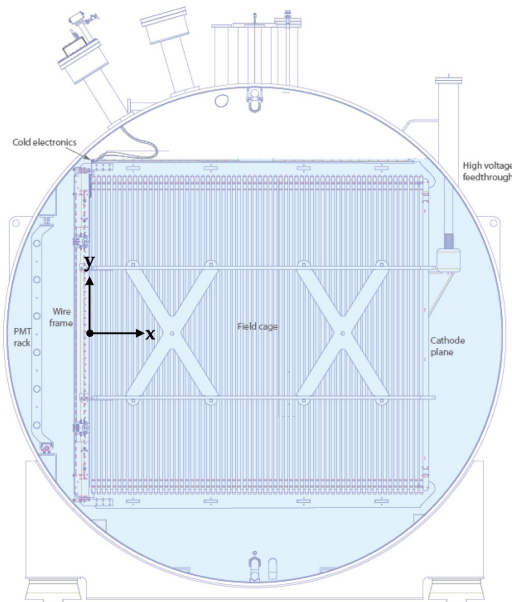


Figure 3: Diagram of MicroBooNE LArTPC. In this view, the beam would be directed out of the page (in the  $z$  direction).

### 14 3. Cryogenic System

15 The use of large quantities of highly-purified liquid argon as a detector medium in MicroBooNE  
16 requires a sophisticated cryogenic infrastructure that can maintain stable operations for years at a  
17 time. Not only must the purity of the liquid argon be maintained, but the pressure and temperature  
18 gradients within the LArTPC active volume must be tightly controlled as the drift velocity of elec-  
19 trons is dependent on these quantities. A customized cryogenic system that serves these purposes  
20 has been built, and the requirements for this system are shown in table 3.

21 The MicroBooNE cryogenic system is represented in figure 4. The central component of the  
22 system is a cryostat that houses the complete LArTPC and light-collection detector systems. The

Table 2: Primary detector design parameters for MicroBooNE.

Parameter	Value
LArTPC Dimensions	2.325 m vertically 2.560 m horizontally 10.368 m longitudinally
LArTPC argon mass	90 tons
Total Number of Wires	8256
Induction0 Wires	2400
Induction1 Wires	2400
Collection Plane Wires	3456
Drift field	500 V/cm
Light collection	30 8" diameter PMTs 4 scintillator paddles
Cryostat liquid argon capacity	170 tons
Operating temperature	87 K
Operating pressure	2 psig

Table 3: Primary design requirements for MicroBooNE cryogenic and purification systems.

Parameter	Value	Motivation
Argon purity	<100 ppt O <sub>2</sub>	MIP identification at longest drift
Argon purity	<2 ppm N <sub>2</sub>	Scintillation light output
LAr Temperature gradient	<1° K	Drift-velocity uniformity
LAr recirculation rate	1 volume change/day	Maintain purity
Cryostat heat load	<15 W/m <sup>2</sup>	Minimize convection currents and bubbles
Cryogenic capacity	10 kW	Capacity to deal with expected heat load
Cryostat maximum pressure	30 psig	Determines relief sizing

<sup>1</sup> cryostat is supported by three major subsystems: the argon purification system, the nitrogen re-  
<sup>2</sup> frigeration system, and the controls and monitoring system. These systems each represent the next  
<sup>3</sup> generation of LArTPC cryogenic system after the Liquid Argon Purity Demonstrator (LAPD) [40]  
<sup>4</sup> and make considerable use of the expertise gained during the design and implementation of that  
<sup>5</sup> apparatus.

### 3.1 Cryostat Design Overview

<sup>7</sup> Three major components make up the MicroBooNE cryostat: a stainless steel (type 304) vessel  
<sup>8</sup> to contain the liquid argon and all the active detector elements, front and rear supports to carry  
<sup>9</sup> the weight of the fully loaded cryostat, and foam insulation covering the cryostat outer surfaces.  
<sup>10</sup> The foam insulation serves to reduce heat input from the ambient environment to a sufficiently low  
<sup>11</sup> level to prevent large temperature gradients and boiling of the liquid argon. The cryostat and the  
<sup>12</sup> cryogenic systems are designed to achieve the high-purity liquid argon needed to allow ionization  
<sup>13</sup> electrons to drift to the anode wires with low probability of capture, and the high degree of thermal



Figure 4: Three-dimensional renderings of the MicroBooNE cryogenic system installed at LArTF.

homogeneity needed to avoid the introduction of non-constant drift velocities for the ionization electrons. Finally, the outer diameter of the vessel is designed to be the maximum standard size for over-the-road transport.

Ionization electrons must not be significantly attenuated, via attachment to electronegative contaminants in the liquid argon, as they drift up to 2.5 m across the active volume. This dictates that the argon be kept free of electronegative contaminants to the level of 100 parts-per-trillion (ppt). The cryostat is designed to minimize outgassing (desorption) and to avoid leakage and diffusion of air into the system. This requirement imposes strict quality assurance demands on all welds for penetrations into the cryostat and on cleaning and handling procedures for the finished vessel. Achieving the required level of purity is accomplished with a purification system, described in section 3.2, that removes electronegative contaminants from the argon during the initial fill and those introduced over time by leaks and outgassing of system components.

The electron drift velocity ( $v_d = 1600$  m/s at an electric field of 500 V/cm, with a liquid argon

1 temperature dependence  $\Delta v_d/v_d = -0.019\Delta T$ ) must remain constant in magnitude and direction  
 2 throughout the active liquid argon volume to avoid distortion of the mapping of drift time into the  
 3 position along the drift ( $\hat{x}$ ) direction. This requirement limits the allowable temperature variations  
 4 of the liquid argon to less than 0.1 K and the laminar and turbulent flow rate of liquid argon to  
 5 less than 1 m/s. These requirements limit fractional errors in velocity, and therefore in the drift-  
 6 coordinate determination, to be less than 0.1%. The constraints on constancy of drift velocity affect  
 7 the design by imposing limits on the acceptable heat flux through the insulation.

8 The cryostat is constructed to the latest American Society of Mechanical Engineers (ASME)  
 9 boiler code requirements [?] and features a single-walled construction, cylindrical shape, and  
 10 domed caps closing each end, as shown in figure 5. One end was removed for installation of  
 11 the active detectors, welded back in place upon completion of that task, and then recertified to  
 12 the ASME code requirements. Upon installation of the sealed cryostat in its final location at the  
 13 Liquid Argon Test Facility (LArTF), 16 inches of spray-on, closed cell, Polyurethane insulation  
 14 was applied to the exterior of the cryostat, as shown in figure 6. At LArTF, to avoid ground loops  
 15 that could interfere with the LArTPC signals, the cryostat vessel is grounded in only one place,  
 16 allowing it to act as a Faraday cage. This grounding scheme is explained further in section 7.1.

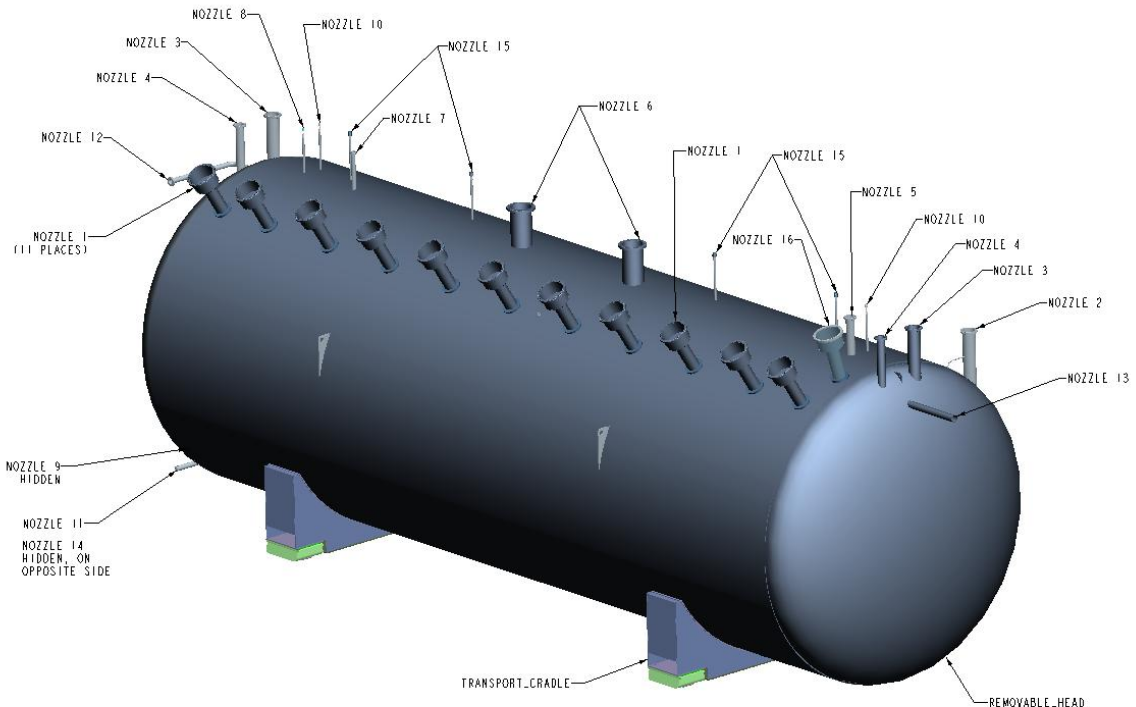


Figure 5: MicroBooNE cryostat with nozzle penetrations labeled.

17 The vessel surface has 34 nozzle penetrations for cryogenic and electrical services, detailed in  
 18 table 4. All nozzles are sealed with feedthroughs, flanges, or pipes that are suitable for operation at  
 19 the nominal pressure and temperature of the cryostat.

### 20 3.2 Liquid Argon Purification Subsystem

21 The heart of the cryogenic system is the liquid argon purification subsystem. The primary require-

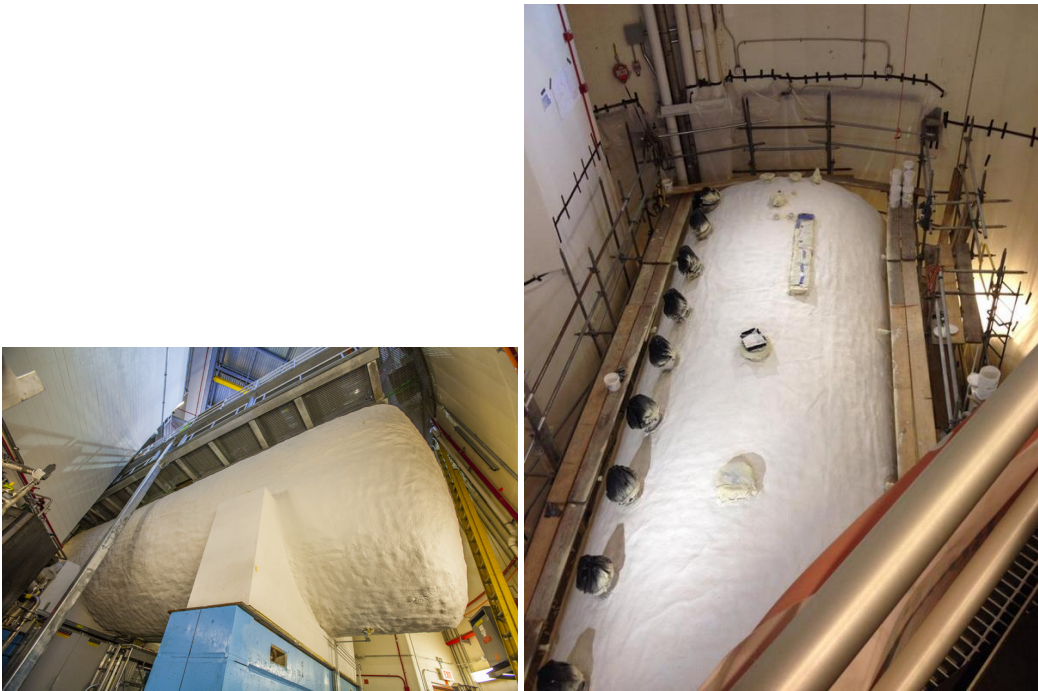


Figure 6: Photographs of the cryostat after application of exterior foam insulation.

ment of this subsystem is to keep the level of electronegative contamination to below 100 ppt of oxygen-equivalent contaminants. This requirement was determined by the physics needs of the experiment, namely the need to keep the attenuation of ionization electrons to less than 20% over the longest drift distance in the LArTPC. In addition to the requirement on the electronegative contamination, the system must maintain the level of nitrogen contamination in the argon at less than 2 parts per million (ppm) [47] to keep the attenuation of the scintillation photons in the argon to a minimum.

The MicroBooNE argon purification subsystem consists of liquid argon pumps and filters that serve to circulate the argon and remove impurities that degrade the quality of the data collected by the active detectors. There are two pumps in the system arranged in parallel in order to allow for continuous recirculation while one pump is being serviced. Similarly, there are two sets of filters arranged in parallel in the system. Figure 7 schematically depicts the flow of liquid and gaseous argon in the MicroBooNE cryogenic system.

The recirculation pumps are Barber-Nichols [48] BNCP-32B-000 magnetically-driven partial-emission centrifugal pumps. Each pump isolates the liquid argon from the electric motor. The impeller, inducer, and driving section of the magnetic coupling each have their own bearings that are lubricated by the liquid argon at the impeller. The motor is controlled by a variable frequency drive (VFD) that allows adjustment of the pump speed to produce the desired head pressure and flow within the available power range of the motor.

Each filter skid contains two filters, each having identically-sized filtration beds of 77 liters. The first filter that the argon stream enters contains a 4A molecular sieve supplied by Sigma-Aldrich [49] that primarily removes water contamination but can also remove small amounts of

Table 4: List of nozzle penetrations in MicroBooNE cryostat. CF=ConFlat flanges, RFWN=raised face weld neck flanges.

Nozzle ID	Function	Flange
N1A-N1K	LArTPC Signal Feedthrough	14" CF
N2	LArTPC HV Feedthrough	8" CF
N3A-N3B	Purity Monitor	8" CF
N4	Temperature Signals	6" CF
N5	Safety Vent	4" RFWN
N6A-N6B	Vacuum Pump-Out	10" RFWN
N7	Condensor	3"
N8	Top Instrument Port	3/4"
N9	Bottom Instrument Port	3/4"
N10A-N10B	Liquid Level Probe	3/4"
N11	Gas Circulation In	2"
N12	Gas Circulation Out	2"
N13	From LAr Filters	3"
N14	To LAr Pumps	2"
N15A-N15B	Laser Calibration	2-3/4" CF
N16	PMT Signal Feedthrough	14" CF
N17	Spare	6" CF
N18	Temperature Signals	6" CF
N19	Spare	6" CF

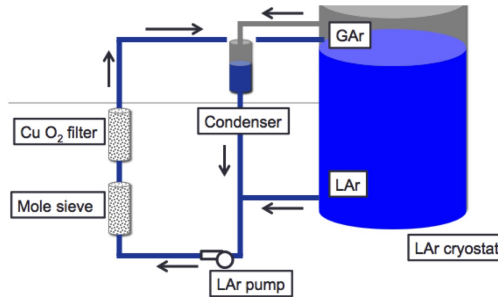


Figure 7: Flow diagram of argon in MicroBooNE, showing direction of liquid and gaseous argon in the cryogenic system. Gaseous argon from the cryostat is condensed and directed through the purification subsystem. Liquid argon drawn from the cryostat volume is directed into the purification subsystem. **NOTE: Update with better figure!**

1 nitrogen and oxygen. The second filter contains BASF CU-0226 S, a highly-dispersed copper ox-  
 2 ide impregnated on a high-surface-area alumina, which removes oxygen [50] and, to a lesser extent,  
 3 water. Thus, the oxygen filter is placed downstream of the molecular sieve to maximize oxygen fil-  
 4 tration. The oxygen-filtering media must be reduced to copper with the procedure described below  
 5 before it can remove oxygen from the liquid argon. The filters are insulated with vacuum jackets

1 and aluminum radiation shields. The metallic radiation shields were chosen because the filter re-  
2 generation temperatures, described below, would damage traditional aluminized mylar insulation.  
3 Pipe supplying the filter regeneration gas is insulated both inside the filter vacuum-insulation space  
4 and outside the filter with Pyrogel XT which is an aerogel-based insulation [51] that can withstand  
5 temperatures up to 650°C.

6 The filters are regenerated *in situ* using heated gas, by a procedure developed for LAPD. The  
7 filters are regenerated using a flow of argon gas that is heated to 200°C, supplied by a commercial  
8 500 liter liquid argon dewar. Once the argon gas reaches 200°C, a small flow of hydrogen is mixed  
9 into the primary argon flow and exothermically combines with oxygen captured by the filter to  
10 create water. Too much hydrogen mixed in with the primary argon flow would induce temperatures  
11 that are sufficiently high to damage the copper-based filter media. The damage is induced by  
12 sintering of the copper, which reduces the available filter surface area. Thus, precautions are taken  
13 to maintain a hydrogen fraction below 2.5% of the heated gas mixture. During the heated gas  
14 regeneration, five filter-bed temperature sensors monitor the filter-material temperature and the  
15 water content of the regeneration exhaust gas is measured. To remove any remaining trace amounts  
16 of water, the filters are then evacuated using turbomolecular vacuum pumps while they cool.

17 A particulate filter with an effective filtration of 10 microns, positioned between the cryostat  
18 and the filter skids, prevents any debris in the piping from being introduced into the cryostat.  
19 The particulate filter consists of a commercial stainless steel sintered-metal cylinder mounted in a  
20 custom cryogenic housing and vacuum jacket. Filtration is accomplished by flowing liquid argon  
21 to the interior, then outward through the walls, of the sintered-metal cylinder. Flanges on the argon  
22 piping, along with flanges and edge-welded bellows on the vacuum jacket, allow removal of the  
23 particulate filter.

24 The argon-purification piping is 2.54 cm diameter stainless steel that was pre-insulated by the  
25 manufacturer with 10.2 cm of polyurethane foam. During the fabrication process, all piping was  
26 washed with distilled water and detergent to remove oil and grease, then cleaned with ethanol.  
27 All valves associated with the argon-purification piping utilize a metal seal with respect to am-  
28 bient air, either through a bellows or a diaphragm, to prevent the diffusion of oxygen and water  
29 contamination. The exhaust side of each relief valve is continuously purged with argon gas to  
30 prevent diffusion of oxygen and water from ambient air across the o-ring seal. Where possible,  
31 ConFlat flanges with copper seals are used on both cryogenic and room-temperature argon piping.  
32 Pipe flanges in the system are sealed using spiral-wound graphite gaskets. Smaller connections are  
33 made with VCR fittings with stainless steel gaskets.

### 34 **3.3 Nitrogen Refrigeration**

35 The cryostat and purification systems that contain the liquid argon are subject to heat load from  
36 the environment, as well as from the active detectors that have electrical power enabled. To keep  
37 these systems operating at a stable temperature and pressure, a liquid nitrogen refrigeration system  
38 is present to provide the necessary cooling power. The liquid nitrogen system contains two con-  
39 densers that are arranged in parallel. One of these is utilized for normal operations and one serves  
40 as a backup on standby. Each condenser contains two liquid nitrogen coils, an inner and an outer,  
41 with the gas argon on the shell side, as shown in figure 9. Typically only one coil is actively running  
42 and the second can be manually activated during situations where the system heat load is higher

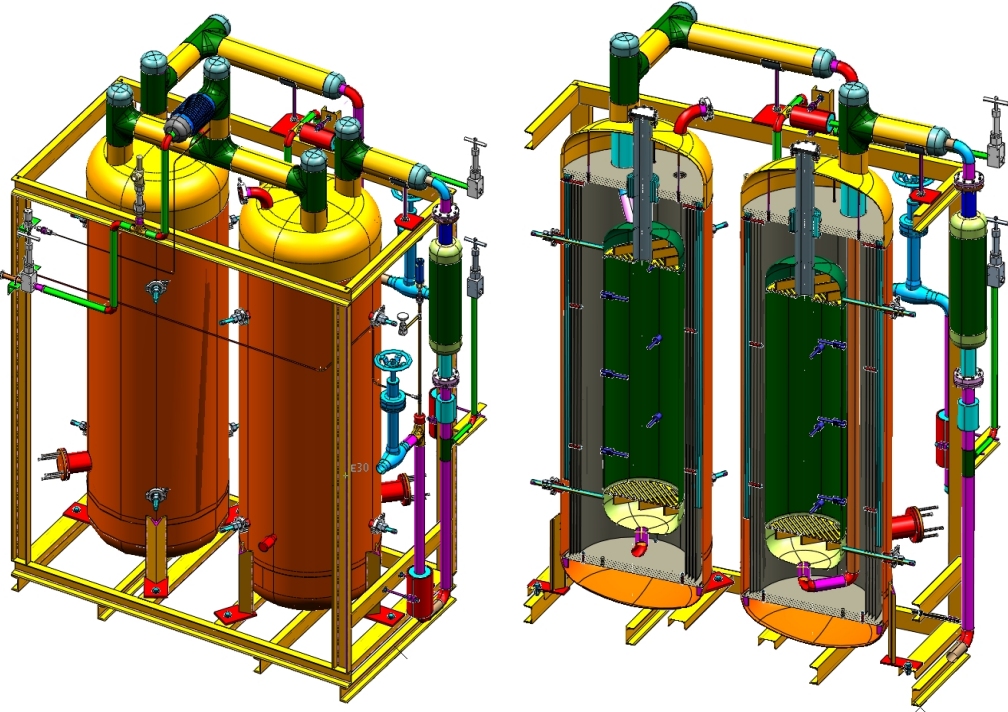


Figure 8: Three-dimensional rendering of a MicroBooNE filter skid. The left drawing shows the full skid, while the right drawing shows a cut-away of the vessels.

than usual. Each condenser is sized to handle a heat load of approximately 9.5 kW. With the vessel full of liquid argon and no pump or liquid argon circulation running, the condenser uses 600-650 gallons of liquid nitrogen per day, which equates to a 3.9 kW system heat load. Once liquid argon begins circulating using the pumps, this usage rate will increase by 50-100%.

#### 3.4 Controls and Purity Monitoring

MicroBooNE makes use of resistive thermal devices (RTDs) to measure temperatures throughout the experimental infrastructure. Twelve RTDs are located along the walls of the cryostat, and another ten RTDs are mounted inside screws attached to the structure of the LArTPC. Each of the filter vessels in the purification system contain nine RTDs. The RTDs within the filter vessels prevent overheating which could potentially occur during filter regeneration with heated argon-hydrogen gas.

Liquid argon contaminations ranging between 300 and 50 ppt oxygen equivalent can be measured using double-gridded ion chambers, henceforth referred to as purity monitors, immersed in liquid argon. The design of the purity monitors is based on the design presented in Ref. [52]. Reference [40] gives a thorough description of the purity monitors, the data-acquisition hardware and software used in LAPD. MicroBooNE uses the same type of purity monitors, and the same data-acquisition hardware and software.

A measure of the electronegative impurities is made with the purity monitor by examining the fraction of electrons generated at the purity monitor cathode that subsequently arrive at the purity

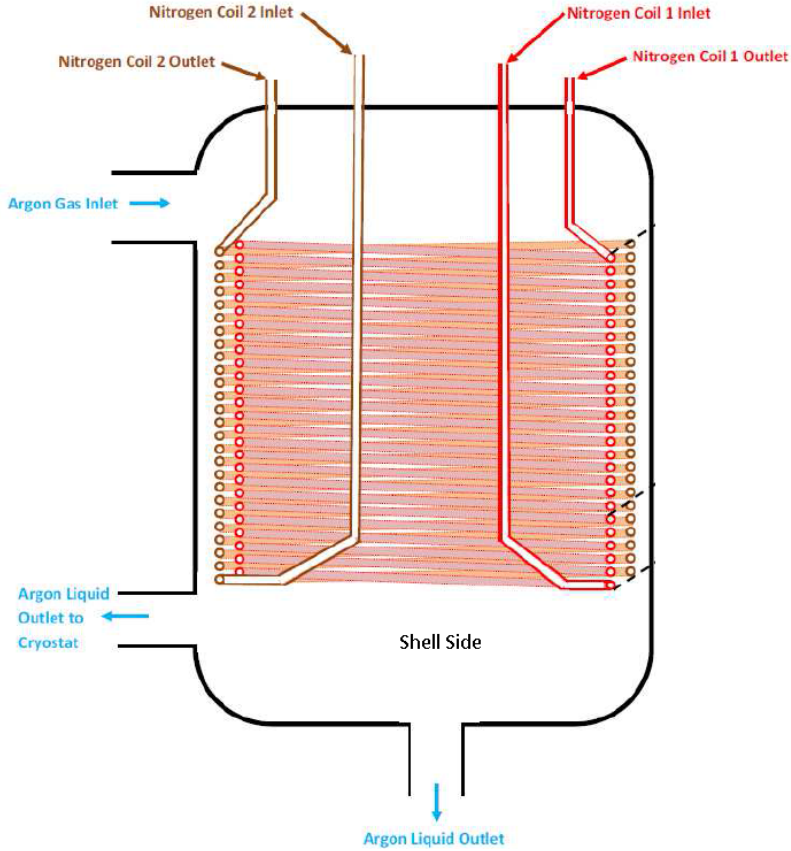


Figure 9: Diagram of a condenser.

- 1 monitor anode ( $Q_A/Q_C$ ) after a drift time  $t$ . The ratio of ( $Q_A/Q_C$ ) is related to electron lifetime,  $\tau$ ,  
2 such that

$$Q_A/Q_C = e^{-t/\tau}. \quad (3.1)$$

3 Measurement of liquid argon purity in the MicroBooNE cryogenic system are provided by  
4 three purity monitors of varying lengths. One purity monitor with a drift distance of 50 cm sits  
5 in a vessel just downstream of the filters and is used to monitor filter effectiveness. Two purity  
6 monitors, one with a drift distance of 19 cm and the other with a drift distance of 50 cm, sit within  
7 the primary MicroBooNE vessel at each end of the LArTPC.

#### 8 4. Liquid Argon Time Projection Chamber

9 The MicroBooNE LArTPC is the primary detector featured in the experiment, and it is capable of  
10 producing fine-grained images of the ionization that is liberated by charged particles traversing a  
11 volume of highly-purified liquid argon. This section describes the design and implementation of  
12 the LArTPC in the experiment.

1 The LArTPC is composed of three major structures: the cathode, the field cage, and the an-  
 2 ode. A negative voltage is introduced via a feedthrough passing through nozzle N2 on the cryostat  
 3 and applied at the cathode, which defines an equipotential surface. This cathode voltage is incre-  
 4 mentally stepped down in magnitude by means of a voltage divider chain spanning the field cage,  
 5 creating a region of uniform electric field within the LArTPC. Opposite the cathode, and oriented  
 6 parallel to it, are the anode wire planes: two induction planes (referred to as the “U” and “V”  
 7 planes) with wires oriented at  $\pm 60^\circ$  from vertical, followed by one collection plane (referred to as  
 8 the “Y” plane) with vertically-oriented wires. The wires of the anode planes are the sensitive ele-  
 9 ments that detect the ionization created by charged particles traveling through the LArTPC. Figure  
 10 depicts the assembled MicroBooNE LArTPC after insertion into the cryostat, showing details  
 11 of the cathode, field cage, and anode plane. Table 5 lists the main parameters of the MicroBooNE  
 12 LArTPC, which will be described in detail in this section.

Table 5: MicroBooNE LArTPC design parameters and nominal operating conditions.

Parameter	Value
LArTPC (active) dimensions ( $h \times w \times l$ )	2.325 m $\times$ 2.560 m $\times$ 10.368 m
LArTPC (active) mass	90 tons
# Anode planes	3
Anode planes spacing	3 mm
Wire pitch	3 mm
Wire type	SS, diam. 150 $\mu\text{m}$
Wire coating	2 $\mu\text{m}$ Cu, 0.1 $\mu\text{m}$ Ag
# wires (total)	8256
# Induction0 plane (U) wires	2400
# Induction1 plane (V) wires	2400
# Collection plane (Y) wires	3456
Wire orientation (w.r.t. vertical)	+60°,-60°,0° (U,V,Y)
Cathode voltage (nominal)	-128 kV
Bias voltages (U,V,Y)	-200 V, 0 V, +440 V
Drift-field	500 V/cm
U-V gap field	666.7 V/cm
V-Y gap field	1466.7 V/cm
Max. Drift Time, Cathode to U (at 500 V/cm)	1.6 ms
# Field-cage steps	64
Ring-to-ring voltage step	2.0 kV

## 13 4.1 Cathode

14 The cathode is assembled from 9 individual stainless steel sheets (Type 304, 0.09 inches thick) that  
 15 are fastened to a supporting frame by hex button head stainless steel screws. The outer edge of the  
 16 cathode frame consists of round stainless steel tubes of 50.8 mm outer diameter and 3.2 mm wall  
 17 thickness. Within this outer edge, square tubes with 50.8 mm  $\times$  50.8 mm cross-sectional area, and

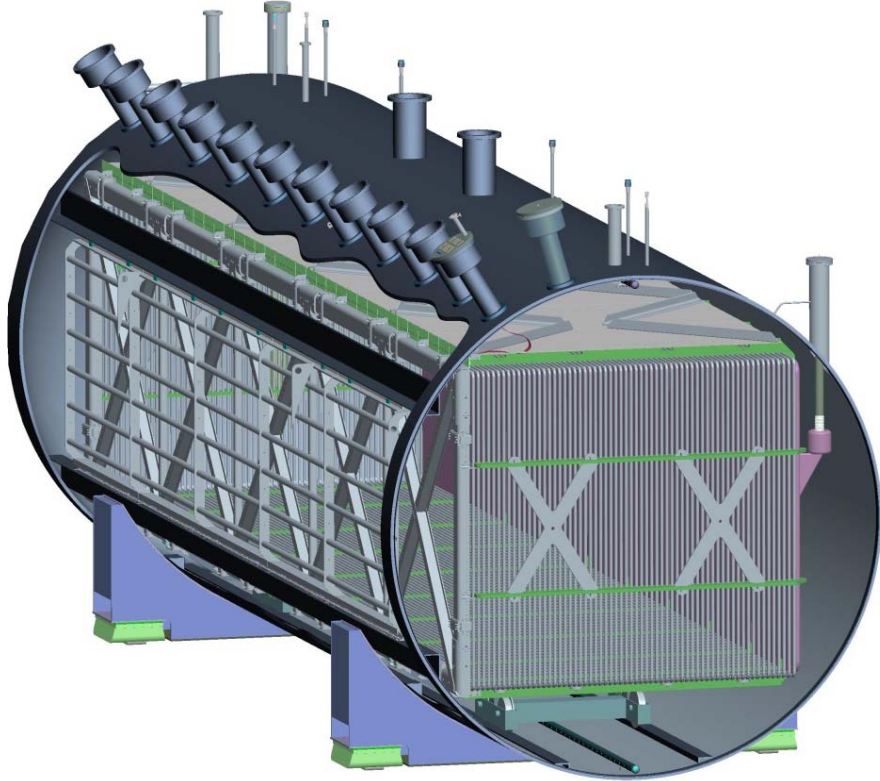


Figure 10: Schematic diagram of the MicroBooNE LArTPC , depicted as it is arranged inside the cryostat.

1    3.2 mm wall thickness, are fastened together with button head screws, forming a support structure  
 2    upon which the cathode sheets are attached. The individual components of the support structure are  
 3    further welded together to eliminate sharp features from this high-potential surface. The exterior  
 4    frame and support structure of the cathode are shown in figure 11 and a view of the interior is shown  
 5    in figure 12. The cathode plane sheets are shimmed according to survey data to make the cathode  
 6    as flat and as parallel to the anode frame as possible. Flatness of the cathode is evaluated relative to  
 7    a best fit plane of survey data (more than 10000 survey points recorded with a laser tracker). The  
 8    largest deviations of the cathode from the best fit plane are +6.6mm and -6.5mm. Approximately  
 9    55% of the measured survey points fall within +/-3mm of the best fit plane, and more than 90% of  
 10   the points fall within  $\pm 5$  mm. Figure 13 shows the results of the survey, with deviations from flat  
 11   represented as color-coded data extending away from the nominal plane of an ideal cathode.

## 12    **4.2 Field Cage**

13    The field cage encloses the volume between the cathode plane and the anode wire planes, and in  
 14   doing so creates a region with a uniform electric field. The volume defined by the interior of the  
 15   field cage, bounded by the anode and cathode planes, is referred to as the “active” volume. The field  
 16   cage structure consists of 64 individual thin-walled stainless steel tubes (1.0 inch OD, 0.065 inch  
 17   wall thickness), each shaped into a rectangular loop framing the perimeter of the active volume.  
 18   These 64 loops are mounted parallel to the cathode and anode planes, as shown in figures 11 and 12,



Figure 11: Exterior view showing the cathode frame and structural supports to which cathode sheets are fastened.



Figure 12: Interior view of cathode plane as viewed from the upstream end of the LArTPC , showing cathode sheets.

<sup>1</sup> and are held in place by a G-10 rib support structure. Each field cage loop is electrically connected  
<sup>2</sup> to its neighbors via a resistor divider chain (described in following section), causing each loop to

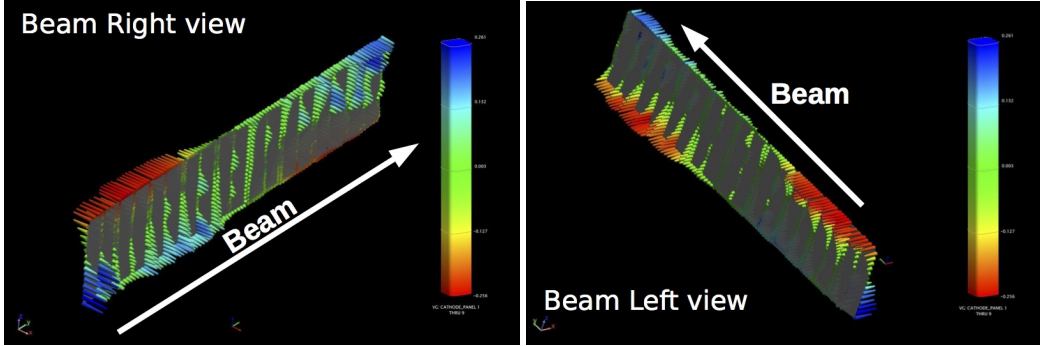


Figure 13: Survey results for interior (left) and exterior (right) of the cathode after shimming.

1 operate at a different electrical potential which in turn maintains a uniform electric field between  
 2 the cathode and anode planes. For a nominal -128 kV cathode voltage, the difference in potential  
 3 between adjacent field cage loops is 2 kV, ramping down the total potential in equidistant steps from  
 4 cathode to anode. The distance from center-to-center of adjacent field cage loops is 1.575 inches.

5 Each field cage loop is assembled from 6.77 feet long vertical pipes on the upstream and  
 6 downstream ends of the LArTPC , and on the top and bottom from two 17 feet long horizontal pipes  
 7 connected by a stainless steel coupling in the center. Each tube has venting holes approximately  
 8 every 6 inches so that they fill with liquid argon and allow air and gaseous argon to escape during  
 9 cryostat cool down and filling.

10 The four corners of each field cage loop are curved with a radius of 2.0625 inch. Each corner  
 11 is formed by three parts: two couplings and an elbow, shown in figure 14. The couplings make the  
 12 connections between the pipes and the elbow. The thin-walled tubes and elbows slip-fit over the  
 13 ends of the couplings with a 0.88-inch overlap. Each coupling has two 6-32 NC tapped holes and  
 14 the connections to the adjoining pieces are made by hex head button screws and lock washers.

15 In order to avoid electrical breakdown between the inner cryostat surface and field cage parts  
 16 at high potential on or near the cathode, the electric field strength is minimized at the corners and  
 17 edges of the field cage. Loop 0 is the cathode frame, which is at the same potential as the cathode  
 18 plane sheets attached to it. The frame is made from larger diameter piping of 2 inch OD, and it has a  
 19 slightly smaller circumference than the other field cage loops, as shown in figure 15. The elbow of  
 20 loop 1 has a specially designed shape in order to minimize the electric field potential, and the elbow  
 21 of loop 2 has a softer radius of curvature than the standard elbows. For all three of these loops (loop  
 22 0, 1, and 2), connections at corners and joints are made by welding instead of screws to avoid sharp  
 23 edges that would result in higher electric fields and greater chance of electrical breakdown.

24 Another precaution to minimize the electrical field between the loops and the cryostat surface  
 25 is the positioning of the coupling screws: for the first 20 loops, the screws are positioned on the  
 26 sides facing the screws of the neighboring loops instead of facing inward to the LArTPC active vol-  
 27 ume and outward toward the grounded cryostat surface. Hex head button screws and lock washers  
 28 are also used here in order to minimize sharp metal edges.

#### 29 **4.2.1 Resistor Divider Chain**

30 A resistor divider chain installed across the field cage loops steps the voltage down in magnitude

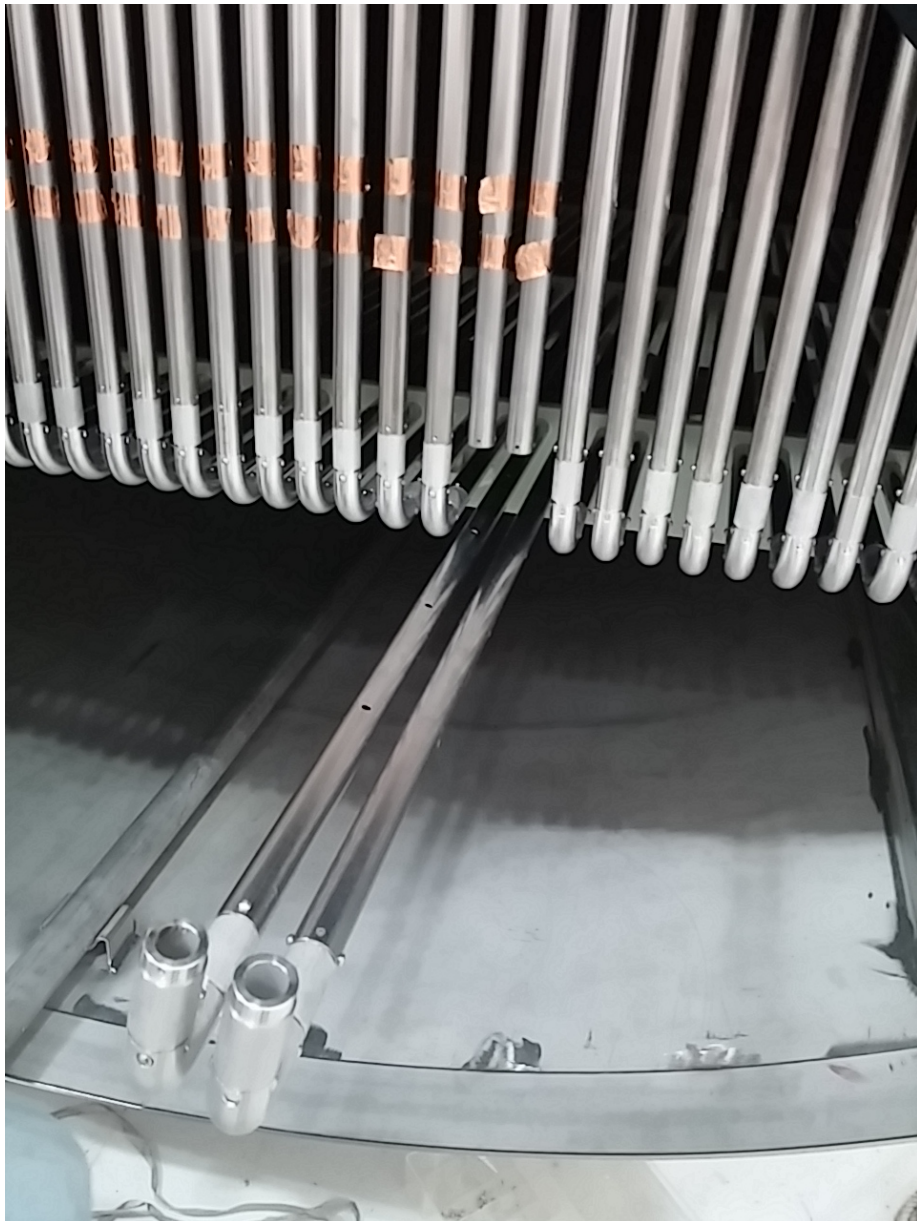


Figure 14: Field cage loops, with two partially disassembled to show elbow and couplings.

from the cathode plane to the anode wire plane in equidistant steps. 63 of the 64 loops between the cathode plane and the anode wire plane are electrically isolated. For a nominal value of -128 kV on the cathode, this results in a potential difference of 2 kV between each pair of loops. The value of the equivalent resistance between loops within the divider chain was chosen to be low enough such that the current flow through the divider circuit is much greater than the signal current flowing through the LArTPC . The signal current in this case is the total energy deposited by cosmic rays, and is estimated to be <50 nA. An equivalent resistance of  $250 \text{ M}\Omega$  between each pair of field cage loops, corresponding to a current flow of  $8 \mu\text{A}$ , was chosen.

The voltage divider chain is mounted on the inside of the field cage at the upstream end of the



Figure 15: Field cage loops closest to (and including) the cathode are modified to reduce sharp edges that would result in higher electric fields.

1 detector. The couplings at the top corner of each field cage loop have additional holes facing the  
2 inside of the field cage, where the resistors are mounted. On the first 16 field cage loops, pairs of  
3 Metallux HVR 969.23 499 M $\Omega$  resistors (rated to 23 W, 48 kV in air) are mounted electrically in  
4 parallel to establish the beginning of the voltage divider chain. On the remaining loops, thick-film  
5 Ohmite Slim-Mox 104E metal-oxide epoxy-coated resistors with a lower power and voltage rating  
6 (1.5 W, 10 kV in air) are used. Extensive testing was done on these two types of resistors, as well  
7 as others, all detailed in Ref. [?]. For redundancy, the desired 250 M $\Omega$  total resistance between  
8 each pair of field cage loops is composed of four individual 1 G $\Omega$  Slim-Mox 104E resistors placed

1 electrically in parallel and attached to a printed circuit board. Printed circuit boards span across  
2 eight field cage gaps and therefore have eight  $250\text{ M}\Omega$  resistances in series, shown in figure 16. The  
3 electrical connection between the boards and each field cage loop is made by metal contact pads  
4 on the back side of the boards, held in electrical contact with the field cage tube by a button-head  
5 hex screw and lock washer.

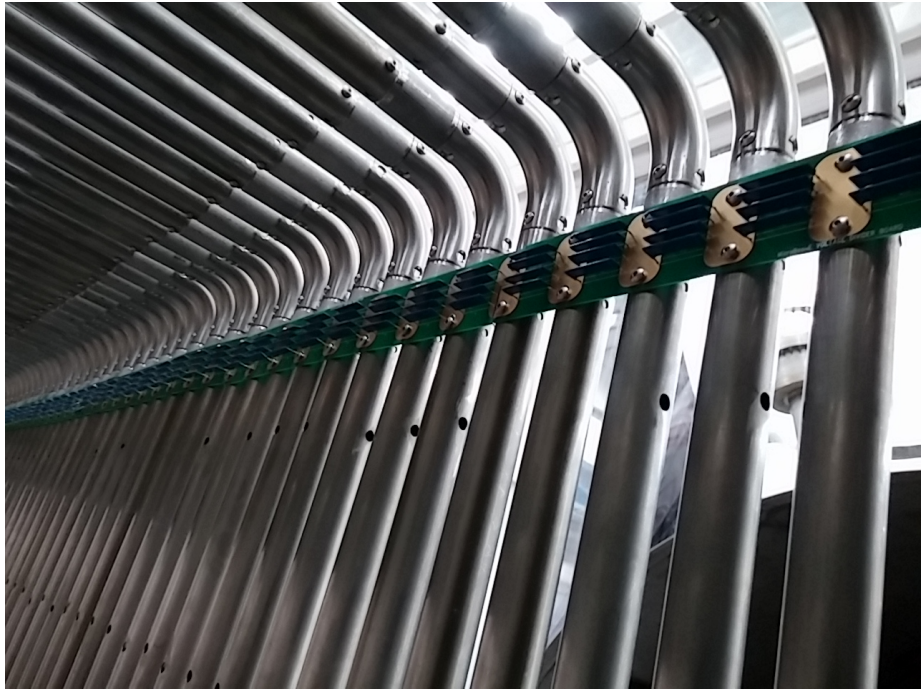


Figure 16: The Ohmite Slim-Mox 104E resistors arranged in parallel sets of four on printed circuit boards that span eight field cage tubes.

6 While the designed operating voltage difference across each resistor in the detector is 2 kV  
7 with a power flow of 4 mW, there is a slight possibility that these values could temporarily exceed  
8 the rating of the resistors in the case of discharge between the cathode plane or field cage loops and  
9 the cryostat wall, through the bulk liquid argon. Recent studies [?] have shown that the value of  
10 the minimum breakdown electrical field decreases with the increasing argon purity; for purities as  
11 high as that required in the MicroBooNE detector, breakdown has been observed at electric fields  
12 as low as 40 kV/cm.

13 The field cage behaves like a capacitance network. Based on measurements and simulations,  
14 the total energy stored inside the field cage when fully charged is estimated to be approximately  
15 24 J. In the case of a discharge between the cryostat and the cathode or one of the field cage loops  
16 close to the cathode, simulations show that voltages of up to 80 kV can develop across the resistors  
17 over the timescale of a few seconds. The observed peak voltages in such discharge scenarios de-  
18 crease the further the breakdown occurs from the cathode, such that discharges occurring between  
19 the cryostat and field cage loops 32 through 63 do not exceed the 10 kV rating of the resistors.

20 In order to protect the Ohmite Slim-Mox 104E resistors near the cathode from damage, two  
21 strategies have been implemented. First, as previously mentioned, on the first 16 field cage loops

1 near the cathode the Ohmite Slim-Mox 104E resistors are replaced by  $499\text{ M}\Omega$  Metallux HVR  
2 969.23 resistors that have a higher voltage rating of 48 kV. An extensive study of resistor breakdown  
3 in liquid argon of several resistor brands and models [?] has revealed that the breakdown voltage  
4 observed in liquid argon exceeds the rating in air substantially for all resistors. No breakdown  
5 has been observed up to 32 kV for the Ohmite Slim-Mox 104E resistor. For the Metallux HVR  
6 969.23 resistors, no breakdown has been observed up to the limit of the test apparatus of 130 kV.  
7 Since the Metallux HVR 969.23 resistors are significantly larger physically than the loop-to-loop  
8 distance, they are mounted diagonally between each pair of field cage loops. They are held by  
9 copper brackets, which are attached to studs welded onto the field cage tubes, shown in figure 17.



Figure 17: The Metallux HVR 969.23 resistors mounted on the 16 field cage loops closest to the cathode.

10 The second type of protection installed for all resistors on field cage loops 1 through 32 is a  
11 surge protection circuit. The chosen surge protection devices are designed to short the circuit in  
12 the case of a voltage spike, which protects any other electrical components installed in parallel.  
13 Below their clamping voltage, they exhibit a very high resistance and do not influence the circuit.  
14 The behavior of Gas Discharge Tubes (GDTs) and varistors in liquid argon has been studied exten-  
15 sively for application in the MicroBooNE field cage [?]. The surge protection device chosen is a  
16 Panasonic ERZ-V14D182 varistor with a clamping voltage of 1700V. In order to obtain a very high  
17 resistance in normal operation and a clamping voltage above the 2 kV in normal operation mode,  
18 three of these devices are mounted in series across a block of four Slim-Mox 104E or two Metallux  
19 969.23 resistors. These additional varistor boards make electrical contact with the field cage via  
20 brass mounting brackets that are fastened to the field cage with button head screws, as shown in  
21 figure 18.



Figure 18: Surge-protecting varistors are installed in parallel with the voltage divider resistors for the first 32 field cage loops. Here, they are shown mounted on small boards in sets of 3, and attached to the field cage by means of 6-32 hex button head screws.

### **4.3 Anode**

The anode frame holds the induction and collection plane sense wires at tension and provides overall structural support for the beam-right side of the LArTPC. Individual sense wires for all anode planes are held in place by wire carrier boards, which are printed circuit board assemblies that locate the wires as well as provide the electrical connection to the electronic readout system of the experiment.

#### **4.3.1 Mechanical structure**

The anode frame is comprised of a stainless steel C-channel hosting adjustable tensioning bars to which the wire carrier boards are attached. The C-channel and tensioning bar assembly is depicted for one corner of the anode frame in figure 19. Wire carrier boards attach to precision alignment pins distributed along the length of the tensioning bars.

#### **4.3.2 Wire winding and quality assurance**

The three anode planes are constructed from wire carrier boards that have had individually-prepared wires attached to them in groups of 16 (for the U- and V- angled planes) or 32 (for the vertical Y-plane). Consistent quality in wire preparation was achieved by a semi-automated winding machine, which terminated the ends of each wire via wrapping around 3 mm diameter brass ferrules as shown in figure 20. Each wire was tested for strength by being placed on a tensioning stand where a load of 2.5 kg (more than 3 times the nominal load of 0.7 kg) was applied for 10 minutes, ensuring that

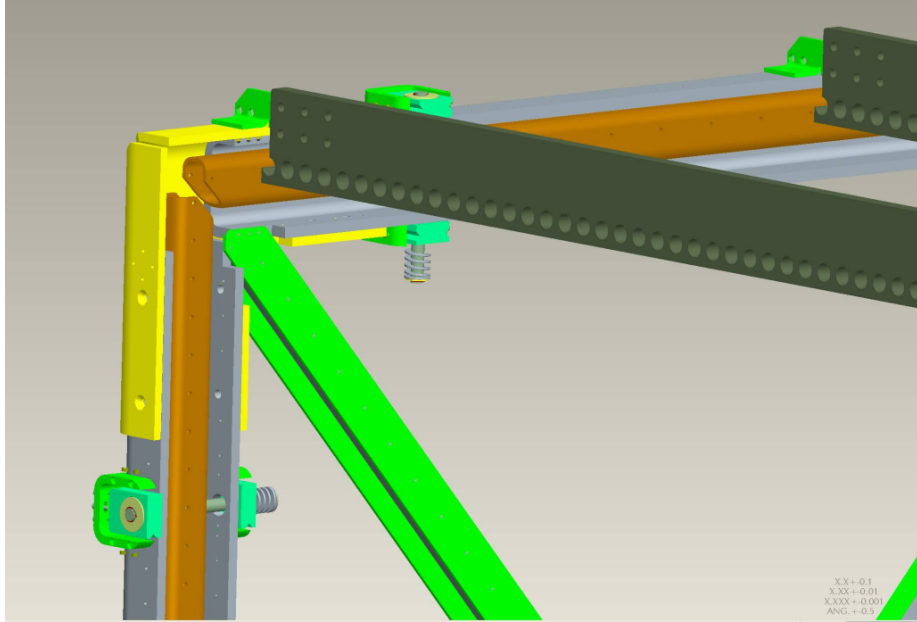


Figure 19: Rendering of the anode frame assembly. The C-channel is depicted in gray, and the adjustable tensioning bar assembly is shown in orange.

the wire preparation did not leave any weaknesses that could result in a breakage later on. Upon successful completion of the quality assurance testing for each wire, it was placed onto a wire carrier board, shown in figure 21

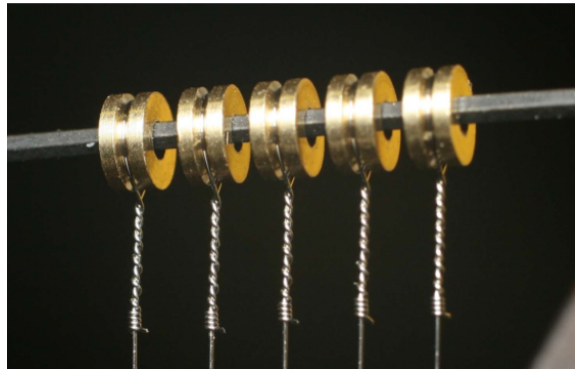


Figure 20: Picture of the wire termination on the brass ferrules. Each ferrule is 3 mm in diameter, and 1.5 mm thick.

When installed, the wires make contact with gold pins positioned on the wire carrier board, and these pins are connected to a trace that routes to the cold electronics described in section 6.1. After fully filling a wire carrier board with wires, a cover plate was installed and press-fit rivets were installed to hold the assembly together. The assembled wire carrier board was then placed onto a tension stand, to reapply a 2.5 kg tension/wire to the whole board for 10 minutes. This is to ensure that the wires were not weakened during the board assembly process. The tension stand is depicted in figure 22. A comprehensive description of the MicroBooNE wire preparation and

<sup>1</sup> associated quality assurance studies can be found in [?].

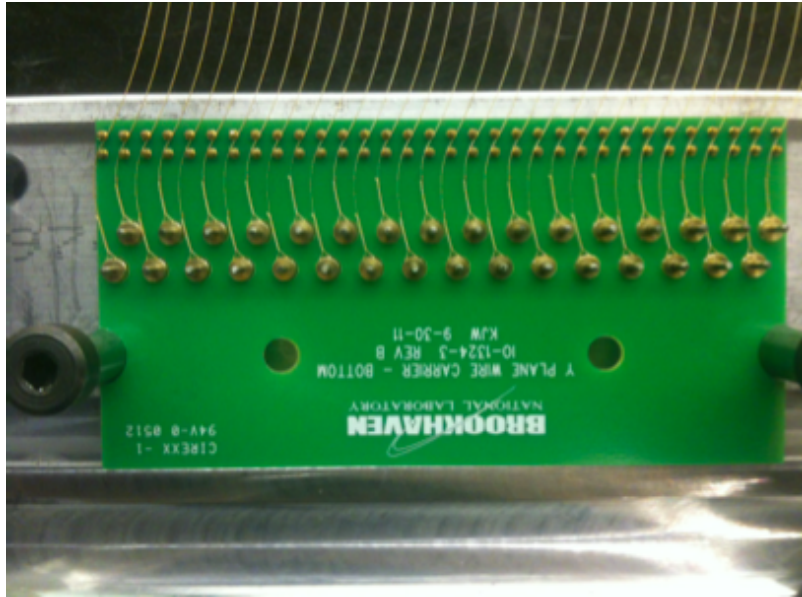


Figure 21: Picture of a collection plane wire carrier board that has been filled with wires, but has not yet had cover plate installed.

### <sup>2</sup> 4.3.3 Wire installation and tension measurements

<sup>3</sup> During detector construction the completed wire carrier assemblies were manually installed onto  
<sup>4</sup> the adjustable tensioning bars residing in the C-channel of the supporting anode frame. A team  
<sup>5</sup> of two people installed each assembly (consisting of wires and supporting carrier boards on either  
<sup>6</sup> end) onto the anode frame. The collection plane was the first installed, followed by the middle  
<sup>7</sup> induction plane, and then finally the inner induction plane. Once all three anode planes were  
<sup>8</sup> completely installed, the tensioning bars were adjusted and a survey was taken of the tension of all  
<sup>9</sup> anode wires. Tension was measured via measuring the resonant frequency of a laser beam reflected  
<sup>10</sup> off of a plucked wire and incident on a photodiode connected to a spectrum analyzer program [?].  
<sup>11</sup> The tensioning bars were adjusted iteratively until the surveyed tension of all wires was within a  
<sup>12</sup> range where no single wire was too taught or loose to create detector performance issues. Figure  
<sup>13</sup> 23 shows the final surveyed tension of the wires within the LArTPC.

### <sup>14</sup> 4.4 Parts Preparation

<sup>15</sup> The majority of the parts that make up the LArTPC are either stainless steel or G-10. These two  
<sup>16</sup> material types, as well as any others used in the LArTPC, were tested in the Fermilab Materials  
<sup>17</sup> Test Stand (MTS) [41], whose purpose was to investigate the suitability of materials for use in  
<sup>18</sup> LArTPCs. The MTS confirmed that none of the materials used in the LArTPC assembly would  
<sup>19</sup> contaminate the liquid argon. Before assembly, all LArTPC parts were cleaned according to the  
<sup>20</sup> procedures described in the following sections.



Figure 22: Picture of a collection plane wire carrier board on the tension stand.

#### **4.4.1 Cleaning stainless steel**

The delivered stainless steel parts were often greasy due to machining, and those with holes or interior cavities generally had a significant amount of trapped metal shavings due to the machining processes. Many of the pieces also had markings from permanent ink pens, dirt smears, rust spots, and/or dried oil from machining. These pieces were scrubbed with ScotchBrite 7447 general-purpose hand pads before cleaning.

Parts that were small enough to fit in an ultrasonic bath were prepared according to the following prescription. A pre-rinse with tap water was performed to remove particulate matter, followed by deburring of sharp edges. The first ultrasonic wash was 15 minutes in heated distilled water with a 3% solution of Citranox acid detergent [53]. After a first rinse in distilled water, a second ultrasonic wash was performed, again for 15 minutes, but using heated distilled water with a weak solution of Simple Green detergent [54]. A second rinse in distilled water was performed, followed by a final rinse in a fresh bath of distilled water. The parts were then wiped dry with lint-free cloths,

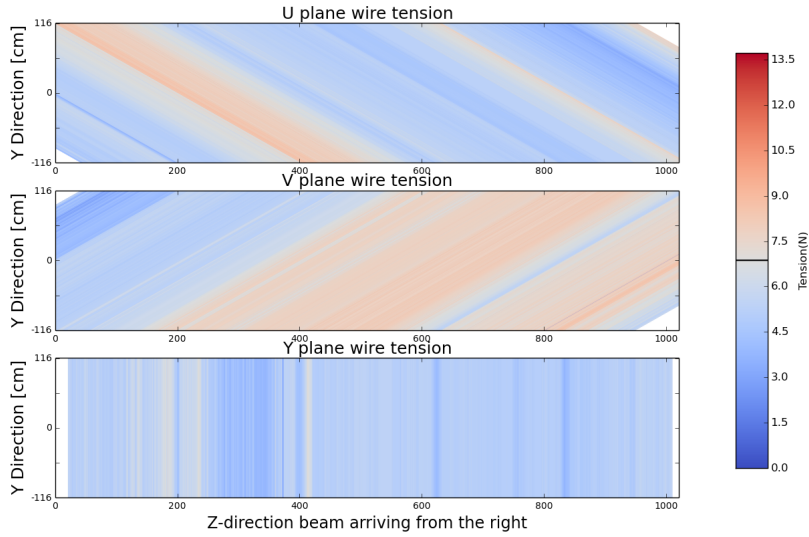


Figure 23: Final survey results for wire tension of the MicroBooNE LArTPC.

1 air dried completely, and wrapped in plastic film for storage.  
 2       Stainless steel parts which were too large to fit in the ultrasonic bath were prepared by a simpler  
 3 prescription out of necessity. A pre-rinse with tap water was followed by deburring to remove sharp  
 4 edges. Both the first and second washes were done with tap water and a weak solution of Simple  
 5 Green detergent, scrubbing with brushes and lint-free sponges. Two tap water rinses were done,  
 6 and the parts were then wiped dry with lint-free cloths. As a final additional step, each part was  
 7 wiped with 200-proof ethyl alcohol, and then air dried completely. These parts were also wrapped  
 8 in plastic film for storage.

#### 9   **4.4.2 Cleaning G-10**

10   G-10 is known to absorb large quantities of water, which would outgas in the argon and could  
 11 inhibit reaching the required argon purity in the detector. For this reason all G-10 parts were cleaned  
 12 and then baked to remove moisture. The largest G-10 parts on the detector are beams that span the  
 13 distance between the cathode and anode. These were washed in 500-gallon ultrasonic baths that are  
 14 overseen by Fermilab Accelerator Division, typically used for cleaning large sections of accelerator  
 15 beam pipes. An initial pre-wash was done with tap water to remove as much particulate matter as  
 16 possible, since the machining process left a large amount of dust on the machined edges. Pieces  
 17 were then placed in the ultrasonic bath with heated deionized water and a 2% solution of Elma-  
 18 Clean 65 (EC 65) neutral cleanser [?]. Two ultrasonic bath rinses were performed, and the pieces  
 19 were then sealed in plastic bags with clean dry nitrogen gas. In order to remove the absorbed water,  
 20 the large G-10 parts were then transported to Fermilab Technical Division where they underwent  
 21 an outgassing procedure to remove any remaining absorbed moisture. They were baked in a large  
 22 oven under vacuum until a plateau in the outgassing was reached, as reported by a monitor inside  
 23 the oven. Upon completion of the outgassing procedure, the parts were resealed in plastic bags for  
 24 storage.

1 **4.5 Assembly**

2 The full mechanical structure of the LArTPC is shown in figure 24, with the top image depicting  
3 the cathode frame on the left, made semi-transparent to show the support structures on which the  
4 cathode sheets are attached. The anode frame is on the right of this image, with I-beams configured  
5 in a crossed pattern to maintain the shape and rigidity of the outer C-channel structure. Ribs of G-  
6 10 connect the anode and cathode, electrically isolating them from each other while also providing  
7 mounting holes to hold in place each of 64 field cage loops that define the active volume of the  
8 LArTPC . The field cage loops are visible in the photograph in the bottom frame of figure 24.

9 Assembly was done inside of a clean tent, shown in figure 25, on a flat surface made up of  
10 adjustable-height metal platforms that were installed on the assembly room floor. These platforms  
11 were leveled to better than 0.5 mm before beginning assembly. The anode frame was the first part  
12 of the detector to be assembled on this surface, shown in figure 26. It was temporarily placed  
13 aside, and the cathode frame was assembled on the same set of platforms along with the G-10 ribs,  
14 which stood vertically with the help of temporary unistrut support pieces. The combined cathode  
15 and G-10 frame was then lifted and rotated to the proper orientation, with G-10 ribs extending  
16 horizontally from the cathode to the anode, as shown in figure 27. Finally, the anode frame was  
17 brought back over and attached to the G-10 ribs, and the stainless steel tubes that make up the field  
18 cage loops were fed through the holes in the G-10 ribs to complete the mechanical structure of the  
19 LArTPC .

20 **4.6 High Voltage System**

21 To create the drift electric field, an adjustable negative voltage (referred to as the “high-voltage”  
22 or “HV”) is supplied to the LArTPC cathode, generated outside of the cryostat by a Glassman  
23 LX150N12 power supply. Before entering the cryostat, the output of the power supply is passed  
24 through a current-limiting resistor series that serves as both a low-pass filter for the power supply  
25 ripple, and a stored energy partition in case of a sudden reduction in voltage. The resistor series  
26 is a set of eight 10 M $\Omega$  resistors submerged in a transformer oil in an aluminum container. This  
27 assembly was successfully tested to -200 kV. The capacitance of the cable is  $\sim$ 50 pF/m making the  
28 time constant of the component upstream of the LArTPC  $\sim$ 35 ms.

29 The potential is introduced into the cryostat by a custom-designed HV feedthrough. The  
30 feedthrough is based on an ICARUS design [7]; an inner 1.0 in diameter stainless steel conduc-  
31 tor carrying the HV is surrounded by an insulating tube, 2.0 in outer diameter and 1.0 in inner  
32 diameter, of ultra-high molecular weight polyethylene (UHMW PE), which is further encased in  
33 an outer ground tube. A photograph and drawing of the production feedthrough are shown in  
34 figure 28.

35 MicroBooNE’s voltage target combined with its geometry of a cylindrical cryostat with a  
36 single drift region necessitate that the HV feedthrough extend deeper into the cryostat than the  
37 ICARUS feedthrough to avoid high field regions. Figure 29 shows the HV feedthrough extending  
38 into its receptacle cup attached to the LArTPC cathode. The lower termination of the outer ground  
39 tube is a torus chosen to reduce the electric field between both the feedthrough and the cathode  
40 plane and along the feedthrough itself. The length of exposed UHMW PE is machined with grooves  
41 in an effort to improve performance. The electrical connection to the cathode is accomplished with

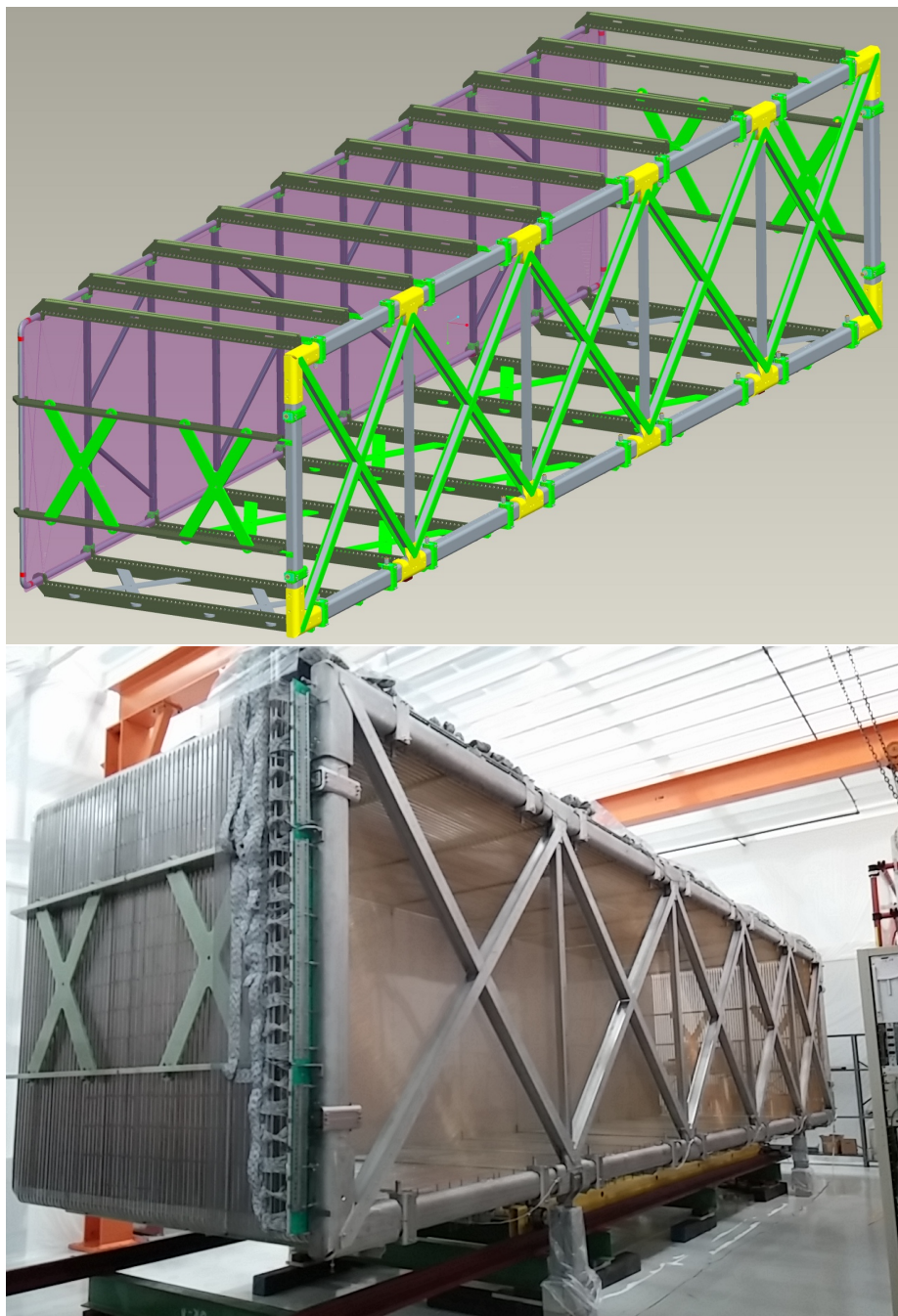


Figure 24: Top: Rendering of the full LArTPC frame assembly. Bottom: Assembled LArTPC after wire and electronics installation.

<sup>1</sup> a hemispherical spring-loaded tip attached to the inner conductor of the feedthrough. When the  
<sup>2</sup> feedthrough is installed on the cryostat, the spring-loaded tip makes contact with the receptacle  
<sup>3</sup> cup attached to the cathode.



Figure 25: Clean tent where MicroBooNE LArTPC assembly was conducted.



Figure 26: Anode frame in the process of being moved from the metal assembly platforms.

## **5. Light Collection System**

<sup>1</sup> Liquid argon is a very bright scintillator, and collecting the light produced when charged particles



Figure 27: Cathode frame and G-10 ribs on metal assembly platforms.

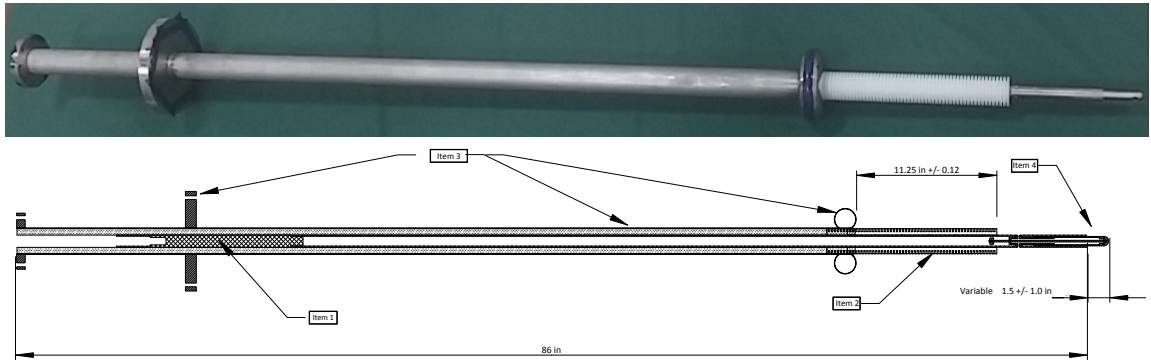


Figure 28: Photograph and drawing of the production HV feedthrough. The spherical probe tip is attached to the end of the inner conductor, on the right side of these figures.

<sup>1</sup> travel through the LArTPC is an essential aspect of fully understanding the interactions taking  
<sup>2</sup> place in the detector. This section describes the MicroBooNE light collection system.

### <sup>3</sup> 5.1 Motivation and General Design

<sup>4</sup> The installed system is designed to meet MicroBooNE's physics goals for light collection, which  
<sup>5</sup> are twofold. First, for accelerator-induced events, the light collection system is required to trigger  
<sup>6</sup> on 40 MeV kinetic energy protons produced in neutrino interactions. Second, for non-beam events,  
<sup>7</sup> efficient observation of 5 to 10 MeV electrons from supernova neutrinos are required.



Figure 29: The production HV feedthrough inserted into the cathode receptacle cup inside the cryostat.

1       The light produced by neutrino interactions in MicroBooNE is an important input for both  
2 event selection and reconstruction. One of the critical capabilities the light collection system pro-  
3 vides is the ability to form a beam-event trigger when a pulse of light is observed in coincidence  
4 with the beam spill. Because a vast majority of beam spills will not produce a neutrino interaction  
5 in the detector, such a trigger will substantially reduce the data output rate. For non-beam physics  
6 studies, the light system provides triggering and an event interaction time ( $t_0$ ). For accelerator-  
7 induced events, the start time of a beam spill is, in principle, sufficient. However, because of the  
8 long window over which the ionization electrons of an event drift (about 1.6 ms maximum drift  
9 time at 500 V/cm field), there are many accelerator-induced events in which a cosmic ray muon  
10 crosses the detector during the drift time. Utilizing the more accurate  $t_0$  from the light collec-  
11 tion system and the position of hits in the photodetectors, one can better reject cosmic ray muon  
12 tracks. The light can also be used to trigger and select specific types of cosmic-ray calibration  
13 events (Michel electrons, straight-through muons, etc.) and non-beam events (supernova neutrinos,  
14 cosmic background events to proton decay studies, etc.).

15       Light produced in liquid argon arises from two processes: scintillation and Cherenkov radia-  
16 tion. Scintillation light is produced by the formation and eventual radiative decay of excited argon

Table 6: Important properties of scintillation light in liquid argon that affect detection in MicroBooNE.

Property	Note	Ref.
Wavelength	128 nm	[?]
Singlet, Triplet state time constants	6 ns, 1.6 $\mu$ s	[?]
Photons/MeV for $E = 500$ V/cm	24000	[?]
Triplet lifetime quench due to N <sub>2</sub> at 1 ppm	20%	[?]
Attenuation length due to N <sub>2</sub> at 1 ppm	66 m	[47]
Rayleigh Scattering Length	$\sim$ 90 cm	[?]
Transparency of the wireplanes at normal incidence	86%	-

1 dimers (or eximers) and is emitted in an isotropic distribution. Liquid argon is an excellent scintil-  
 2 lator: it produces a large amount of light per unit energy deposited (about 40,000 per MeV at no  
 3 drift field) and is transparent to its own scintillation. The scintillation light has a prompt and slow  
 4 component with decay times of about 6 ns and 1.6  $\mu$ s, respectively. The two lifetimes correspond  
 5 to the two lowest-lying eximer states with the prompt component coming from the decay of a sin-  
 6 glet state and the slow from the decay of a triplet state. The prompt to slow ratio is about 1:3 for  
 7 minimum ionizing particles and varies with ionization density and particle type. Both components  
 8 consist of photons with a wavelength of 128 nm.

9 There is a significant uncertainty on the expected triplet lifetime [?] and this may be further  
 10 modified by quenching (non-radiative dissociation of excimers by impurities) [?]. Other factors  
 11 that can affect the arrival of the light include Rayleigh scattering, absorption by impurities, and  
 12 obstructions. For detailed discussion of the physics of scintillation light production and propagation  
 13 in MicroBooNE, see Ref. [?]. Table 6 summarizes information about the scintillation light.

14 Because scintillation photons have a wavelength of 128 nm they are very difficult to detect  
 15 using conventional photodetectors. Figure 30 summarizes the challenges involved in detection of  
 16 the 128 nm scintillation light. In order to detect the scintillation light, with spectrum shown in  
 17 red, the VUV photons must be shifted into the visible region. MicroBooNE employs tetraphenyl-  
 18 butadiene (TPB). This organic fluor absorbs in the UV (green line) and emits in the visible with a  
 19 peak at  $425 \pm 20$  nm (green hatched region), the peak wavelength having a slight dependence on the  
 20 micro-environment of the fluors. This is a favorable wavelength for detection by the photomulti-  
 21 plier tubes (PMTs) employed by MicroBooNE. The efficiency for transmission through borosilicate  
 22 PMT glass (black) and the quantum efficiency of the cryogenic tubes used in MicroBooNE (blue)  
 23 are overlaid on the TPB spectrum.

24 The light collection system consists of primary and secondary sub-systems. The primary light  
 25 collection system is made up of “optical units”, each one consisting of a PMT located behind a  
 26 wavelength-shifting plate. In total, 32 optical units were installed, yielding 0.85% photocathode  
 27 coverage. The secondary system consists of four light guide paddles. These paddles are introduced  
 28 for R&D studies for future LArTPCs, and are placed near the primary optical units to allow a  
 29 comparison of their performances. A flasher system, used for calibration, consists of optical fibers  
 30 bringing visible light from an LED to each PMT face.

31 The light collection detectors are located in the y-z plane behind the anode planes of the

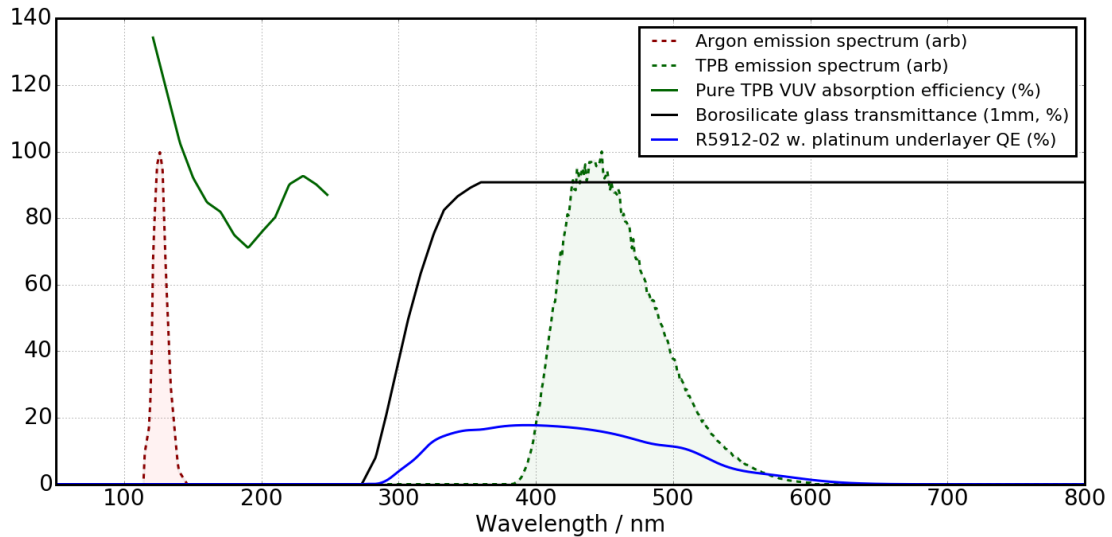


Figure 30: Scintillation light emission spectrum (red) and TPB re-emission spectrum (green), in arbitrary units. Superimposed are important efficiencies (see y axis): Dark green line – absorption of VUV light by TPB; Black line – transmission of borosilicate glass; Blue line – efficiency of a R5912-02mod cryogenic PMT [?]

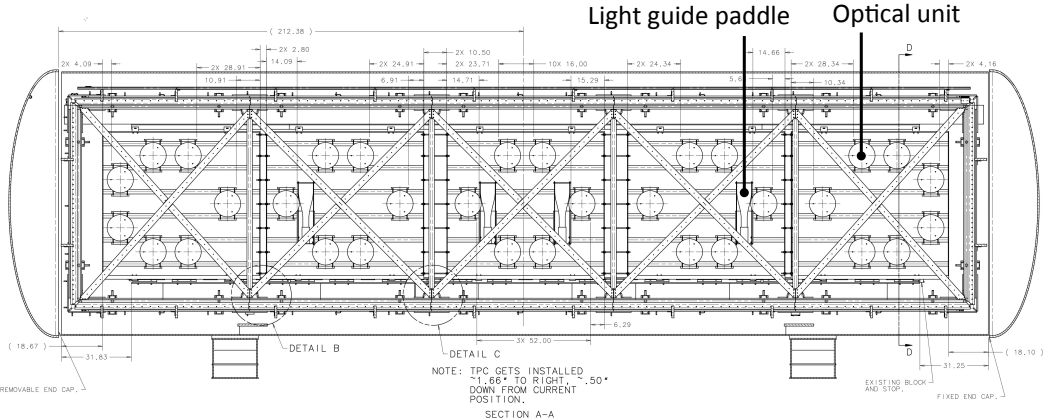


Figure 31: The MicroBooNE light collection system consists of a primary system of 32 optical units and a secondary optical system of four lightguide paddles [55]. These are mounted behind the anode wire planes such that the view is not obscured by structural cross bars of the LArTPC.

<sup>1</sup> LArTPC, as shown in figure 31. The combined transparency of the three anode planes is 86% for light at normal incidence. This transparency value assumes 100% of VUV photons impinging on the wires (150  $\mu\text{m}$  diameter and 3 mm pitch) are absorbed. The detectors were placed so as not to be obscured by the LArTPC structural cross-bars, shown in figure 31. Locating the light detectors behind the anode plane places them in a very weak electric field due to the +440 V bias of the collection plane. To test for an effect from weak electric fields, the response of a PMT placed between a +700 V mesh and ground, separated by 50 cm, was studied. The PMT zenith was 25 cm

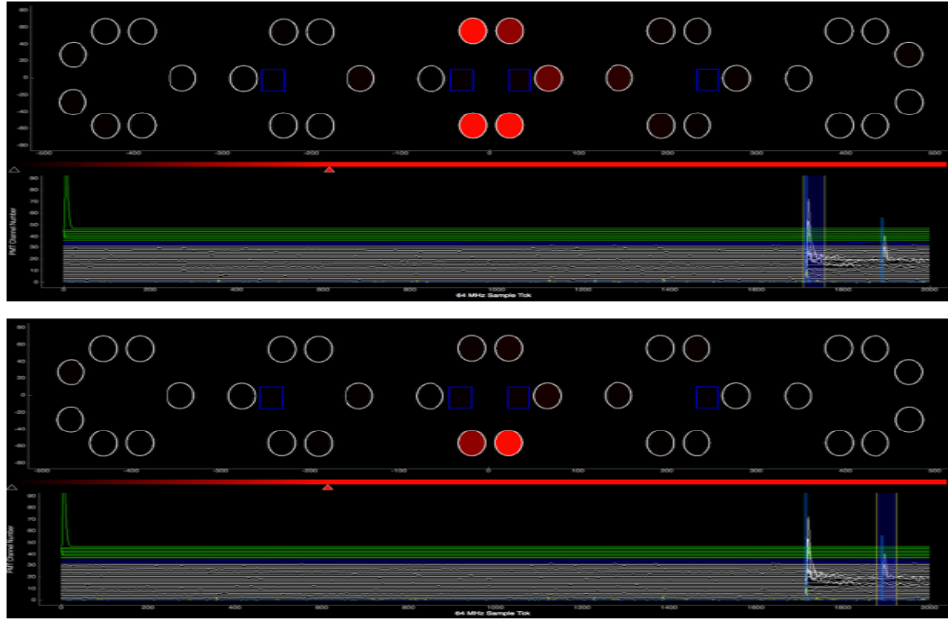


Figure 32: Two sequential event displays for the light collection system. The sequence is consistent with a muon that stops (top) and decays (bottom). The circles correspond to the optical units. Red circles indicate those units with hits. The waveforms versus time are shown below.

from the HV. No effects on the signal were observed. This was expected, as the photocathode is held at ground, effectively acting as a Faraday cage.

Throughout the design and construction of the light collection system, substantial R&D was performed. The reader should refer to Refs. [56, 57, ?, ?, 58, 47, 59, 55, 60–64] for detailed results of these studies. A useful overall review is available in Ref. [?].

Figure 32 shows the light observed in two sequential events, consistent with a muon entering the detector followed by a Michel electron from the decay. One can see that the light is relatively well localized. This allows the light to be correlated with specific tracks in the detector. This “flash-track matching” is used to identify and reconstruct the tracks that are in time with the beam spill—an important goal of the light collection system.

## 5.2 The Primary Light Collection System

Each of the 32 optical units of the primary light collection system consist of a cryogenic Hamamatsu 5912-02MOD PMT seated behind an acrylic plate coated with a TPB-rich layer and surrounded by a mu-metal shield. Figure 33 shows a diagram of one unit (left) and a photograph of installed units (right). Past experiments have directly coated PMTs with wavelength shifter [?]. However, the MicroBooNE design separates the PMT from the wavelength-shifting plate for

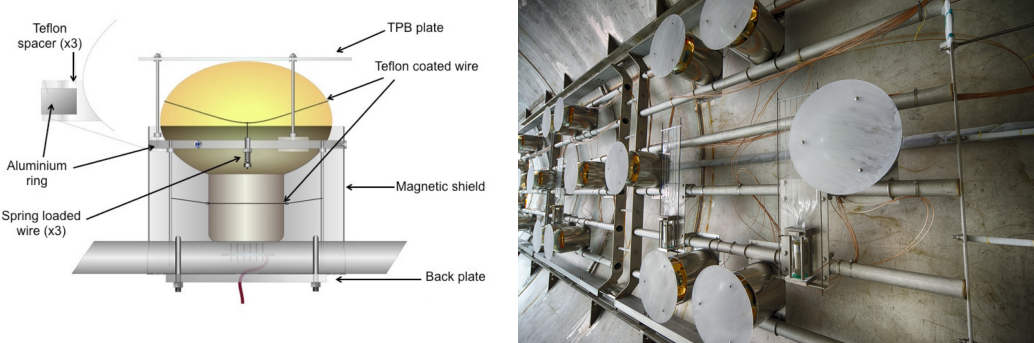


Figure 33: Left: diagram of the optical unit; Right: units mounted in MicroBooNE, immediately prior to LArTPC installation.

1 simplicity of quality control and installation. This proved important, as R&D indicated that TPB is  
 2 particularly vulnerable to environmental degradation (see section 5.2.3). In this section, description  
 3 is provided for each component of the optical unit, as well as for the overall assembly.

#### 4 **5.2.1 Photomultiplier Tubes and Bases**

5 Ref. [58] provides detailed information on the selection and testing of the 8" Hamamatsu R5912-  
 6 02mod cryogenic PMTs employed in MicroBooNE. In this section a brief summary of the findings  
 7 from this testing is presented.

8 The R5912-02mod employs a bi-alkali photocathode. Because the PMT is designed for cryo-  
 9 genic use, the R5912-02mod also features a thin platinum layer between the photocathode and the  
 10 borosilicate glass envelope to preserve the conductance at low temperatures. While this allows the  
 11 PMT to function below 150 K [?], absorption in the platinum reduces the efficiency of the PMT  
 12 by 20%. Figure 34 provides quantum efficiency curves for the 8 inch photomultiplier tubes. The  
 13 manufacturer's specifications do not include the effects of the platinum photocathode coating, but  
 14 a wavelength dependent quantum efficiency was provided by Hamamatsu for 4 of the 32 installed  
 15 PMTs. The mean and standard deviation of these curves is shown in figure 34.

16 The R5912-02mod is a 14-stage PMT. The high gain at room temperature ( $10^9$  at  $\sim 1700$  V),  
 17 compensates for known reduced gain at 87 K in the liquid argon. The high gain also has the  
 18 additional advantage of allowing operation at lower than nominal voltage which reduces heat-loss  
 19 in the cables and the potential for high voltage breakdown at the feedthroughs.

20 The PMT base is designed such that the photocathode is grounded and the last dynode in the  
 21 chain is held at large, positive voltage. Thus the PMT bulb, which is closest to the LArTPC anode  
 22 plane, is at ground and does not disturb the electric field on the wires. The result is that the high  
 23 voltage (HV) can be provided and the signal can be extracted from the PMT using a single cable,  
 24 reducing the cable volume in the vapor region and removing a possible source of out-gassing water  
 25 impurity.

26 The flat PC-board base was made of Rogers RO4000-series woven glass-reinforced laminate,  
 27 which is the same material with the LArTPC cryogenic front end boards. The base is attached  $\sim 1$   
 28 cm from the bottom of the PMT and is the closest possible distance of safe approach to the PMT

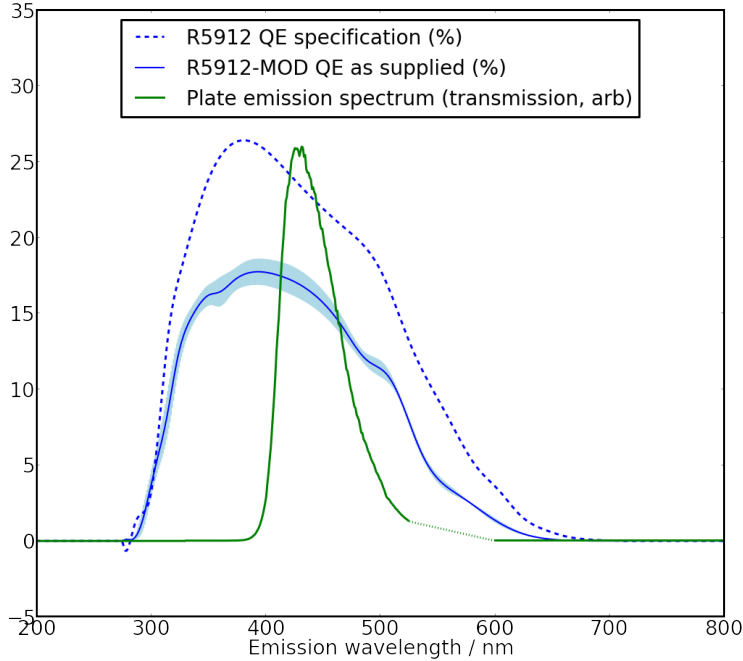


Figure 34: The specification for the non-platinum undercoated PMT from [65]. The blue band shows the mean and standard deviation of the four quantum efficiency curves provided by Hamamatsu for installed MicroBooNE PMTs. Also shown is the measured emission spectra of MicroBooNE wavelength-shifting coatings, discussed in section 5.2.2. [?]

vacuum seal tip. A schematic and photos of the PMT base are provided in Ref. [58]. The passive components include only metal film resistors and C0G/NP0 capacitors, which have the minimum temperature coefficients, and the performance at cryogenic temperatures were tested. Because the supplied HV and return signal share a single cable, the signal must be split from the HV through an AC-coupling capacitor, as is discussed in section 5.2.5.

All installed PMTs were tested in a PMT test stand, both at room temperature and in liquid nitrogen which is at 77 K. The details are described in Ref. [58]. In brief, the test stand consisted of a light-tight 346 L, liquid nitrogen filled dewar into which up to four PMTs could be installed. The PMTs were immersed and maintained in the dark environment for up to three days before most measurements of the dark rate and gain were performed. A fiber brought in light from a pulsed blue LED, which was tested for linearity with bias voltage.

Among the important results from cryogenic testing were the following [58]:

- The PMTs could be ramped to voltage quickly in the cold environment, and after 30 minutes, the gains were found to be stable.
- If the room temperature PMTs were immersed in liquid nitrogen, dramatic changes in the gain were observed after initial turn-on. The PMT gain remained high in the first  $\sim$ 5 hours after immersion, and then suddenly dropped by more than a factor of two, afterwards reaching a stable value with a small drift.

- The PMT response showed good linearity up to 100 photoelectrons (PE), which was the maximum attainable by the PMT test stand LED.
- The HV for each PMT was selected to produce a gain of  $3 \times 10^7$  in liquid nitrogen, and was typically chosen to be  $\sim 1300$  V.
- The dark current plateaus extended up to 1800 V in liquid nitrogen, and the dark current is higher in liquid nitrogen than at room temperature.
- The PMT performance depended on rate of the pulsed LED.

No PMTs were rejected on the basis of the testing. However, there were three unexpected results to note here.

The first unexpected behavior was that, at room temperature, most of the PMTs showed gains that were 10 to 30% higher than manufacturer's specifications. As expected at cryogenic temperatures, the gain is reduced by  $\sim 10\%$  to 50%. To measure the PMT gain, the LED was set to produce one to two PEs. The gain was found from the separation of the single PE peak from the pedestal, where the single PE response is fitted using the procedure described in Ref. [66].

Second, it was found that the PMTs are noisier in the cryogenic environment. It would typically be expected that thermal emission is suppressed at cryogenic temperatures and one would expect a lower dark current for PMTs operating in this regime. However, the dark current measured in the liquid nitrogen is higher than at room temperature. Although the cause is unknown, this phenomenon has previously been observed, see Ref. [67]. A proposed explanation is provided in Ref. [68].

Third, an LED pulse-rate-dependent gain shift was found during testing, as shown on figure 9 of Ref. [58]. This behavior is described qualitatively in [69]. With 10 kHz LED pulsing, the gains of cold and dark-adapted PMTs were shown to steadily increase, requiring nearly 24 hours from turn-on to stabilize. The effect was not observable at 10 Hz. This is relevant to MicroBooNE because the cosmic muon rate in the MicroBooNE detector is  $\sim 5$  kHz. Therefore a similar effect is expected in the MicroBooNE detector. Preliminary results from measurements of the PMTs installed in the LAr-filled MicroBooNE cryostat shows the expected effect.

### 5.2.2 Wavelength-Shifting Plates

In order to be sensitive to 128 nm VUV liquid argon scintillation photons, the optical assemblies use a wavelength-shifting coating to convert this VUV light to visible wavelengths that are detectable by photomultiplier tubes. In MicroBooNE, the active ingredient of this coating is TPB, an organic fluor which absorbs efficiently in the vacuum ultraviolet with an emission spectrum peaked around 425 nm [70] as shown in figure 30.

The optical unit PMTs observe light transmitted through TPB-coated, 12-inch diameter acrylic plates (see figure 35). The coating consists of a 1:1 TPB-to-polystyrene ratio, with 1 g of each dissolved in 50 ml of toluene. A small amount of ethyl alcohol is added as a surfactant. The coating is applied to the acrylic plate in three layers by brush-coating. The solution dries in air at room temperature. This leads to a final layer which is oversaturated with TPB, and white crystals form on the surface as the coating dries. The presence of surface crystallization gives the MicroBooNE plates a white, opaque finish. Details of the process are described in Ref. [71].

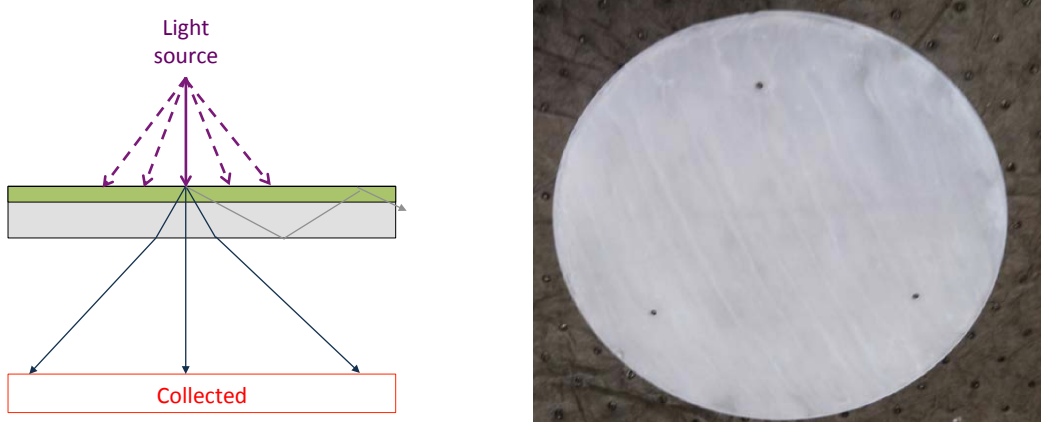


Figure 35: Left : Illustration of transmission mode, used by the optical units. Right: photograph of a coated plate.

1       The emission spectrum in figure 34 was measured using a Hitachi F-4500 fluorescence spec-  
 2 trophotometer with an incident beam of wavelength 270 nm, selected by a diffraction grating from  
 3 a xenon lamp. A standard rhodamine dye calibration sample was used to correct for drift in the  
 4 lamp and spectrometer. The measurement was made in transmission mode, and an artifact peak at  
 5 a harmonic of the twice incident wavelength was observed between 525 and 600 nm. This region  
 6 is omitted from the reported spectrum of figure 34.

7       As shown in figure 34, although the absolute quantum efficiency for the platinum-undercoated  
 8 cryogenic PMT is lower than the non-cryogenic version, the wavelength dependence is similar,  
 9 and overlap between the TPB emission spectrum and the sensitive wavelength range of the PMT  
 10 remains high. Using the measured TPB emission spectrum for plate coatings and the PMT quantum  
 11 efficiency curve provided, the spectrum-averaged PMT quantum efficiency is  $15.3 \pm 0.8\%$  per  
 12 visible photon incident on the photocathode.

13       The wavelength-shifting performance of the coating was measured at 128 nm relative to evap-  
 14 orative coatings of the type studied in [72]. Coating efficiencies were measured as a function  
 15 of wavelength between 128 and 250 nm using a vacuum monochromator at room temperature.  
 16 They were also measured in liquid argon using 128 nm scintillation light, relative to the same  
 17 evaporatively coated plate. These data are shown in figure 36, and more information about these  
 18 measurements can be found in [71].

19       The absolute efficiency of the MicroBooNE coatings can be obtained by multiplying the rela-  
 20 tive efficiencies of figure 36 by the measured absolute efficiencies from [72], and accounting for the  
 21 temperature dependence in the wavelength-shifting efficiency of pure TPB reported in [73]. The  
 22 expected efficiency of MicroBooNE coatings is found to be  $0.98 \pm 0.17$  emitted visible photons per  
 23 incident 128 nm photon for the plate coating.

#### 24     **5.2.3 UV Light Protection for the Wavelength-Shifting Plates**

25       TPB coatings have been shown to degrade under exposure to ultraviolet light [74] through a rad-  
 26 ical mediated photo-oxidation to the UV-blocker and photo-initiator benzophenone [75]. Several  
 27 measures were taken to ensure that degradation was minimized during the construction of the ex-

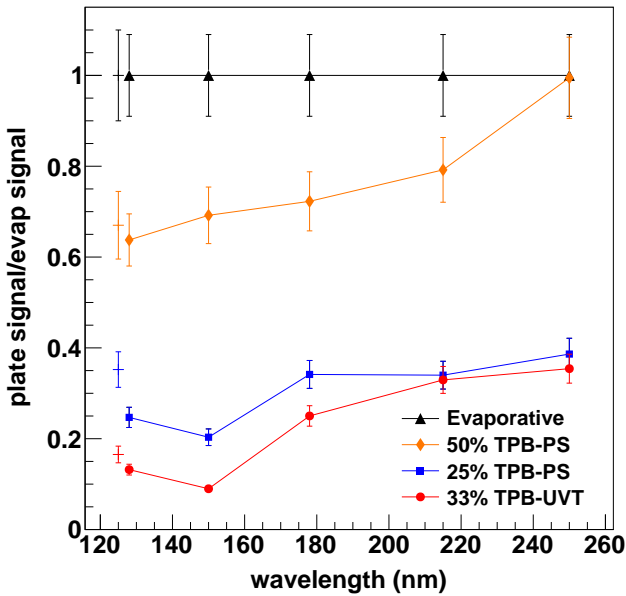


Figure 36: Measured efficiencies of various wavelength-shifting coatings, from [71]. In this plot, 50%TPB-PS is the MicroBooNE plate coating used in the optical units. The 33%TPB-UVT is the light guide coating for the secondary light collection system described below. Connected points were measured in a vacuum monochromator at room temperature, and non-connected points were measured in liquid argon with 128 nm scintillation light. All points are normalized to the performance of an evaporatively coated plate.

periment. The TPB powder and coated elements were stored in the dark at all times, with coated plates and light guides being kept wrapped in foil and stored in a dark container before installation. The detector construction area was covered with a UV blocking plastic [76], and test plates were placed at various positions in the clean tent to check for degradation from stray light. After several weeks of exposure, one test plate with a clear line of sight to the tent entrance demonstrated a few percent degradation, and all others showed no observable loss of efficiency. The open end of the MicroBooNE cryostat was shielded from light by a black curtain after installation, and the feedthroughs of the cryostat were blocked when not in use to prevent stray light from entering. The coated plates were the final component of the optical system to be installed into the detector to give the minimum possible light exposure during the detector construction process.

#### 5.2.4 Cryogenic Mu Metal Shields

The trajectories of electrons within the 8" PMT can be deflected by the Earth's magnetic field. This effect can be reduced or removed by surrounding the PMT with mu metal, a metal of low magnetic permeability. Commonly used mu-metal fails to provide shielding at cryogenic temperatures. Two types of cryogenic mu metal,Cryoperm 10 and A4K, both products of Amuneal, were identified that did provide shielding at cryogenic temperature.

The mu metal shields were tested in the apparatus shown in figure 37. The system allowed for

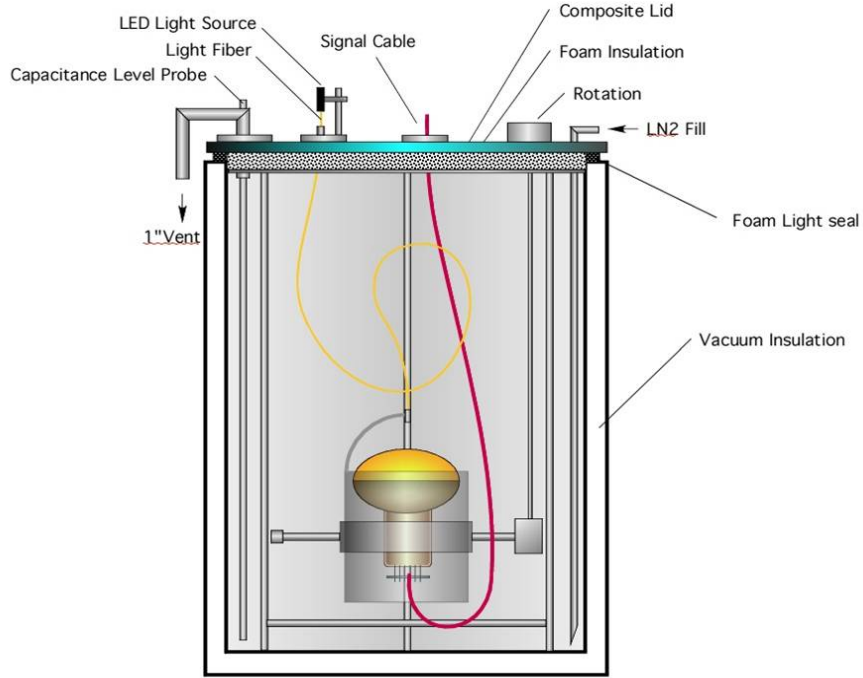


Figure 37: Schematic of the system used to study the mu-metal shields. The design allows rotation along all three axes.

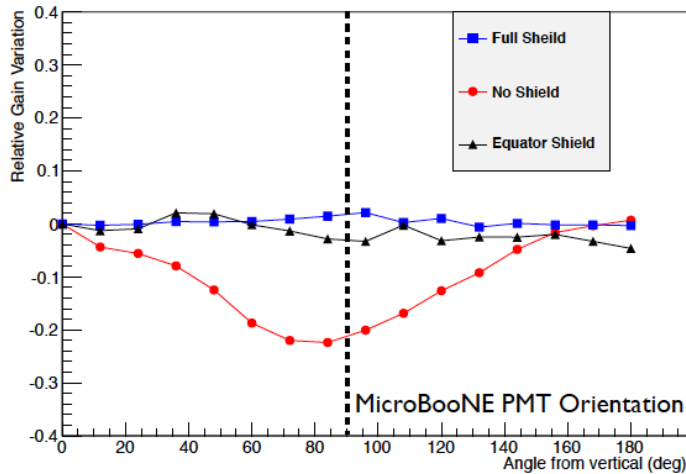


Figure 38: Red: Angular dependence of a PMT response with no shield; Black: for a shield that reaches the tube equator; Blue: for a shield that fully covers the tube to the zenith.

1 the PMT to be positioned at an angle relative to the vertical axis, with the rotator set to 30 positions  
 2 from 0 to  $348^\circ$ . The set-up was on a dolly that allowed for rotation about the vertical axis. PMT  
 3 tests were performed in air and in liquid nitrogen. PMTs were dark adapted for 5 hours before  
 4 testing. A blue LED provided 1 to 2 single PEs of light through an optical fiber. The fiber was  
 5 fixed to the PMT mount such that the endpoint was stationary with respect to the tube as the system

1 was rotated.

2 The mean charge from the PMT as a function of angle was recorded. The error was primarily  
3 systematic. The  $\sim 10^6$  to LED pulses per data point give  $< 1\%$  statistical error on the mean.  
4 However, 24-hour studies of a single point showed  $\sim 5\%$  variations in collected charge due to  
5 gain drift. Results showed that A4K and Cryoperm function essentially identically, to within the  
6 measurement error, and so MicroBooNE chose A4K, based on significant cost savings. A plot of  
7 the relative PMT gain variation versus angle from vertical, figure 38, shows that adding the shield  
8 significantly improves PMT performance. This plot shows the effect of the A4K shield with the  
9 height aligned with the equator of the PMT (black) and aligned with the zenith of the bulb (blue),  
10 compared to no shield (red) as a function of PMT azimuthal angle. Given the 5% systematic error,  
11 the two shield positions are indistinguishable.

12 As a result of these tests, the A4K shields were designed to extend just past the equator of the  
13 PMT. The shield has small holes in the backplate that allows the PMT cables to exit the shield.  
14 MicroBooNE is the first LArTPC to use cryogenic mu metal shields in its light collection system.

### 15 **5.2.5 Implementation of the Primary System**

16 The light collection system is composed of optical units assembled as shown in the left-hand picture  
17 of figure 39. The PMT is seated within the mu metal shield on three teflon pads attached to an  
18 equatorial support ring. The neck of the tube slides inside a loose wire guide-loop that prevents  
19 the PMT from tipping. The PMT is held within this assembly using teflon-encased wires that  
20 extend across the bulb and connect to wire hooks attached to the equatorial ring with stainless  
21 steel springs. Legs extending from the support at the equator are screwed into a backplate for final  
22 mounting. Concern about differences in contraction of the materials led to this design which holds  
23 the PMT in place, but with only moderate rigidity. The units were tested to ensure the PMTs would  
24 not be displaced during installation and filling. Three posts extend upward from the equatorial  
25 ring to hold the plate 3.0 cm above the apex of the bulb. The optical units slide into a cylindrical  
26 mu-metal shield, which screws into the equatorial ring. The unit is then mounted on stainless steel  
27 back-plates affixed to a support rack, as shown in the right-hand picture of figure 39.

28 The support rack consists of five stainless steel components, or modules, for ease of instal-  
29 lation. Each module has vertical height 1.83 m and horizontal length 2.07 m, resulting in a total  
30 horizontal length of 10.36 m. Unlubricated Thomson bearings fitted to the lower edge allow each  
31 module to slide into the cryostat on rails mounted in the vessel. The system was designed to allow  
32 the light detection system to slide into the vessel after the LArTPC was installed. However, in the  
33 end, scheduling permitted installation of the system before the LArTPC installation. This had the  
34 advantage of making installation and surveying easier, but the drawback that the system would be  
35 exposed to UV light for a long period. Therefore, the units were installed with dummy clear acrylic  
36 plates, and the TPB coated plates were installed only just before the LArTPC was moved in and  
37 the detector could be easily protected from light. During optical unit installation, each rack module  
38 was supported by a temporary mounting rail. The optical units were then mounted in positions  
39 chosen to avoid obstruction by the LArTPC cross-bars, as shown in figure 31. As the units were  
40 mounted and slid into the cryostat, the cables were loosely tied to the bars of the rack for support  
41 and constraint.

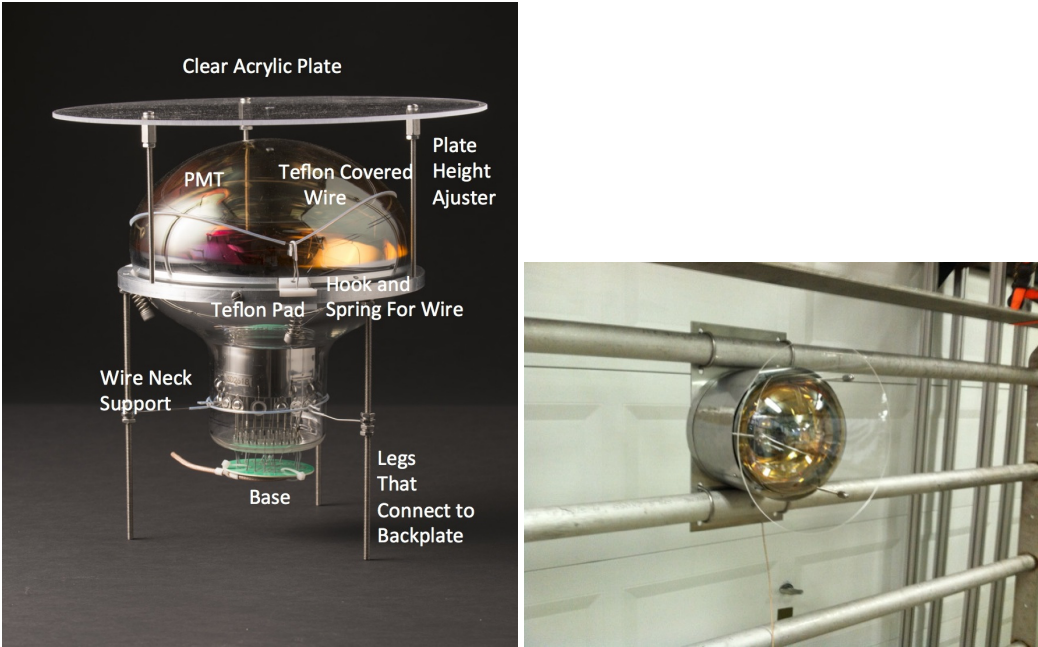


Figure 39: Left: The optical unit mount internal to the shield, with components labeled; Right: Unit mounted on rails. The clear plates were replaced with TPB-coated plates immediately before LArTPC installation, as discussed in the text [58, 55].

1       The “splitter” circuit, located outside of the cryostat, is shown in figure 40. The splitter sepa-  
 2       rates the HV of the PMT from its output signal which is subsequently split into a high-gain (HG)  
 3       and a low-gain (LG) channel. The HG and LG channels respectively carry 18% and 1.8% of the  
 4       output signal. This allows a wide dynamic range for ADC readout of the PMT pulses. The ca-  
 5       pacitance was chosen to minimize reflections, since the bases are not back-terminated. The HV is  
 6       supplied to the splitter using BiRa Corporation, Model 4877PS modules.

7       The PMT cable system delivers HV and returns signals between the external splitter and the  
 8       optical unit in the cryostat. A single cable runs from an external connector, through the feedthrough  
 9       filled with Stycast 2850 epoxy [?], into the cryostat and to the PMT base. The RG316/U coaxial  
 10      cable has 50 Ohm impedance. Cables were terminated with Pasternack PE4498 SHV to accom-  
 11      modate that the cable carries HV to the tube as well as signals from the tube. The cable carries  
 12      an AC voltage rating of 1100 V; however tests showed the DC rating to be at least three times  
 13      higher and so suitable for this use. The cables were routed through feedthroughs consisting of a  
 14      pipe filled with solidified epoxy mounted on a conflat disk. On the warm side of the feedthrough,  
 15      the cables were terminated at a patch panel with SHV connectors. The SHV connector impedance  
 16      has a negligible effect on the 20-30 ns PMT signals. SHV cables connect the patch panels to the  
 17      splitters. The impedance of every channel was tested at the feedthrough patch panel for a stable  
 18      and correct value for the base resistance, which was  $4.04 \pm 0.02$  MΩ for the 8-inch PMTs.

### 19     **5.3 The Bo Vertical Slice Tests**

20     The Bo cryostat at Fermilab is a 250-liter vacuum-insulated vessel with an inner diameter 22 inches  
 21     and a depth of 40 inches used for R&D studies, and, relevant to this paper, a vertical slice test of

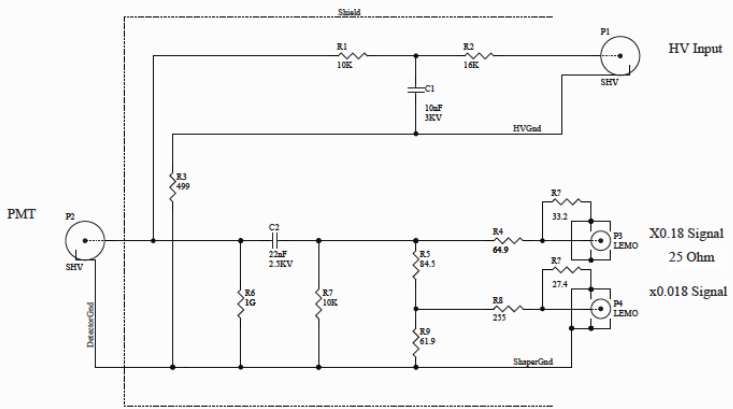


Figure 40: The "splitter" circuit. The circuit connects the HV source to the PMT. It also provides a pathway for signal pulses from the PMT to reach the readout electronics via an AC-coupling capacitor (C2). The signal is split into two copies, one provided with an attenuation factor of 0.18 and another at 0.018. Both signal sources are recorded by the readout electronics in order to provide two dynamic ranges.

the MicroBooNE optical units. The system is described in detail in Ref. [?]. The cryostat can be filled with purified LAr with parts per billion level contamination of oxygen and water and parts per million level of nitrogen. The light collection system was tested with light from visible (420 nm) and UV (250 nm) LEDs piped in via fiber, as well as scintillation light from  $^{210}\text{Po}$  alpha sources and cosmic rays.

A vertical slice test (VST) of the MicroBooNE optical system was performed in the Bo Cryostat. The slice consisted of two 8 inch PMTs with base electronics, mu-metal shield, TPB plates, cable feed throughs, splitters, the HV power supply and the interlock system. Tests were performed without and with the mu-metal shield. The test made use of the DAQ components described in section 6, including the shaper, FEM, trigger card, control card, and server. The MicroBooNE trace impurity monitors were also used.

The VST informed the final design of many components, as well as producing results relevant to understanding the running conditions and performance expectations. For example, during studies of the response of the slice to 128 nm scintillation light from the alpha source, valuable information was gathered on the single photo-electron dark rate and cosmic ray rate that could be scaled to the MicroBooNE detector expectations. As a second example, these runs allowed characterization of the pulse shape nonlinearities of the optical units, as seen in figure 41. These were shown to be significant at  $\sim 300$  photo-electron in pulse amplitude. Full amplitude saturation occurred at  $\sim 670$  PE. Thus, it is concluded that for pulses of more than 300 PE, pulse shape cannot be described by linear superposition of single photoelectron pulses.

#### 5.4 Acrylic Light Guides as a Secondary System for R&D

A secondary light collection system consisting of four lightguide paddles was also installed. This concept has several advantages for future large detectors such as DUNE. First, the collection area

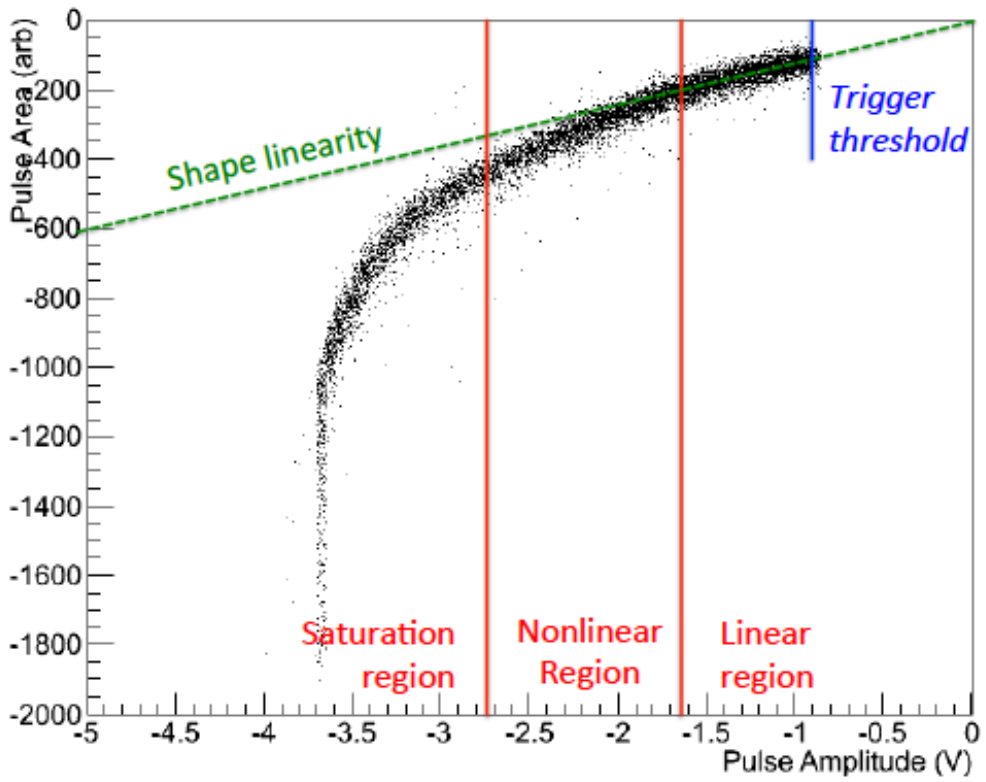


Figure 41: As shown by the VST, linearity of cosmic-ray induced PMT pulses is maintained up to amplitudes of around 1.7 V (300 PE), and amplitude saturation occurs at 3.7 V (670 PE) [?]

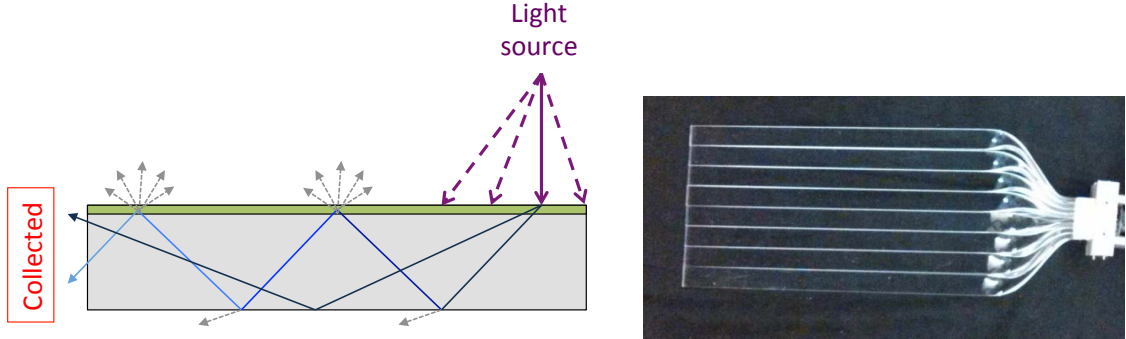


Figure 42: Left : Illustration of guiding mode, used by the paddles. Right: photograph of a coated paddle.

<sup>1</sup> per channel is larger than the optical units, providing more coverage for the same number of electronics channels, cables, and feedthroughs. Second, the detectors have a flat profile so they can <sup>2</sup> be slid between chambers in a multi-LArTPC detector, minimizing space requirements of the light <sup>3</sup>

1 collection system. In the case of MicroBooNE, the design gradually guides light in bent acrylic  
2 bars to a PMT. This design was an early alternative to a perfectly flat design that guides the lights  
3 to SiPMs. Running this system will provide long-term information on performance of lightguide  
4 based systems. It also enhances the MicroBooNE dynamic range, since the lightguide detectors  
5 saturate at a much higher light level than the optical units.

6 In the case of the lightguides, the 128 nm light is absorbed and shifted by a clear wavelength-  
7 shifting coating, and the re-emitted light is guided to a 2-inch Hamamatsu R7725-MOD PMT, as  
8 illustrated in figure 42, left. The installed paddles consist of six bars. A photograph of one coated  
9 paddle with eight bars is shown in figure 42, right. The active length of each bar is 20 inches. This  
10 system was added for R&D purposes and made use of 8 spare channels available of HV, cables,  
11 feedthroughs, and electronics. The impedance of the 2 inch PMTs, tested at the feedthrough, was  
12  $4.89 \pm 0.01 \text{ M}\Omega$ . As shown in figure 31, each paddle is installed next to an optical unit for direct  
13 comparison of performance.

14 The coating requirements for plate assemblies and light guides are different, and so the com-  
15 position and coating methods for each were separately optimized. In the case of the light guide  
16 coatings, the figure of merit is the light emitted in guided mode. Guided mode light is the light  
17 that is detected at one of the ends of a test sample, which is orthogonal to the illuminated face of  
18 the sample. In addition to the wavelength-shifting efficiency of the active layer, the detected light  
19 yield is affected by the reabsorptive and scattering losses in the coating as visible light propagates  
20 along the bar. The light guide assemblies have a TPB coating of 33% TPB to 67% UVT acrylic  
21 by mass, also with ethanol surfactant. The coating is applied as a single layer and the TPB re-  
22 mains suspended in the acrylic matrix as the coating dries, leading to a smooth, visibly transparent  
23 surface. The performance and attenuation behavior of similar light guides to those installed in Mi-  
24 croBooNE were studied experimentally in [77]. The reported non-exponential attenuation suggests  
25 that surface losses dominate over bulk losses as the attenuation mechanism, and that the fractional  
26 loss per reflection within the light guide is of order 2-3% [75].

27 In the light guide coatings, the TPB is suspended in an acrylic matrix which leads to a slight  
28 broadening of the emission spectrum compared to the spectrum from the plates. This is an ex-  
29 pected effect—TPB fluorescence has been shown to have dependence upon its microenvironment  
30 [78, 79, 73, 80, 81], and Ref. [73] demonstrated spectral broadening in the presence of a polystyrene  
31 substrate. Using the monochromator described for the plate spectrum studies, the light guide coat-  
32 ing spectrum was measured in guided mode. A 10 cm section of light guide, with the incident  
33 beam perpendicular to the TPB coated surface, was used. Based on reference [73] it is expected  
34 that the emission spectrum for the light guide coating, with TPB embedded in the substrate, will  
35 not change significantly as it cools to 87 K. The expected efficiency for the light guide coating is  
36 found to be  $0.25 \pm 0.05$  emitted visible photons per incident 128 nm photon.

## 37 **5.5 Flasher System**

38 The flasher system for the optical units and the light guides is described in Ref. [62]. This system  
39 was developed to check the timing of the installed optical units, exercise the optical units dur-  
40 ing construction and commissioning, and to calibrate them once the detector is operational. The  
41 reference provides engineering drawings and details. The system is briefly summarized here.

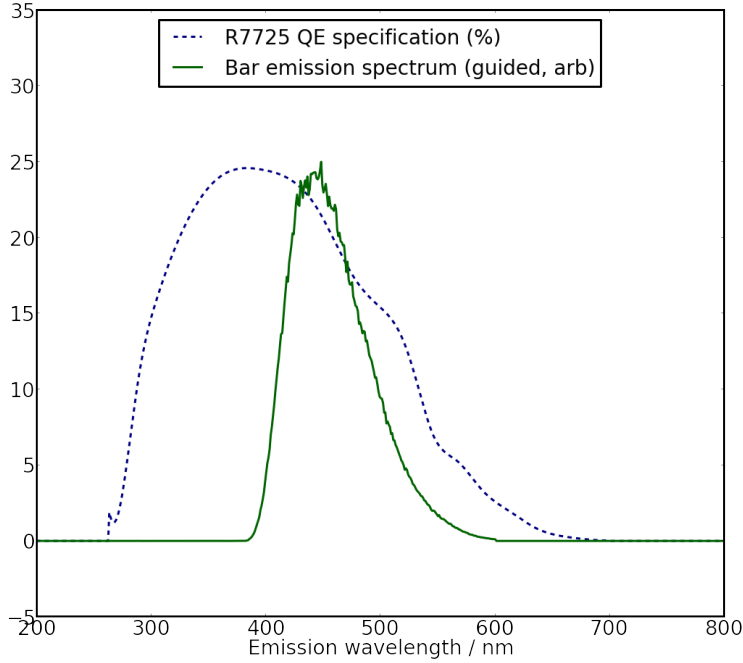


Figure 43: Measured emission spectra of the light guide coating in guided mode, and the R7725 quantum efficiency. Only the quantum efficiency of the non-undercoated PMT model is shown, from [82].

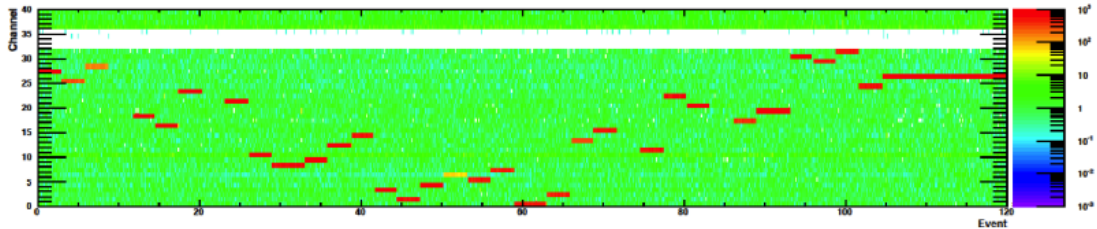


Figure 44: Charge detected in each PMT due to flasher tests, shown as a function of time. Each PMT is flashed for a short period. The white band indicates unused channels.

1       A control board pulses an array of 400 nm LEDs, each of which is coupled through an optical  
 2       feedthrough to 10 m optical fibers within the cryostat. The custom feedthrough/patch panel design  
 3       encases the fibers in Arathane CW 5620 blue with HY 5610 hardener. The internal fibers are Molex  
 4       FVP polyimide fibers with diameter of 600 mm, cladding of 30  $\mu\text{m}$ , and an additional buffer layer  
 5       of 25  $\mu\text{m}$ . Each PMT has an individual calibration fiber. Each fiber is routed along the rack and  
 6       attached to the PMTs by a fiber holder constructed of an aluminum standoff with a nylon-tipped  
 7       set screw at a distance of about 2 inches from the PMT glass.

8       Figure 44 shows the results of flasher tests on all 32 optical units and four PMTs on the paddles.  
 9       Time is along the  $x$  axis and PMT channel number is along the  $y$  axis. The white region separating  
 10      the optical unit PMTs from the paddle PMTs represents unused channels. The colored bars indicate  
 11      charge detected in the PMTs during flashing. One can see that all tubes respond properly.

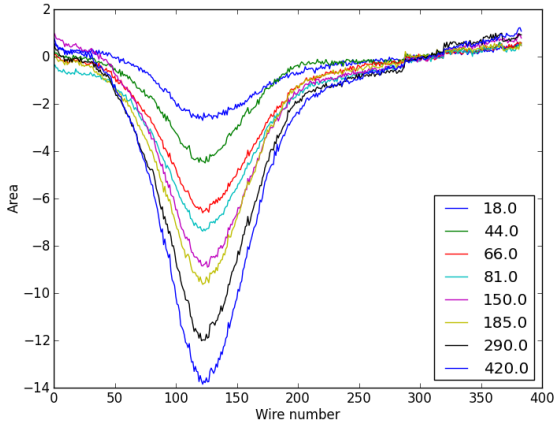


Figure 45: Area of signal pulses recorded on collection plane (in arb. units) as a function of wire number (arb. offset). The legend indicates the calibrated photo-electron count. The signal pulses are averaged over 50,000 repetitions. The plots are pinned together at wire 300, as the distribution baseline fluctuated over the course of the experiment due to intermittent noise.

## **5.6 Testing Coupling of PMT Signals to the Anode Wires**

The ICARUS detector has observed an unexpected cross-talk between their PMTs and collection wire plane [?]. The Argontube test stand at the University of Bern also observed this effect [?]. Therefore, while the LArTPC was under final testing, before being rolled into the cryostat, an experiment was devised in order to determine the implication of this cross-talk for MicroBooNE. One of the production 8" Hamamatsu R5912-02mod PMTs was placed 5" from the LArTPC collection wire plane. This PMT was encased in a dark box with an optical fiber delivering light from a LED flasher. The collection wire plane was read out using a DAQ test-stand that reflects the final DAQ design.

A clear signal was observed on the collection plane when the LED fired. The magnitude of the signal was characterized as a function of photo-electron count (figure 45) and separation between the PMT and wire-plane. The signal induced on the collection plane was estimated to be no more than  $\sim 10$  ADC counts for a cosmic ray under normal operating conditions. This was reduced to  $\sim 2$  ADC counts when the PMT was encased in the  $\mu$ -metal shields. This was deemed an acceptably small amount that further shielding was not required.

The effect appears to saturate with photo-electron count, and is reduced when shorting the resistors between the anode and last dynode. A later test with Argontube showed that the signal was drastically amplified when using capacitors not able to withstand cryogenic temperatures in the PMT base [?]. This suggests that the effect is electrostatic in nature, and probably due to capacitive coupling between the PMT and wire-plane. This is also suggested by the similarity between the signals observed and those produced by anode-coupled readout of a light collection system [64].

## **5.7 Initial Performance of the MicroBooNE Light Collection System**

The system was first powered on after the cryostat had been filled with liquid argon. All the PMTs in both the primary and secondary system were found to be operational. Figure 46 shows the

1 waveforms for all the PMT channels around the time that a large pulse, potentially from a cosmic  
2 ray muon, is observed. After initial checks of the system's health, the single photoelectron response  
3 of each PMT was set such that a one photo-electron pulse has an amplitude of 20 ADC counts as  
4 seen by the PMT readout system. The flasher LED system, described previously, is used to set this  
5 response. Figure 47 shows a candidate single photoelectron pulse following arrival of a TTL logic  
6 pulse driving the LED flasher system. The LED light level is set so that the majority (about 80%)  
7 of waveforms see no response in the region where pulses from the LED are expected to occur. This  
8 ensures that for windows with pulses, the pulses are of single photoelectrons. Figure 48 shows an  
9 example of the area vs. maximum amplitude of such pulses seen by a PMT during the flasher runs.

## 10 **6. Electronics and Readout Systems**

11 The analog signals that develop on a LArTPC during its operation must be amplified, digitized,  
12 and written to disk for use in analysis. Custom low-noise electronics that are capable of operating  
13 in the liquid argon environment have been developed for this purpose in MicroBooNE. The data  
14 from these LArTPC electronic channels, as well as from the PMTs, is sent to a readout system that  
15 digitizes and organizes the information before passing it along to a Data Acquisition (DAQ) system  
16 that stores it on disk. The stages of signal processing are illustrated in figure 49. The following sub-  
17 sections describe the LArTPC cold electronics, the LArTPC and PMT readout electronics systems,  
18 and the DAQ system in more detail. Details of triggering capabilities available in MicroBooNE are  
19 also provided in this section.

### 20 **6.1 Cryogenic Low-Noise Electronics**

21 To obtain optimum detector performance, MicroBooNE uses cryogenic low-noise front-end elec-  
22 tronics for readout of the LArTPC. To reduce electronic noise, the interconnection length between  
23 the LArTPC wires and preamplifier should be as short as possible thus minimizing the total capaci-  
24 tance seen at the preamplifier input. To accomplish this, the analog front-end ASICs, which include  
25 a preamplifier, shaper, and signal driver are located inside the cryostat in addition to the wire bias  
26 voltage distribution system, decoupling capacitors, and calibration networks. The front-end ASIC  
27 and associated circuits are implemented on a cold mother board which is directly attached to wire  
28 carrier boards on the LArTPC itself. Cold cables are used to transmit output signals from cold  
29 motherboards to warm interface electronics installed on the top of signal feed-through flanges.

#### 30 **6.1.1 CMOS ASIC**

31 The analog front end ASIC is designed in 180 nm CMOS technology, which integrates both the  
32 preamplifier and shaper on a single chip. Each chip has 16 channels to read out signals from 16  
33 wires. Each channel also has a charge injection capacitor for precision calibration. In MicroBooNE,  
34 the shaper has 4 programmable gain settings (4.7, 7.8, 14 and 25 mV/fC) and 4 programmable  
35 peaking time settings (0.5, 1.0, 2.0 and 3.0  $\mu$ s) that provide increased flexibility to the readout  
36 system. The ASIC also has programmable baseline settings (200 or 900 mV) to accommodate  
37 different detection wire configurations: either collection or induction plane. It has a selectable  
38 AC/DC coupling mode with a 100  $\mu$ s time constant for the AC coupling mode which can be used

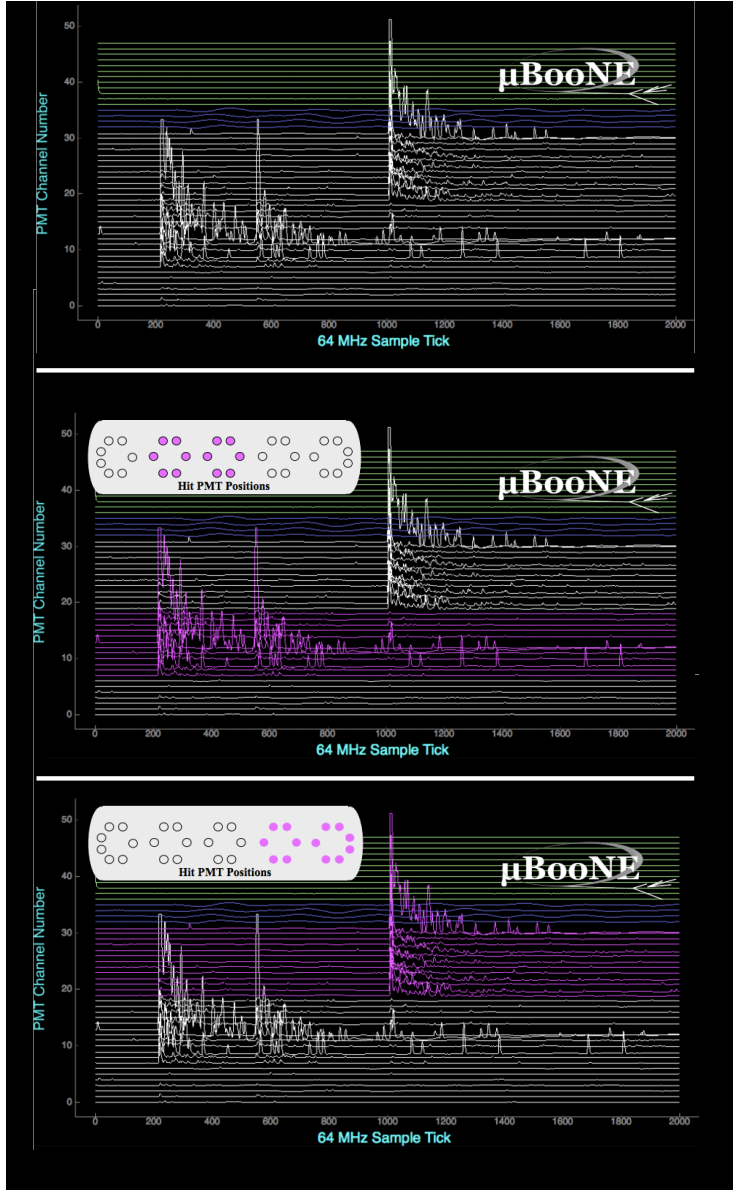


Figure 46: Top: Example waveforms from all 32 PMTs of the primary light collection system over a 31.25 microsecond readout window. The waveforms from the PMTs are in white. The blue waveforms are from the secondary lightguide PMTs, which are off in this picture. Waveforms from channels reserved for logic inputs are shown in green. In this image, the PMTs see two successive flashes of light at different parts of the detector. Middle and Bottom: Magenta highlights the early and late pulse, with the insets showing the PMTs which fired. Each pulse is likely from two cosmic ray muons traveling through the detector.

<sup>1</sup> to reduce low frequency noise. The ASIC also has built-in band-gap reference and temperature sensors to facilitate biasing and monitoring.

<sup>3</sup> The CMOS ASICs consume only  $\sim$ 6mW/channel in its default configuration. The front end ASICs of the entire detector generate  $\sim$ 50 W of heat load that is easily handled by the cryogenics

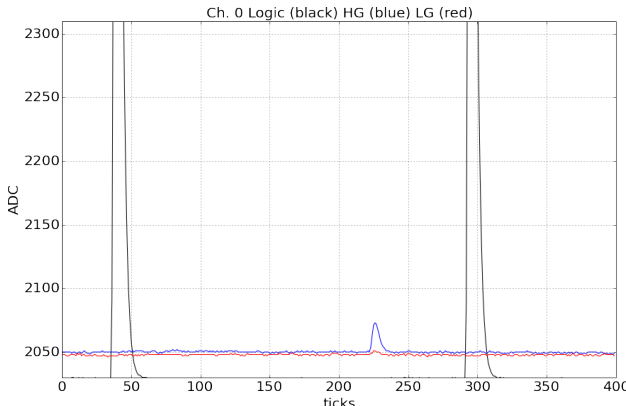


Figure 47: Example waveform captured by the PMT readout electronics during single photoelectron calibrations. The black waveform is of logic pulses that mark time at which an LED in the flasher system is driven. After some delay coming from PMT cable lengths and the flasher system, a candidate single photoelectron pulses is seen.

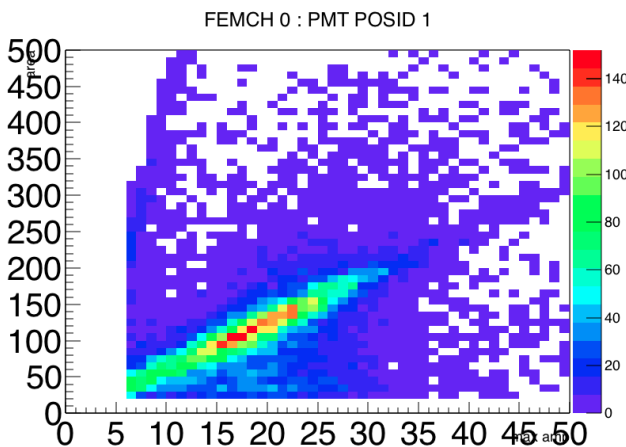


Figure 48: Distribution of the maximum amplitude and charge of pulses collected during an LED flasher calibration run. The central distribution of events is due to single photoelectron pulses.

1 system. Design guidelines that constrain the electric field and the current density to address the  
 2 lifetime of CMOS devices operated at cryogenic temperatures have been applied to every single  
 3 transistor (total  $\sim$ 15,000 transistors) in the ASIC design. A picture of the layout of the CMOS  
 4 ASIC is shown in figure 50. The test results [?] agree well with simulations and indicate that the  
 5 analog and the digital circuits (including the digital interface) operate as expected in the cryogenic  
 6 environment.

7 The MicroBooNE LArTPC has 8,256 readout channels and a total of 516 CMOS ASICs are  
 8 required to fully instrument the detector. The production testing of the CMOS ASICs required  
 9 two steps: both a warm and cold test. The warm test was performed with a dedicated test board  
 10 housed in a Faraday box containing a socket to house the ASIC for ease in chip exchange. All  
 11 programmable parameters (gain, peaking time, baseline, AC/DC coupling etc.) were exercised  
 12 with the warm test setup for careful screening at room temperature. The yield of the warm testing

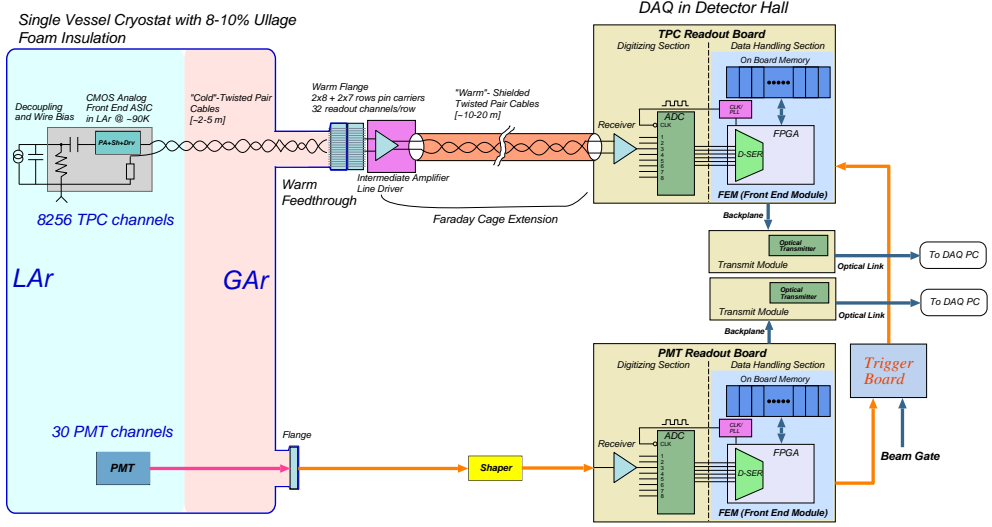


Figure 49: MicroBooNE LArTPC and PMT signal processing and readout stages.

- 1 of the ASICs was  $\sim 89\%$ . ASICs must have passed the warm test before going through cold testing.
- 2 The cold test was performed with a dedicated test board containing 6 sockets to facilitate testing
- 3 of multiple chips in liquid nitrogen at the same time. A total of 201 ASICs went through cold
- 4 testing with a yield of  $\sim 97\%$ . Based on this high yield, it was decided not to continue the cold
- 5 screening test on the rest of the production chips, as they were tested cold after being installed on
- 6 the motherboard. After enough ( $\sim 600$ ) ASICs passed the production screening test, they were sent
- 7 to an assembly house to equip the cold motherboard.

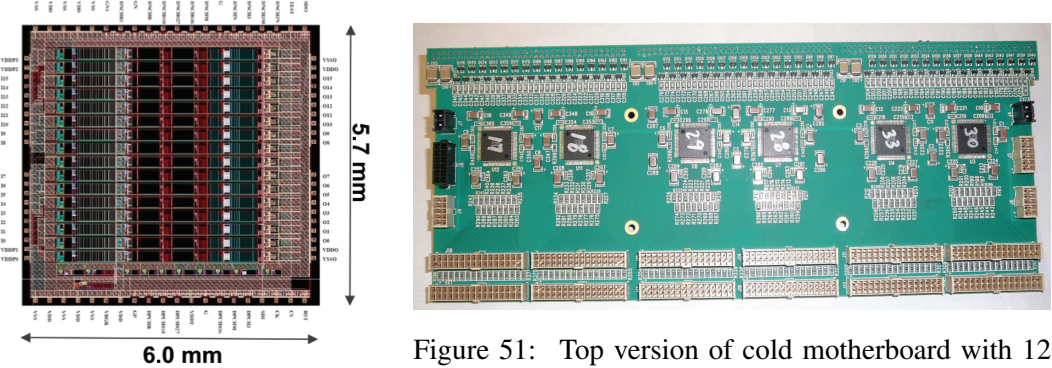


Figure 50: Layout of the CMOS analog front end ASIC

Figure 51: Top version of cold motherboard with 12 ASIC chips including 6 chips are mounted on top layer and 6 chips on bottom layer

### 6.1.2 Cold Motherboards

- 9 A cold motherboard was designed to house the MicroBooNE CMOS ASICs. In this capacity,
- 10 the motherboard provides signal interconnections both between the detector wires and preampli-

fier inputs as well as between the driver outputs and cold cables to the signal feed-through. The cold motherboard design provides sufficient protection of the ASICs against electrostatic discharge during installation. It also provides a calibration network and bias voltage distribution for the wire planes. Specifically, a calibration signal enters the cryostat via a feed-through and reaches the preamplifiers through the motherboard. Each preamplifier channel in the ASIC has a built-in switch to individually cycle the calibration injection. The bias voltage reaches the LArTPC wires via a two-fold redundant path on the motherboard that allows the detector to operate normally even if one bias voltage channel fails. Use of Rogers 4000 series as the base material of the cold motherboard avoids the potential risk of contamination of the liquid argon. The Rogers material has a similar temperature expansion coefficient as the surface mounted components which enhances the reliability of the electronics assembly when operated at cryogenic temperatures. The different positions of the wire attachments along the top and sides of the LArTPC requires 2 types of cold motherboard. The top version of the motherboard has 192 readout channels that includes 96 Y channels, 48 U channels, and 48 V channels. The side version of the motherboard has 96 readout channels that are either U or V channels. A picture of the top version of a cold motherboard with 12 mounted ASIC chips is shown in figure 51.

The MicroBooNE LArTPC required a total of 36 top version motherboards and 14 side version motherboards to instrument the full detector. A test stand was built for testing of the front end electronics. This test stand included a full readout chain from the cold motherboard, cold cable, signal feed-through, warm interface electronics, warm cable and Receiver ADC board to a DAQ board based on a Xilinx ML605 FPGA evaluation board which sends acquired data to a PC over a Gigabit Ethernet. The production test of each motherboard also involved both a warm and cold test. Both tests used the same test stand, except the motherboard was placed in a Faraday box for the warm test and submerged in a liquid nitrogen dewar for the cold test. Noise, gain, peaking time, and linearity parameters were measured in both warm and cold to screen the motherboard. Motherboards had to pass both tests before being installed on the detector.

### 6.1.3 Cold Cables

Cold cables transmit the detector signals from the cold motherboard to an intermediate amplifier on top of the signal feed-through and distribute power to the CMOS ASICs. The cold cable is a custom-built 32-pair twisted pair flat ribbon cable with Teflon FEP insulation and  $100\Omega$  ( $\pm 10\%$ ) impedance, using AWG 26 stranded wire with silver-plated copper. Custom designed shells with jack screws used in the cable assembly ensured proper alignment of the insertion on the signal feed-through pin carriers. The twisted pair cable was ordered from the manufacturer and sent to a company to be woven into flat ribbon cables. After that, an assembly house was used to assemble the various cold cables. Cold cables were produced in two different formats: signal and service cables. Signal cables are used to transmit amplified detector signals while the service cable is used to transmit calibration pulses and slow control/monitoring signals. Signal cables were produced in three different lengths: 80 inch, 100 inch and 180 inch to accommodate the different lengths between the cold motherboards and the signal feedthroughs, while the service cables were produced in two different lengths: 100 inch and 180 inch. All of the cold cable assemblies were tested with a cable tester in the assembly house before they were shipped out. In addition,  $\sim 10\%$  of the cold cables were tested in the test stand at BNL to confirm the quality of the cable assembly.

1 **6.1.4 Electronic Calibration**

2 The MicroBooNE cold electronics include a precision charge calibration system. Through the cold  
3 cable and calibration network on the motherboard, a calibration signal enters the cryostat via a  
4 feed-through and reaches the preamplifiers. A built-in switch in the ASIC makes it possible to  
5 power cycle the calibration injection for every channel individually. The electronics calibration is  
6 based on charge injection through known capacitances (180 fF) in the ASIC. This system enables  
7 gain (charge sensitivity) calibration, verification of sense wire integrity and noise measurements.  
8 The built-in electronics calibration capability is an important tool in testing and characterizing the  
9 overall performance of the detector readout system. It was extensively used in the cold electronics  
10 production testing and the electronics checkout during installation, commissioning, and data taking.

11 **6.1.5 Performance Tests**

12 The development of the analog front end ASICs was initiated using 180 nm CMOS technology  
13 and 300 K models, though the performance parameters are extracted at 77 K. CMOS was found to  
14 function at cryogenic temperatures with increased gain and lower noise. The noise, gain, and pulse  
15 shaping were found to be as expected in evaluation tests of the ASICs. Extensive test of the ASICs  
16 mounted on the motherboards was performed in liquid nitrogen because noise performance can be  
17 better evaluated in liquid nitrogen than at room temperature. Thus, cold tests were performed on all  
18 production cold motherboards fully populated with 12 chips. A total of  $\sim$ 2,200 chip-immersions  
19 were accumulated in liquid nitrogen without any failures due to thermal contraction or expansion.

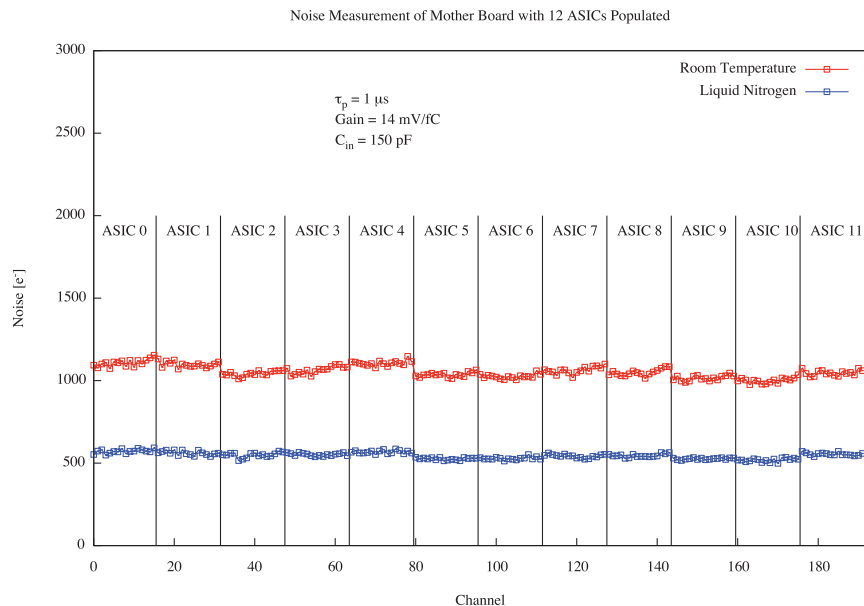


Figure 52: Plot of noise vs. temperature of 12 ASICS, total 192 channels. Noise is  $\sim 1,200 e^-$  at 293K, and  $\sim 550 e^-$  at 77 K with 150 pF  $C_d$

20 The test results show the noise of the front end readout electronics system decreasing uni-  
21 formly for all 768 channels from  $\sim 1,200 e^-$  at 293 K to less than  $600 e^-$  at 77 K with 150 pF

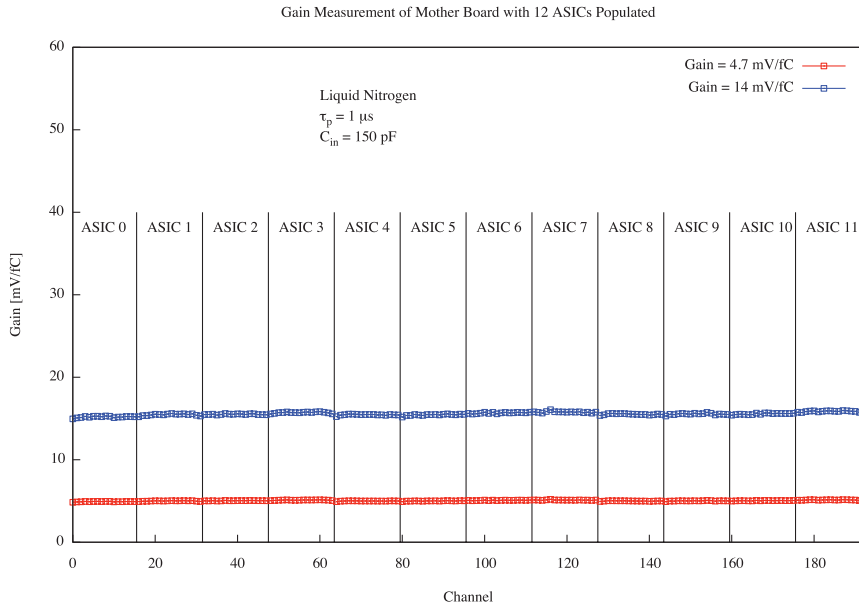


Figure 53: Plot of gain uniformity of 12 ASICs, total 192 channels, at 77 K with two different gain settings

detector (sense wire) capacitance. A plot of noise versus temperature of 12 ASICs for a total of 192 channels is shown in figure 52. The response of the front end electronics exhibits excellent uniformity at cryogenic temperatures. As shown in figure 53, the gain variation of a cold motherboard with 12 ASICs is only  $\sim 7\%$  peak-to-peak across 192 channels. The spread of the gain variation is only  $\sim 1\%$  of the gain setting.

## 6.2 Warm Electronic Amplification

Signals from the cold electronics are carried over the cold cables to dedicated feedthroughs mounted on the cryostat. The cold cables are connected to pin-carriers located on 14-inch CF signal feedthrough flanges that are mounted on nozzles N1A-N1K of the cryostat (see figure 5). The signal feedthrough design must accommodate 100% hermeticity and high signal density. A design based on the ATLAS pin carrier style was developed for this purpose. Two 8-row pin carriers and two 7-row pin carriers are welded onto the 14-inch CF flange, as shown in figure 54, and create a vacuum-tight seal. Nine of the 11 signal feedthroughs receive signals from the three LArTPC anode planes (384 Y-plane, 192 U-plane, 192 V-plane), while the remaining two on the extreme ends of the cryostat only receive signals from one of the angled Induction planes (672 U-plane on one feedthrough, 672 V-plane on the other).

A Faraday cage is mounted on the external, warm, side of the signal feedthroughs to provide shielding for the intermediate amplifiers located inside. The bias voltage feedthrough, which supplies anode plane bias voltages into the cryostat, is built onto a small 2.75-inch CF flange welded onto the signal feedthrough flange. A filter board mounted on the bias voltage flange filters noise

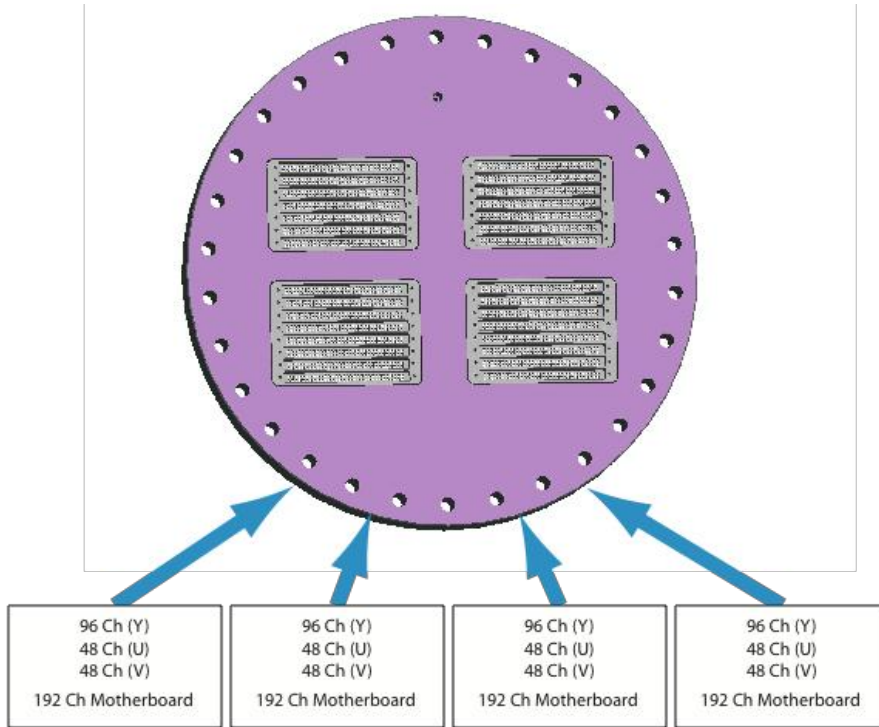


Figure 54: Signal feedthrough flange consisting of a 14-inch CF flange with two 8-row and two 7-row pin carriers welded in place.

<sup>1</sup> and ensures a good ground connection. Figure 55 shows details of the signal feedthrough assembly with electronics boards, bias voltage feedthrough, and Faraday cage.

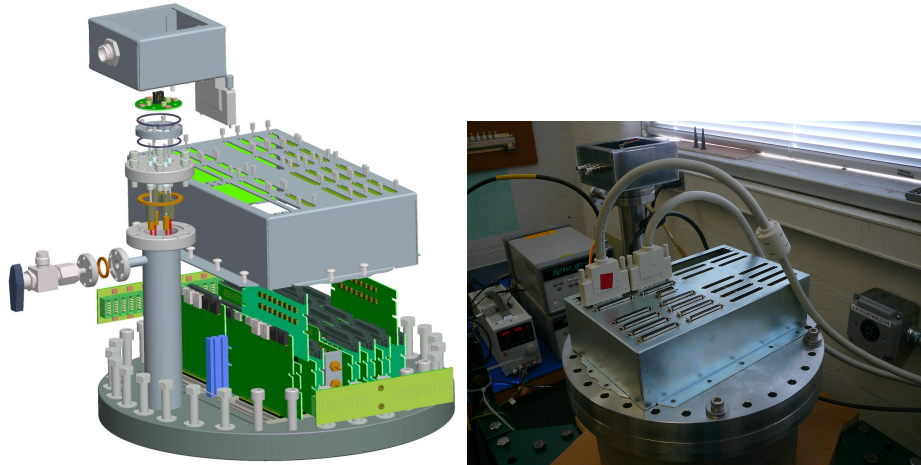


Figure 55: Left: Diagram of the signal feedthrough assembly, which includes intermediate amplifiers, Faraday cage, bias-voltage feedthrough and filtering circuit. Right: Photograph of one of the feedthrough assembly, partially constructed and being tested.

1     The intermediate amplifiers provide  $\sim$ 12 dB gain to the LArTPC signals to make them suitable  
2     for transmission over a 20 m long cable to the readout electronics (see section 6.3). Each  
3     intermediate amplifier has 32 channels installed on the signal feedthrough flange and housed inside  
4     the Faraday cage to provide noise isolation. Figure 56 shows a picture of a prototype intermediate  
5     amplifier plugged on the signal feedthrough pin carrier. The intermediate amplifier uses a 68-pin  
6     SCSI-3 connector to drive the 32 channels of signal differentially for better noise immunity. The  
7     layout and connector position have been carefully designed to ensure the card can be plugged on  
8     the pin carrier in either direction. This efficiently utilizes the limited available space on the top of  
9     the feedthrough, which also makes the design of the Faraday cage easier.

10    In addition to the intermediate amplifiers, there are two service boards mounted on the top of  
11    each signal feedthrough. The service board provides regulated low voltage, control and monitoring  
12    signals to the analog front end ASICs. It also provides pulse injection to the preamplifiers for  
13    precision calibration. The control, monitoring, and calibration signals are provided to the front end  
14    electronics with two-fold redundancy. Should one set of signals become defective the detector can  
15    still operate normally with the redundant set. Each service board plugs onto a 64-pin carrier row.  
16    Figure 56 shows a picture of a prototype service board.



Figure 56: Left: Photograph of one of the intermediate amplifier boards plugged into a pin carrier during testing. Right: Photograph of a prototype service board.

### 17    6.3 LArTPC Readout Electronics

18    The MicroBooNE Readout Electronics system consists of two subsystems: the LArTPC and PMT  
19    readout electronics. The LArTPC readout electronics are responsible for the readout, digitization,  
20    and processing of the induction and collection wire signals after amplification. The PMT readout  
21    electronics are responsible for the amplification, shaping, digitization, and handling of PMT signals,  
22    as can be used to provide a trigger signal for the readout and data acquisition systems. While  
23    the LArTPC and PMT readout systems share the same back-end design that organizes and packages  
24    the data for delivery to the DAQ system, they employ different analog front-end and digitization  
25    designs, which are described in this and the following subsection.

26    The LArTPC readout electronics are responsible for processing the signals from the 8,256  
27    wires in MicroBooNE after pre-amplification and shaping in the cold electronics (section 6.1).  
28    The pre-amplified and shaped analog signals from the cold electronics are transmitted to the warm

1 electronics outside the cryostat, as described in section 6.2, and then passed to custom-designed  
2 LArTPC readout modules distributed evenly over nine readout crates. The readout modules digitize  
3 the analog signals and then process and prepare them for shipping to designated DAQ machines  
4 (one per readout crate) (section 6.6).

5 The LArTPC readout crates communicate with the DAQ machines via three duplex 3.125  
6 Gbits/sec optical links that connect to a crate controller module and data transmitter (XMIT) mod-  
7 ule on the crate end, and to three PCI Express boards on the DAQ machine end. The controller  
8 is responsible for configuration, trigger and run control command distribution as well as the slow  
9 monitoring of each readout crate. The controller occupies one of the optical links while the XMIT  
10 is responsible for sending two separate streams of readout data to the DAQ machines via the two  
11 other optical links. The first XMIT stream contains losslessly compressed LArTPC data associ-  
12 ated with event triggers received by the LArTPC readout crates, such as the BNB trigger, and  
13 is referred to as the “NU” data stream. The second stream is a continuous LArTPC data stream  
14 which is compressed with some data loss. The continuous data stream is used for beam-unrelated  
15 physics analyses, such as the study of potential supernova neutrino events, and is referred to as  
16 the “SN” data stream. The compression schemes used in the NU and SN streams are described in  
17 section 6.3.3.

18 All readout crates are synchronized to a common 16 MHz clock. The clock sync is provided  
19 by a clock fanout board which shares the same ground as all readout crates, and is sent via coaxial  
20 cable to a distribution board which is mounted on each crate backplane. The readout frame size  
21 is set to 1.6 ms, which is equivalent to the time it takes for charge produced on the far end of the  
22 LArTPC to drift to the wire planes at the design cathode voltage of -128 kV.

### 23 **6.3.1 LArTPC Data Digitization**

24 The amplified and shaped analog LArTPC signals are differentially received and digitized in the  
25 first section of the readout modules. Each ADC module holds 8 AD9222 octal-channel 12-bit  
26 ADCs. Each ADC module handles signals from 64 wires. The wire signals are grouped in two  
27 sets of 32 consecutive wire channels: either 32 induction wires plus 32 collection wires or two sets  
28 of 32 induction wires. The induction channel sequence alternates wires between the two induction  
29 planes. The ADC module digitizes the signals continuously at 16MHz. Each channel has a config-  
30 urable baseline, which is either set low (450 ADC counts) for collection channels or at the middle  
31 of the dynamic range (2055 ADC counts) for induction channels, thus ensuring that both the collec-  
32 tion plane unipolar differential signals and the induction plane bipolar differential signals can make  
33 use of the full ADC analog input range. The requirement to observe a MIP produced at the far end  
34 of the LArTPC in the induction plane determines the lower end of the dynamic range, while the  
35 requirement to observe a highly-ionizing stopping proton at the close end of the LArTPC without  
36 saturation sets the higher end. The digitized outputs from the ADC board are passed directly to a  
37 Front End Module (FEM) in the second section of the LArTPC readout module. The FEM houses  
38 an FPGA for data processing, data reduction, and preparation for readout by the DAQ system as  
39 described in the following section.

### 40 **6.3.2 LArTPC Data Handling**

41 The FEM board consists of a 14-layer printed circuit board which is mechanically integrated with

1 the ADC board as illustrated in figure 57. The choice of a smaller board allows for short trace  
2 lengths which is beneficial for high speed signals. The full assembly comes together as a standard  
3 VME 9U card in height, with a 280 mm depth. Differential outputs from the ADCs connect to the  
4 FPGA through HM-Zd connectors that have individual ground shielding on each differential pair.

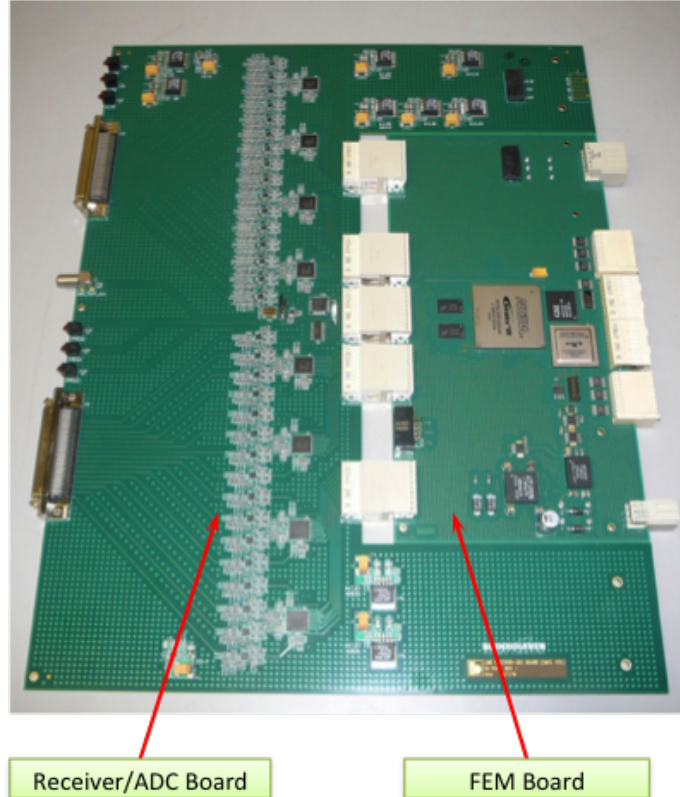


Figure 57: LArTPC ADC+FEM board.

5 The digitized data stream moves from the ADCs to a Stratix III Altera FPGA, which reduces  
6 the sampling rate of the ADC from 16 MHz to 2 MHz. The 2 MHz sampling rate is optimized by  
7 taking into consideration the expected pulse shape provided by the convolution of the cold electron-  
8 ics, the expected LArTPC field responses, and the  $O(1\mu s)$  diffusion effects which govern charge  
9 drift within the liquid argon. The FPGA stores the data from all 64 wires per board sequentially  
10 in time in a  $1M \times 36$  bit 128 MHz SRAM memory, grouping two ADC words together in each 36  
11 bit memory word. This requires a data storage rate of  $(64/2) \times 2$  MHz = 64 MHz. The SRAM  
12 chip size and memory access speed allow for continuous readout of the LArTPC data. Since data  
13 reduction and compaction algorithms rely on the sequential time information of a given wire, the  
14 data readout out from this SRAM memory takes place in wire order in alternate clock cycles, again  
15 at the rate of 64 MHz. This read in/out sequence is illustrated in figure 58.

16 Separate DRAM multi-event buffers on the FEM store the NU and SN data streams. The data  
17 divert into the NU readout stream when a trigger is issued and received (as shown in figure 59)  
18 which signals, for example, an accelerator neutrino-induced event. When an event trigger is re-  
19 ceived, 4.8 ms worth of data, relevant to that event, are packeted per channel and sent to the DAQ

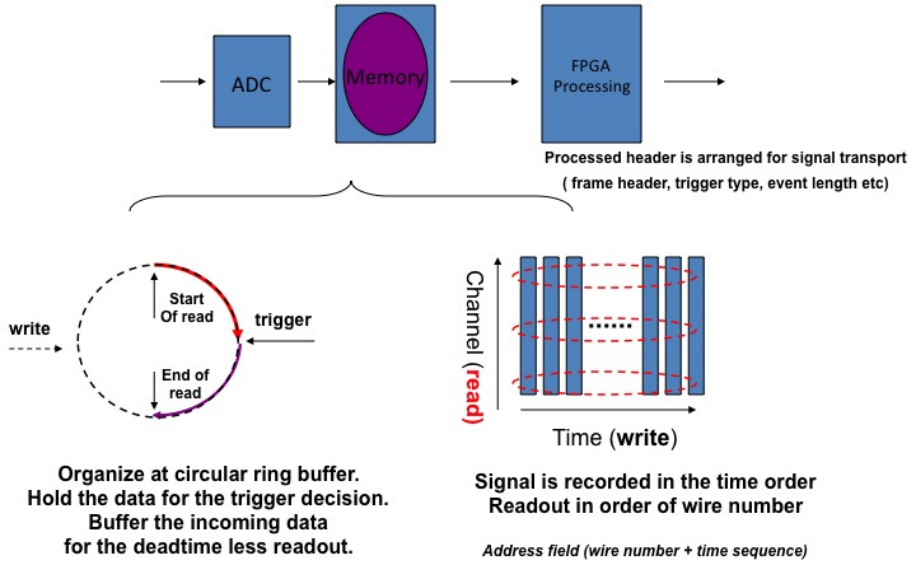


Figure 58: LArTPC readout sequence in the TPC FEM.

through the NU data stream. The 4.8 ms readout size is governed by the maximum drift time and spans three or four frames. In order to reduce the amount of data being transmitted, the FPGA trims the three or four frames to span the exact 4.8 ms required, 1.6 ms before the trigger plus 3.2 ms after the trigger. In parallel, the data is continually sent out through the SN data stream, frame by frame. The compaction and data reduction algorithms applied to each of the two streams are described in the following section.

After processing by the FPGA, the data passes to the crate backplane dataway on connectors shown in figure 57. A token-passing scheme is utilized to transfer data from each FEM board to the data transmitter module (XMIT) in a controlled way, whereby each FEM, in the order of closest to furthest from the XMIT module, receives a token, transmits its data to the XMIT, and passes the token on to the next FEM in the sequence. For the NU stream, each FEM sends all data associated with a particular trigger number; while for the SN stream, each FEM sends all data associated with a particular frame number. This data transfer is relayed via the otherwise passive crate backplane, and is limited to 512 MB/s. In the XMIT module, the data is buffered temporarily and sent to the DAQ machine through the two streams, SN and NU, which proceed effectively in parallel.

### 6.3.3 LArTPC Compression Schemes

In the case of the NU data stream, a lossless Huffman coding scheme implemented in the FEM FPGA compacts the data by approximately a factor of five. Further reduction in the overall rate is achieved by exploiting a PMT trigger in coincidence with the BNB trigger, as described in section 6.5. Huffman coding provides for lossless data compression by taking advantage of the slow variation of the waveform TPC data in any given channel. In particular, this compression scheme relies on the fact that successive data samples on any given wire vary relatively slowly in

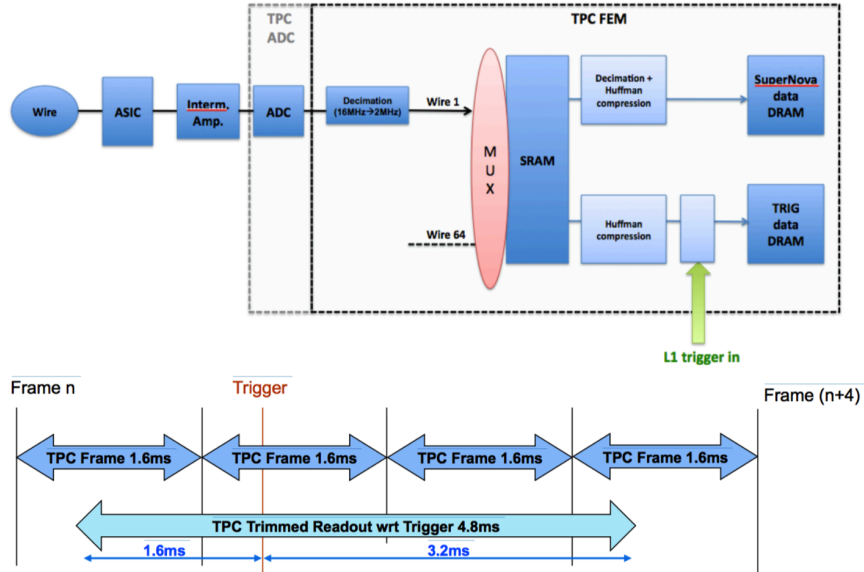


Figure 59: LArTPC trigger readout.

time. As such, when noise levels are low, any two adjacent data samples either coincide or differ by 1 ADC count. The most frequent values for the difference in ADCs between successive data samples are assigned pre-specified bit patterns with the lowest number of bits possible. Those bit patterns are compacted in the 16-bit data words that would otherwise be used for a single 12-bit ADC sample value. As such, data reduction of up to a factor of 14 is theoretically possible<sup>1</sup>. In practice, the data reduction is sensitive to noise levels and LArTPC activity, and is also dependent on the gain setting. The compression factor achieved by MicroBooNE is shown in figure 60.

Because of the low trigger rate<sup>2</sup>, lossless Huffman coding compression proves sufficient for the NU data stream. However, for the continuous SN stream, further compression becomes necessary, resulting in unavoidable data loss. A method called “dynamic decimation” (DD) handles this case. The DD scheme relies on recognizing regions of interest (ROI) in the data stream that contain waveforms corresponding to drift ionization charges. Portions of the data stream not containing ROI contribute to pedestal determination, and ROI are identified as deviations from the continually-updated pedestal, buffered, and read out to disk. At the time of this writing, the MicroBooNE SN stream compression scheme is being finalized and the SN readout stream will be commissioned in September 2016.

#### 6.4 PMT Readout Electronics

The PMT readout electronics are responsible for processing signals from the 32 PMTs described in section 5 and identifying light signatures coincident with the BNB and NuMI beam spills. The coincidences generate PMT triggers that can be later mixed with other triggers in the Trigger Board

<sup>1</sup>The uppermost two bits are always reserved for header information, in each 16-bit word.

<sup>2</sup>The BNB trigger dictates an upper bound on the trigger rate of 15 Hz.

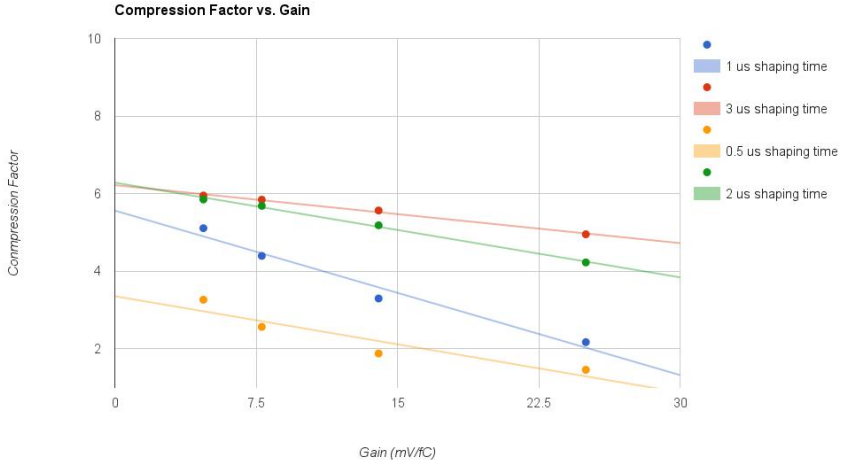


Figure 60: Compression factors achieved on ADC data with Huffman compression.

1 (TB). Signals from the 4 light paddle guides installed in the LArTPC are also recorded by the PMT  
2 readout electronics, but these signals do not participate in the PMT trigger generation.

3 The stages of signal processing are illustrated in figure 61. First, each PMT signal (with the  
4 exception of the light paddle guide signals) is split into two different gains, as described in sec-  
5 tion 5.2.5, with the HG channel carrying 18% of the PMT signal and the LG channel carrying  
6 1.8% of the PMT signal. Each gain is split once again into HG1 and HG2, and LG1 and LG2, in  
7 order to allow different processing of beam-related and beam-unrelated PMT signals. All  $32 \times 2 \times 2$   
8 plus 4 signals are pre-amplified and shaped in 16-channel pre-amp/shaper boards (section 6.4.1).  
9 Four PMT readout modules receive the analog shaped signals differentially and digitize them (sec-  
10 tion 6.4.2) at 64 MHz. The PMT readout modules then process the signals in order to prepare them  
11 for shipping to a designated DAQ machine and to form a possible PMT trigger (section 6.4.3).

12 Each one of the 4 PMT ADC+FEM readout boards used in the PMT readout system handles  
13 one of the following:

- 14     • Readout of and PMT trigger generation using the HG1 PMT signals associated with neutrino  
15       beam events. The paddle signals are also readout by this board.
- 16     • Readout of and PMT trigger generation using the HG2 PMT signals that are out of beam  
17       time (i.e. cosmic rays and other cosmogenic backgrounds)
- 18     • Readout of the LG1 PMT signals associated with neutrino beam events
- 19     • Readout of the LG2 PMT signals that are out of beam time

20 After signal processing, the data is sent to a designated DAQ machine via a transmitter (XMIT)  
21 module in the same way as is done for LArTPC data. Two data streams are provided: a NU data  
22 stream associated with event triggers and a SN data stream which a continuous version of the NU  
23 stream readout.

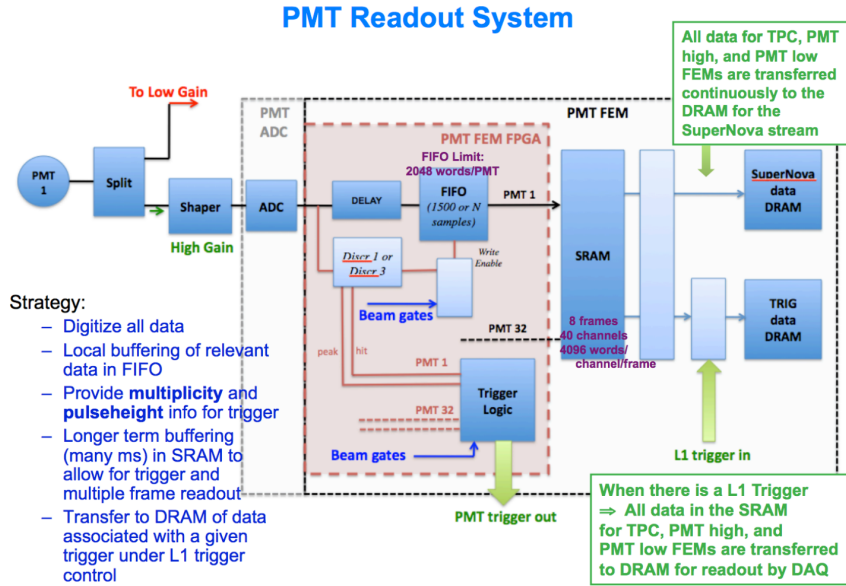


Figure 61: Signal processing in PMT FEM.

#### 1 6.4.1 Signal Amplification and Shaping

2 The preamp/shaper boards read raw PMT signals from the PMT HV/signal splitters and shape them  
 3 into unipolar signals with a 60 ns rise time. The shaped signals are sent to the LArTPC readout  
 4 boards differentially via short front-panel cables, in order to minimize noise, where they are digi-  
 5 tized at 64 MHz. The 60 ns peaking time allows digitization of two or three samples on the rising  
 6 edge. This in turn enables an accurate determination of the event start time ( $t_0$ ) needed to determine  
 7 the  $x$  coordinates of ionization signals along the drift direction. An accurate time measurement also  
 8 helps reject other tracks, such as cosmic rays, that cross the detector during the drift time.

<sup>1</sup> **6.4.2 PMT Data Digitization**

<sup>2</sup> The ADC module part of the PMT readout board (figure 62) is responsible for digitization of up  
<sup>3</sup> to 48 differentially-driven input signals. The differential signals are digitized at 64 MHz. The 64  
<sup>4</sup> MHz clock used by the PMT readout is generated starting from the 16 MHz clock that is common  
<sup>5</sup> to all readout crates (LArTPC and PMT).



TEMPORARY  
PLACEHOLDER

Figure 62: The PMT readout board digitizes 48 input signals. **NOTE: Missing Image!**.

<sup>6</sup> In addition to HG and LG waveforms from the PMTs, each readout board also receives, digitizes,  
<sup>7</sup> and processes beam gate signal markers which arrive  $4\mu s$  before the BNB  $1.6\mu s$  and NuMI  
<sup>8</sup>  $10\mu s$  beam gates. These gates are used to (a) specially mark regions of interest where PMT data  
<sup>9</sup> are read out continuously with no compression and (b) look for coincident PMT light signatures  
<sup>10</sup> for trigger generation.

<sup>11</sup> **6.4.3 Data Handling and PMT Trigger Generation**

<sup>12</sup> PMT information is recorded in the NU data stream for four 1.6ms frames associated with an event  
<sup>13</sup> trigger: the frame containing the (asynchronous) trigger, the frame preceding the trigger frame,  
<sup>14</sup> and two frames following the trigger frame. To avoid the inordinate amount of data that would  
<sup>15</sup> be generated at a 64 MHz sampling rate, the FEM applies a zero-suppression immediately after  
<sup>16</sup> digitization, retaining only samples above a given threshold as well as enough information before  
<sup>17</sup> and after this useful data to establish a local baseline value; this collection of information is referred  
<sup>18</sup> to as a PMT readout ROI. An exception is formed for beam-related or other likewise-triggered data  
<sup>19</sup> where, for example, the  $4\mu s$ -early BNB and NuMI beam gates mentioned in section 6.4.2 instruct  
<sup>20</sup> readout of 1500 consecutive samples ( $23.4\mu s$ ) surrounding and including the beam gates regardless  
<sup>21</sup> of signal activity.

1 Two different discriminators are used: one that is active inside the beam gate(s), and one  
2 that is also active outside the beam-gate-surrounding  $23.4\mu\text{s}$ . The latter discriminator governs the  
3 readout activity due to cosmic rays and other non-beam related activity. The first discriminator  
4 enables PMT channels with pulse heights above a configurable threshold (e.g. corresponding to 1  
5 photoelectron) to participate in trigger multiplicity and pulse height sum conditions, as described  
6 in the following section. The thresholds for those two discriminators are set to different levels and  
7 configured with different dead times for the HG and LG signals.

## 8 **6.5 Level-1 Trigger Generation**

9 The TB, which physically resides in the PMT readout crate, issues a “Level-1” trigger in order to  
10 flag frames that must be treated differently. In the case of the LArTPC readout, the TB flags the 4  
11 frames that must be trimmed and readout through the NU data stream and, in the case of the PMT  
12 readout, it flags the 4 frames that must be readout in full through the NU data stream.

13 The inputs to the TB include a BNB trigger input (maximum rate of 15 Hz), a NuMI trigger  
14 input (1.25 Hz), a Fake Beam trigger input (configurable), a PMT trigger input, and two calibra-  
15 tion trigger inputs, provided by the Laser calibration system and the cosmic ray muon telescope,  
16 respectively. The TB also has the ability to receive, via the crate controller, DAQ-issued calibration  
17 triggers, which are used explicitly for cold electronics and PMT calibration. The various input  
18 triggers can be independently pre-scaled, masked, and mixed together (OR or AND) to generate an  
19 event trigger.

20 The FPGA firmware in the PMT FEM can generate two different types of PMT triggers based  
21 on the PMT signals: a cosmic PMT trigger and a beam gate PMT trigger. Beam gate PMT triggers  
22 are configured in the same way for the BNB, NuMI, and Fake Beam. The nominal criteria for these  
23 triggers are (1) PMT multiplicity  $\geq 1$  and (2) summed PMT pulse-height  $\geq 2$  photoelectrons (p.e.)  
24 summed over all 32 HG1 PMT channels. Both criteria must be met during any 100 ns time interval  
25 coincident with the beam spill duration ( $1.6\mu\text{s}$  in the case of the BNB and Fake Beam gates and  
26  $10\mu\text{s}$  in the case of the NuMI gate), and only channels enabled by the beam gate discriminator can  
27 participate in the active pulse-height and multiplicity sums. The criteria for a cosmic PMT trigger  
28 are (1) PMT multiplicity  $\geq 1$  and (2) summed PMT pulse-height  $\geq 40$  p.e. summed over any one of  
29 28 preset groups of 5 HG2 PMT channels that are grouped based on their spatial correlation. Again,  
30 only channels enabled by the cosmic discriminators can participate in the trigger generation.

31 In addition, a software-based algorithm has been written to mimic the capabilities of the beam  
32 gate PMT trigger performed in the FPGA and provide more flexibility in trigger criteria settings.  
33 Details of this higher-level software trigger are described in section 6.7.

34 Figure 63 diagrams the PMT readout and trigger logic. Activation or masking of each of the  
35 trigger inputs and outputs is DAQ-controlled. The trigger condition and explicit PMT trigger type,  
36 if applicable, is available for every event in the NU data stream at the event building stage as well  
37 as offline as this information is readout through a dedicated optical data stream directly from the  
38 TB. The trigger number and trigger time are also propagated and available in the NU data streams  
39 arriving at the assembler DAQ machine independently from each LArTPC and PMT crate and can  
40 therefore be used to correctly associate data from the same event for every event.

41 The readout control sequence is illustrated in figure 64. When a trigger is generated by the  
42 TB it is passed to a fan-out module on a single cable and from there it is distributed to all crate

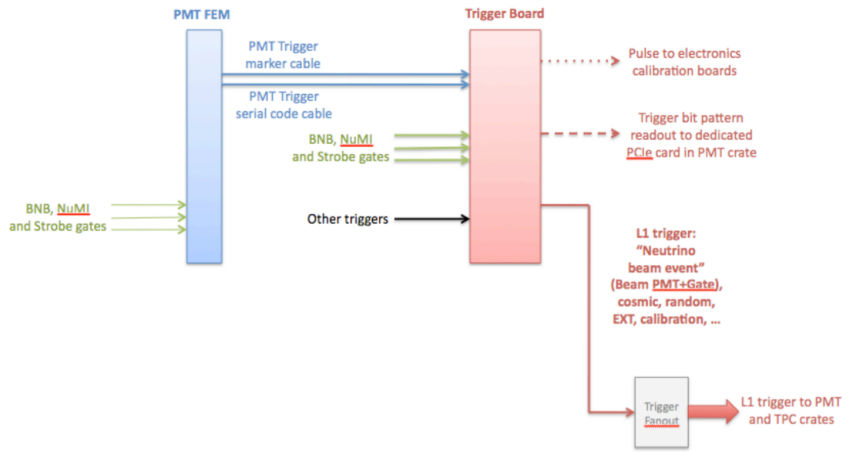


Figure 63: PMT readout and trigger logic.

1 controllers (LArTPC and PMT). Through the crate backplane, the trigger gets propagated to each  
 2 FEM. An FEM that receives a trigger temporarily inhibits the SN stream with its associated deci-  
 3 mation and initiates the loss-less readout scheme to direct the data to the appropriate readout path.  
 4 SN readout resumes once the XMIT is done sending all NU data associated with an event to the  
 5 DAQ.

## 6 6.6 DAQ Design

7 The MicroBooNE DAQ system acquires data from the readout electronics, writes data to local disk  
 8 before transferring it to long-term storage, configures and controls the readout electronics during

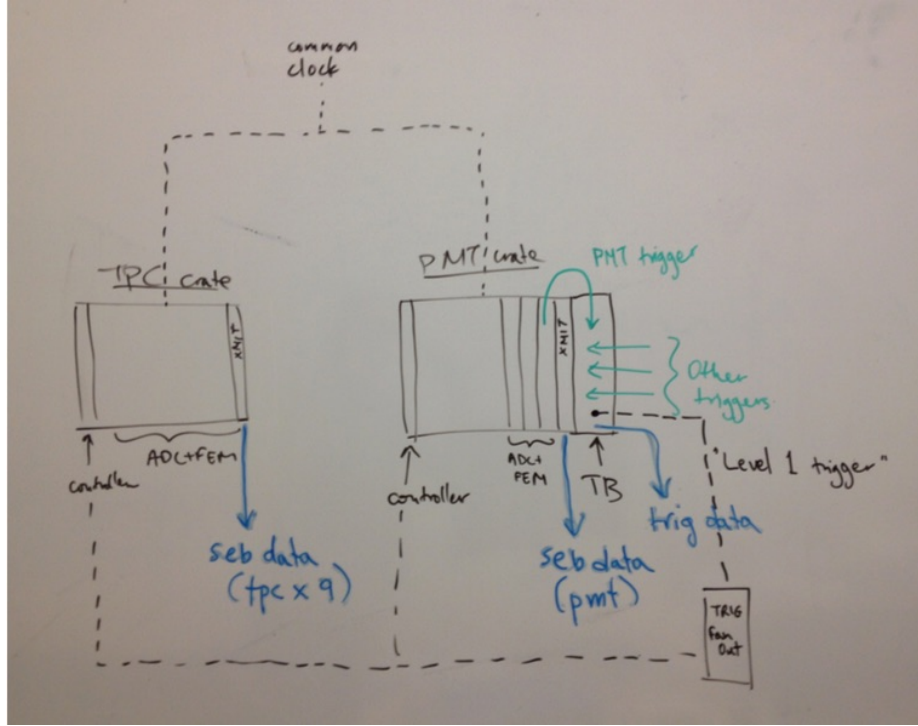


Figure 64: Readout control sequence. The MicroBooNE Level-1 trigger is a hardware trigger which consists of the OR between a BNB, NuMI, and EXT (strobe) trigger. Once received, the Level-1 trigger is propagated to all readout crates and instructs PMT and TPC data readout into ten dedicated sub-event buffer DAQ machines. The data across different DAQ machines is correlated at event building stage by the trigger number and corresponding trigger frame and sample numbers recorded in each data stream, per event. All readout crates are synchronized and correlated to the same, 16 MHz clock. **NOTE: Placeholder figure!**

1 data-taking periods, and monitors the data flow and detector conditions. These tasks are performed  
 2 on a network of commodity servers running both custom and open-source software.

3 The data from each crate of the backend electronics is sent to a dedicated server (called the  
 4 sub-event buffer, or SEB) via an optical fiber. The data arrives in a card on the SEB's PCIe bus  
 5 where a real-time application places data in an internal buffer, collects all of the data belonging  
 6 to an event, and creates a sub-event fragment that may be routed to a specified destination. For  
 7 the NU stream, in which the data arrives with every trigger, these fragments are sent to a single  
 8 event-building machine (EVB) over an internal network. Full events are checked for consistency  
 9 and written to local disk on the EVB before being sent offline for further processing. A high-level  
 10 software trigger, described in section 6.7, is applied to the data to determine whether events should  
 11 be written locally or ignored. For the SN stream the data remains on the SEB where it is written to  
 12 disk and only sent for offline analysis on explicit requests.

13 Data writing to either triggered or SN streams is limited by the RAID6 disk write speeds which  
 14 are roughly 300 MB/sec. This is much less than the network bandwidth bottleneck, which is 10  
 15 Gbps. The 300 MB/sec disk write speed therefore sets the maximum aggregate rate at which all

1 SEB fragments can ship data to the EVB without loss of data. With Huffman compression, which  
2 gives a data reduction of approximately a factor of five (figure 60) and the PMT trigger, which  
3 reduces the data rates by another factor of  $> 70$ , this is more than sufficient for MicroBooNE's  
4 maximum 15 Hz beam spill rate. MicroBooNE expects a total triggered write rate of around 12  
5 MB/sec. The SN stream circular buffers, which will be aggressively (non-losslessly) compressed  
6 beyond what the triggered stream experiences, will fill each server's 14 TB in on the order of one  
7 day, which is ample time to respond to a Super Nova Early Warning System (SNEWS) alert [?].

8 After data is written to disk, it is then copied to another server on the internal DAQ network,  
9 where the raw data is further compressed, shipped, and queued to be stored on in tape and disk  
10 cache using the Fermilab central data management system known as SAM. Offline applications  
11 then begin processing the raw data in a "swizzling" routine, converting the binary data format int a  
12 LArSoft ROOT-based format which can be used as input for reconstruction algorithms. A separate  
13 process collects beam data and, during swizzling, inserts that data into the built events. A duplicate  
14 copy of the triggered swizzled data is also stored offsite at Pacific Northwest National Laboratory  
15 (PNNL). This collection of approximately 15 "projects" and the database which holds and moni-  
16 tors the state of the data flow is known as the Python/Postgres for MicroBooNE Scripting system  
17 (PUBS), and is patterned after a similar database state machine that the Double Chooz experiment  
18 used for data management. As PUBS pushes the data through this process, the progress of each  
19 project is monitored and viewable via GUI. PUBS can also monitor the state of the SN stream data,  
20 held locally on the SEBs. A separate offline PUBS instance controls the processing of the swizzled  
21 data including applying newly calculated calibration constants as part of data quality management.  
22 Figure 65 schematically depicts the flow of data throughout the MicroBooNE experiment.

23 Additional software components handle the management of the main DAQ processes moving  
24 the data. A run control application issues configuration and state-progressing commands to the  
25 SEBs and EVB. Configuration states are stored in a dedicated run configuration database, which  
26 allows for the setting and preserving of configuration information for the DAQ, readout, and addi-  
27 tional components. This database not only allows for creating the large ( $\sim 200$  parameters) intricate  
28 DAQ run configuration files, but also enforces certain conditions which must hold for consistency.  
29 For example, the configuration that initiates the ASICS charge-injection calibration also dials and  
30 captures the settings on the external pulser that drives the calibration signal and assures that ASICS  
31 gains and peaking time parameters are enforced and recorded.

32 Another important aspect of the system is monitoring the health of the DAQ. Monitoring of  
33 DAQ components is accomplished through Ganglia which monitors basic system states (such as  
34 CPU, memory, and network usage) as well as allows use of custom metrics to monitor the data flow  
35 and status of the readout electronics [?]. These metrics are sampled and collected by the EPICS  
36 slow monitoring and control processes, which archives desired quantities and provides alarms when  
37 pre-defined thresholds are exceeded [83]. Some examples of Ganglia metrics that are monitored  
38 and alarmed in EPICS are the rates of growth of the SEB data buffers, the fragment rates leaving  
39 each SEB, and fragment arrival rates at the EVB. Figure 66 shows some examples of Ganglia  
40 metrics.

41 Additional online monitoring exists to check data quality in more detail, through both pro-  
42 grammed checks and visual checks including a real-time event display. The online monitoring  
43 takes snapshots into shared memory segments on the SEBs and the EVB, and thus provides the

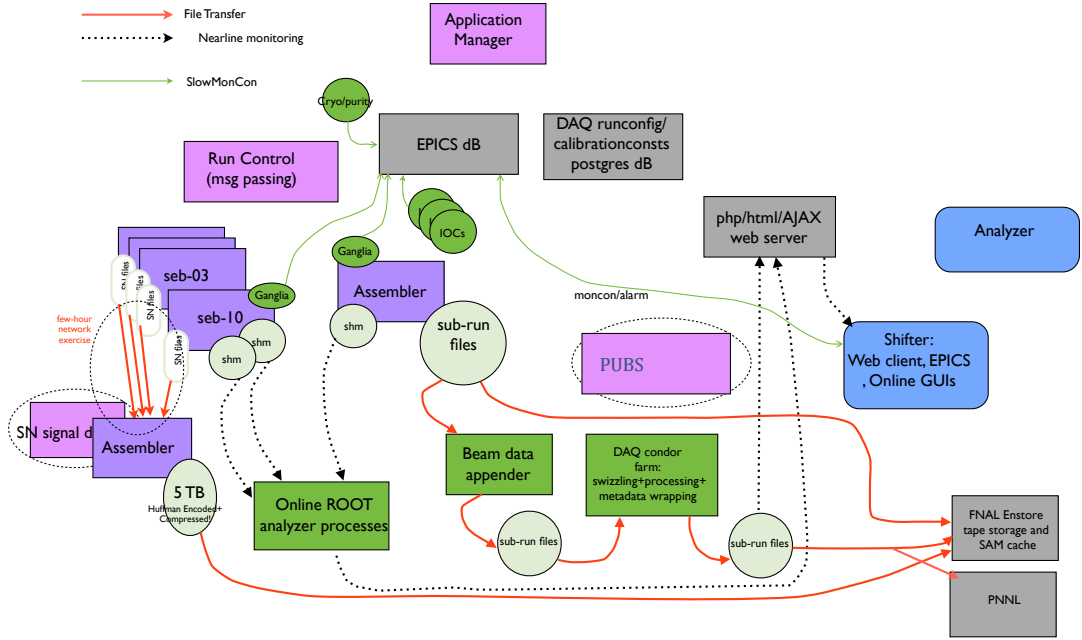


Figure 65: Data flow for MicroBooNE DAQ from raw to processed.

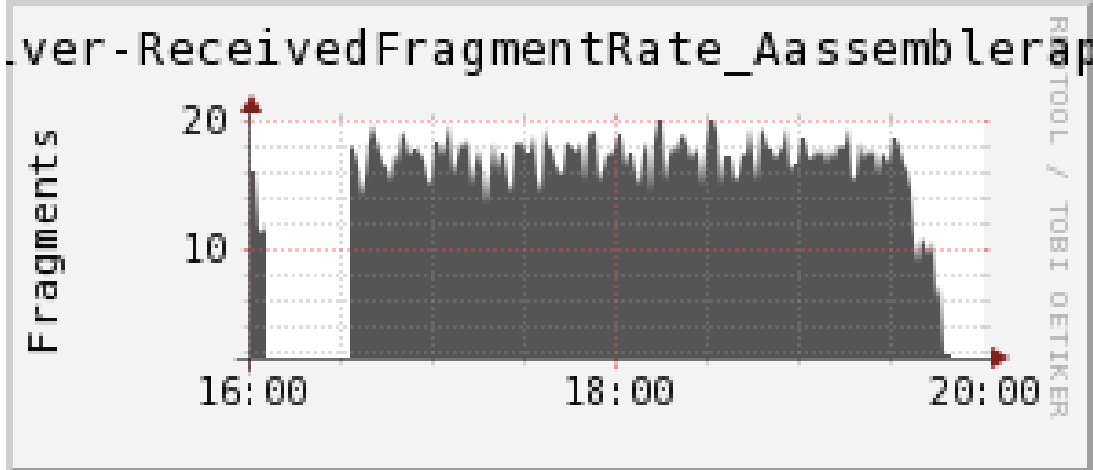


Figure 66: Ganglia metrics showing data flow on the EVB machine during a 2 Hz test run. (ul) the event disk write rate (ur) The number of assembled queued-up events waiting to be written (ll) The total EVB received data rate, and the (lr) received fragment rate.

<sup>1</sup> desired low latency checks of newly-arriving data. It continually walks through these  $\approx 150$  MB snap-shotted events and outputs histograms of occupancies and rates which are saved in ROOT files <sup>2</sup> [?]. The histograms are then displayed in a web-based monitoring system that is easily accessible

1 by the shift crew. Channels are aggregated in a variety of formats, including the order in which  
2 they appear in crates or across the wires and PMTs themselves. In this way, potential problems  
3 across connectors or crates, for example, may be more readily identified. Noisy, quiet, and unre-  
4 sponsive channels are easily marked and displayed to the shift crew. Figure 67 shows an example  
5 of available online monitoring information.

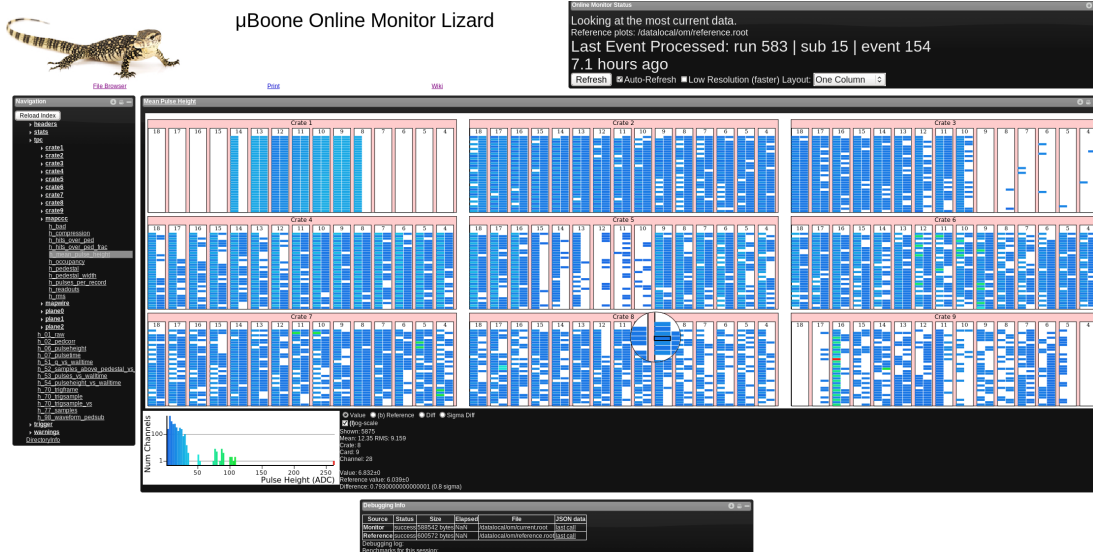


Figure 67: The online monitoring GUI (Lizard). The pedestal-subtracted ADC values for all 8256 wires in one minimum bias event are shown. Each box is a channel. Not all crates are fully populated with electronics.

## 6 6.7 High-level software trigger

7 After events are collected on the DAQ event-builder server, a suite of trigger algorithms are applied  
8 to the data. Currently, these algorithms mimic the PMT readout electronics’ FPGA-based beam  
9 gate trigger algorithms, described in section 6.5. A search over the PMT digitized waveforms from  
10 the beam-spill period is performed, and if there is a significant amount of light in coincidence  
11 with the expected arrival time of the neutrinos, the event is marked and saved. This selection  
12 is performed on data that passes the level-1 trigger, which typically includes data from the BNB  
13 and NuMI beams, and randomly selected off-beam data from an “external” trigger. A fraction of  
14 the data from each of these level-1 trigger input streams is also retained via a random prescale,  
15 which provides a selection of data that has not been biased by the trigger. The high-level trigger  
16 algorithms take approximately 10 ms to return a result, a latency that is well-below the event-taking  
17 rate and so does not impact data-taking performance. The average pass rate for data-events in the  
18 PMT beam gate trigger algorithm is roughly 5%.

## 19 7. Infrastructure and Monitoring Systems

20 MicroBooNE is housed at LArTF, which is located on-axis to the BNB. Complete knowledge of  
21 the electrical and cryogenic systems housed within LArTF is necessary to maintain acceptable

1 operating conditions for the experiment. Continuous monitoring of the beam being delivered to  
2 LArTF is also necessary for subsequent physics analyses. This section describes the details of  
3 infrastructure within LArTF, as well as monitoring of the experiment and beam conditions.

4 **7.1 Electronics Infrastructure at LArTF**

5 This section describes the electronics infrastructure of the MicroBooNE experiment, which is es-  
6 sential for proper operation of the electronics that control the functioning of and extract data from  
7 the LArTPC, PMTs, and other detector subsystems. Figure 68 shows a diagram of this system  
8 for: LArTPC control and readout, light collection system, drift high voltage, purity monitor, cal-  
9 ibration laser, trigger, and cryogenic control systems. Additional server racks containing the data  
10 acquisition, beam timing, and external network electronics are located in a separate computer room  
11 above and adjacent to the above-cryostat platform. The distribution of power, data, and network  
12 connections to and from all of these racks are also presented in figure 68, and is described in more  
13 detail in the following sections, as are electronics safety systems and interlocks.  
14

15 **7.1.1 AC Power Distribution and Grounding for Low-Noise LArTF Data-taking**

16 As with any large detector operating with a high dynamic range, prevention of electromagnetic  
17 interference and its attendant effects on MicroBooNE data is an essential aspect of detector design.  
18 MicroBooNE’s strategy for producing a low-noise environment for the LArTPC and associated  
19 readout electronics can be largely summarized in a few key points. AC power distribution-related  
20 items will be described here, while cabling, connections, and shielding will be described in a  
21 following section.

- 22     • ‘Clean power,’ or AC power electrically isolated from AC power for the rest of LArTF  
23        (‘building power’), is supplied to all sensitive electronics via an isolation transformer.
- 24     • Highly sensitive electronics are housed inside the Faraday cage provided by the detector  
25        cryostat or inside Faraday cages directly grounded to the cryostat.
- 26     • The detector cryostat is grounded to a ‘detector ground,’ which is physically and electrically  
27        isolated from the ground provided to all other LArTF power circuits, or ‘building ground.’
- 28     • No direct electrical connections are present between detector ground and building ground.  
29        This is accomplished through the use of insulating platform and cryostat saddle materials,  
30        insulating cable trays and cables, and by inserting insulating ‘breaks’ (i.e. fiber data links  
31        or insulating cryo pipe sections) when connections between sensitive and potentially noisy  
32        detector components are necessary.
- 33     • Indirect pickup on clean signals through capacitive coupling to adjacent noise sources is  
34        minimized through use of detector-grounded shielding and electrically-insulating cable trays.
- 35     • Ground loops on detector ground are avoided wherever possible by connecting all electronics  
36        racks directly to the cryostat and by minimizing direct electrical connections between racks.

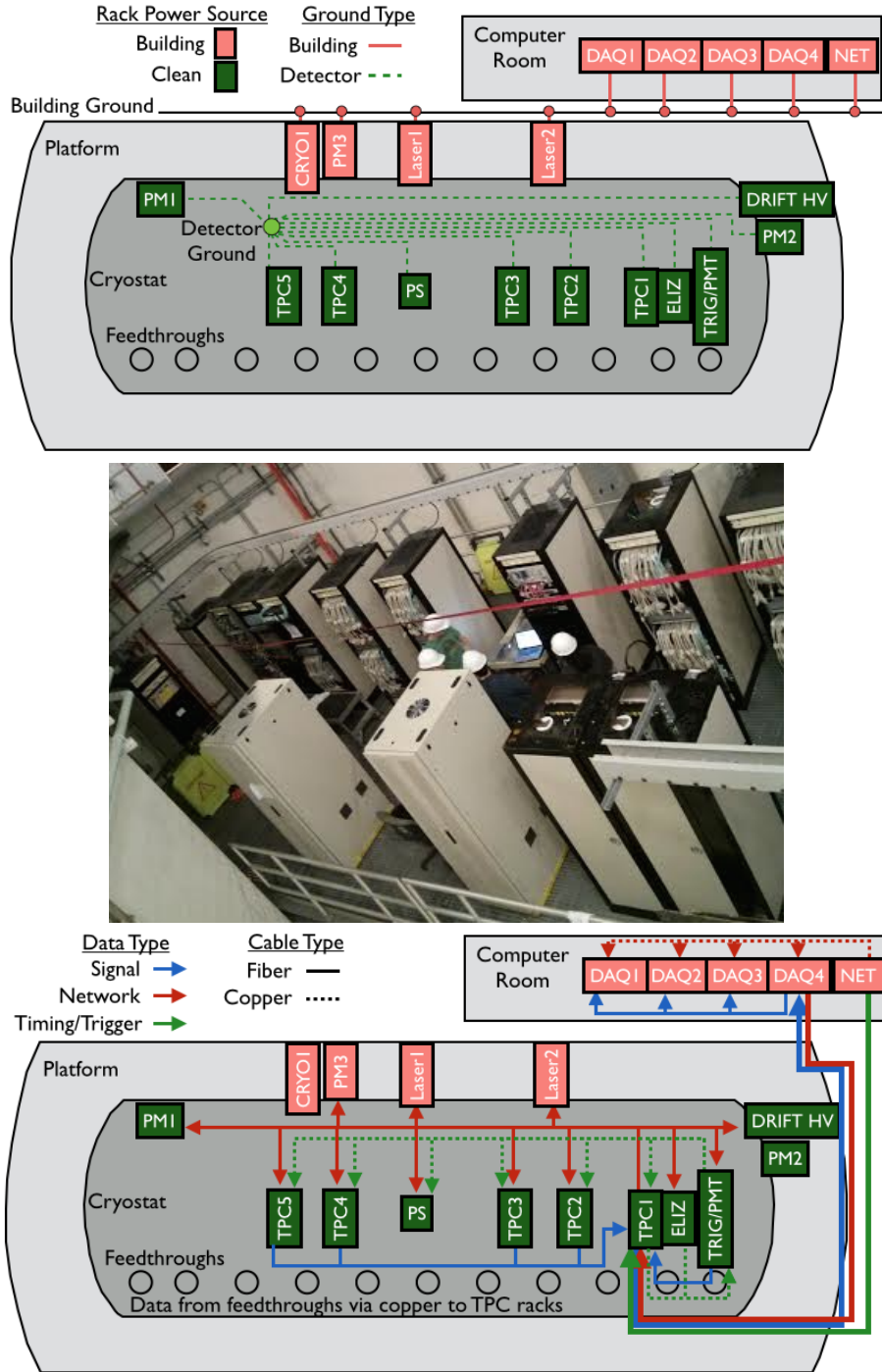


Figure 68: Top: Diagram illustrating location of deployed electronics racks and separation of detector and building grounds and clean and building power for differing racks. Middle: Photograph of installed electronics racks on the LArTF platform. Bottom: A diagram illustrating the general scheme of signal, network, and timing signal cabling in the LArTF computer room and platform.

- 1     • Direct or capacitive couplings between building and detector ground are constantly monitored during installation and operation with a custom-designed impedance monitor.

3     A line drawing describing the production of clean power and clean ground are shown in figure 69. Two 200-Amp clean power circuits produced at isolation transformers are used to power all  
4     5 sensitive racks, which are indicated in figure 68. All racks containing LArTPC readout electronics  
5     are placed on one circuit, while all other sensitive equipment is placed on the alternate circuit. On  
7     the platform, all racks utilize clean power with the exception of the calibration laser and in-line  
8     purity monitor racks, which either contain noise-producing elements or support building-grounded  
9     components. All racks in the LArTF computer room utilize building power.

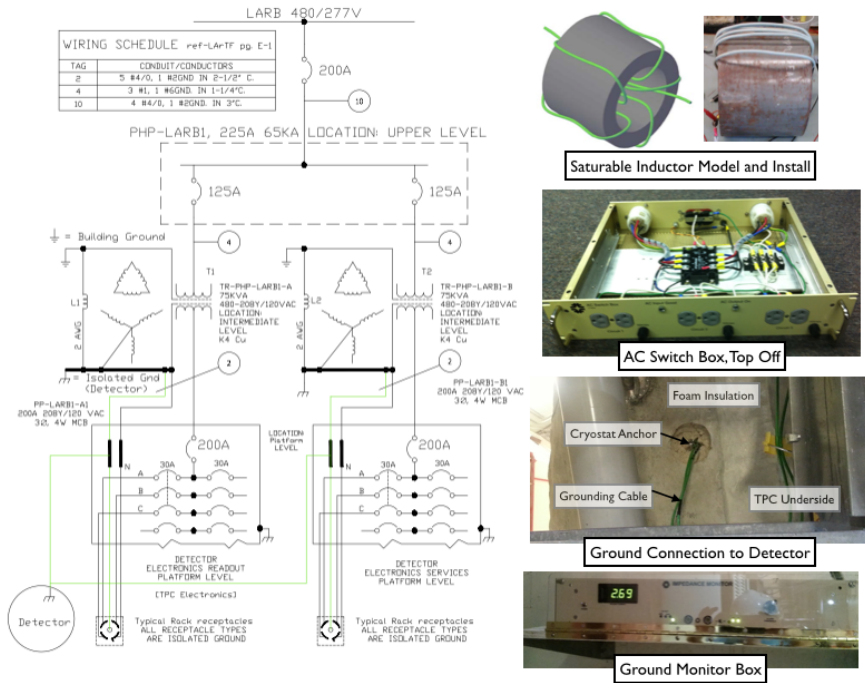


Figure 69: Line drawing of clean power generation and distribution and connections to detector ground, along with pictures of the installed saturable inductor (top), AC switch box (top middle), detector ground strap and connection (bottom middle), and impedance monitor (bottom).

10     208-3phase power is distributed to each individual electronics rack. For racks with significant  
11     power requirements or a large number of components, this power is delivered to a Fermilab-  
12     designed ‘AC switch box,’ which distributes power to an Eaton Power Distribution Unit (PDU)  
13     only upon receiving an interlock signal from a smoke detection system in each rack, which will  
14     be described in more detail below. Rack components then receive power from one of the three  
15     phases on this PDU. For racks with fewer requirements, power is supplied to components directly  
16     from an interlocked simplified AC switch box or SurgeX SX-1120-RT PDU. Racks with sensitive  
17     electronics (listed above) are grounded to the cryostat via copper sheeting running throughout in-  
18     sulated cable trays above the cryostat. Sensitive components within each rack are connected to a  
19     tin-plated copper grounding bar electrically connected to the rack bottom and running the height  
20     of the rack. Mechanical attachments to the rack provide grounding for less sensitive rack com-

1 ponents. As mentioned before, any unintentional direct connection between building and detector  
2 ground can be quickly identified by the impedance monitor located on the LArTF platform.

### 3 **7.1.2 DC Power Distribution to the MicroBooNE Detector**

4 DC power is provided to the LArTPC and readout electronics by power supplies in clean-powered,  
5 detector-grounded racks for a variety of purposes:

- 6     • Holding the LArTPC cathode plane at voltage to produce the desired ionization electron drift  
7         speed
- 8     • Holding the two ungrounded anode planes at the proper constant voltage to ensure the planes  
9         are transparent to drifting electrons
- 10    • Operating the light collection system PMTs
- 11    • Powering the cold electronics located inside the LArTPC
- 12    • Powering the warm electronics located in the LArTPC readout electronics racks
- 13    • Powering auxiliary systems, such as LArTPC temperature sensors and purity monitors

14   Table 7 summarizes the required voltages or currents for each of these purposes as well as the  
15   power supply make and model utilized in each case. Power supplies are located in the relevant  
16   subsystem's electronics rack, with power and grounding connections as dictated by that rack.

Table 7: Overview of MicroBooNE DC power distribution. Delivered voltages or currents are listed, along with power supply makes and models and whether each supply utilizes clean or building power.

Sub-System	Supplied Value	Supply Made/Model	Clean Power?
Drift High Voltage	120 kV	Glassman LX150N12	Y
Anode Plane Voltage	1 kV / 8 mA	Wiener MPOD ISEG_EHS 82 10X_805F	Y
PMT High Voltage	2 kV / 3 mA	BIRA T4	Y
Cold Electronics Power	8 V / 10 A	MPOD MPV 800I	Y
Warm LArTPC/PMT Electronics	+/-5V MDH 2-8V/25A +12V MEH 8-15V/92A +3.3V MEH 2-7V/115A	Wiener PL508	Y
Auxilliary Systems Power	Various	Various	Laser: N Inline PM: N Cryostat PM: Y

17   DC supply power consumption is minimal in most cases, with the exception of the warm  
18   LArTPC electronics PL-508 supplies, which can draw in the vicinity of XXX W during normal  
19   operation. Care was taken to distribute the AC power load by limiting the number of high-draw PC  
20   supplies per electronics rack.

**1    7.1.3 Network, Timing, and Data Distribution for Low-Noise LArTF Data-taking**

**2** Network, timing, and data connections must be made between the detector, building-ground, and  
**3** detector-ground racks to properly read out MicroBooNE data. However, as described above, these  
**4** connections must be made while maintaining strict detector-building electrical isolation. Deployed  
**5** interconnections meeting both of these requirements are displayed in figure 68.

**6**      Timing and LArTF-external network signals are brought into LArTF via electronics in the  
**7** computer room, where all racks are building grounded and powered. These signals are distributed  
**8** and processed in the computer room utilizing copper cable, while network and processed timing  
**9** signals to be sent to the platform are converted onto fiber cables and aggregated into a central fiber  
**10** termination box. A fiber trunk line then delivers these signals to the platform, where another fiber  
**11** termination box on a detector-ground rack is used to fan out these signals. Network connections are  
**12** fanned out via fiber to a network switch in each platform rack, while timing signals are re-converted  
**13** to copper and further processed for use by the trigger system on a different detector-grounded rack.  
**14** All rack-to-rack cables are run in insulating cable trays beneath the platform.

**15**     PMT and LArTPC data are transferred from each detector feedthrough to readout crates in  
**16** detector-ground racks via insulated copper cable whose shield is tied to detector ground. Digitized  
**17** crate output is then sent to the aforementioned platform fiber termination box, where these signals  
**18** are sent via fiber trunk line to the computer room. In the computer room, these fibers are then  
**19** fanned out to the appropriate DAQ computer. Readout crate and cold electronics control commands  
**20** are transmitted in the opposite direction utilizing a similar scheme, with crate controls delivered  
**21** directly via fiber, and cold electronics commands delivered via ranger fiber to a copper fanout in a  
**22** detector-ground rack.

**23**     Clock and trigger signals must also be sent from a central trigger rack to all detector-ground  
**24** LArTPC/PMT readout racks. These signals are transmitted via copper connections, and represent  
**25** the only source of ground loops on detector ground. To further reduce the possible impact of  
**26** induced noise in these and all copper cables mentioned above, all insulating cable trays beneath  
**27** the platform are lined with copper sheeting grounded to the detector. As an additional precaution,  
**28** all LArTPC signal copper cables are run in separate cable trays from power and auxiliary cabling  
**29** beneath the platform as well as inside every rack.

**30**     All cables between all detector components have been uniquely labelled with serial number,  
**31** source, and destination to allow for ease of replacement and reconnection. Ample fiber and copper  
**32** spares for every major cable type are also installed along with the production cables to allow for  
**33** quick replacement of any failed cable.

**34    7.1.4 Interlocks and Safety Systems**

**35** All electronics racks contain smoke-sensing and temperature-monitoring systems, which, when  
**36** interlocked with AC and DC power transmission in each rack, constitute a rack protection system  
**37** (RPS) designed to meet Fermilab safety requirements and reduce the risk of fire and related damage  
**38** in LArTF and to individual rack components.

**39**     The RPS principally consists of a smoke sensor connected to a Fermilab-designed rack pro-  
**40** tection box. This box produces and outputs a 12 V interlock signal when the rack protection box  
**41** is on and receiving a 'no-smoke' signal from the smoke sensor. This 12 V signal can be sent to the

1 AC distribution box located in each rack, as described above, to allow AC transmission to all rack  
2 components only if the RPS is on and not detecting smoke. A similar 12 V ‘RPS Status’ signal  
3 is also produced by the RPS box for input into the MicroBooNE slow control box, which will be  
4 described in following sections. Alternate contacts are available on the rear of the RPS box for  
5 coupling the status of additional subsystems, such as the DAQ and calibration laser uninterruptible  
6 power supply (UPS), to smoke sensor or rack power status.

7 Fermilab-assembled temperature sensors deployed in two or three locations in each electron-  
8 ics rack sample air temperature within each rack. Temperatures at each sensor are read out and  
9 recorded in the slow-control database by the slow-control monitoring box. In addition, the box also  
10 produces a 5 V interlock signal if all sampled temperatures are within pre-programmed thresholds.  
11 In electronics racks distributing PMT- or LArTPC-related DC power these temperature interlock  
12 signals are input into each relevant power supply, allowing DC power distribution only when this  
13 interlock signal is present, for safety purposes.

14 Additional hardware interlocks ensure the non-simultaneous operation of particular subsys-  
15 tems. In particular, when cryogenic system liquid level sensors detect a level below that of the  
16 highest PMT bases, the PMT system should be disabled. In addition, when the UV laser system  
17 is active, PMTs should also be disabled. The former requirement is enforced with a dry-contact  
18 hardware interlock, while the latter is enforced with a software interlock in the MicroBooNE online  
19 software.

### 20 **7.1.5 Performance Measurements**

21 The proper operation of each production electronics rack’s AC and DC distribution and RPS sys-  
22 tems has been tested prior to installation at LArTF. Furthermore, test stands exercising function-  
23 ality of DAQ, PMT and LArTPC electronics, trigger, and drift HV systems have successfully in-  
24 corporated and tested various aspects of these same AC and DC distribution and RPS systems.  
25 Impedances between detector and building grounds were recorded throughout the installation of  
26 the rack infrastructure at LArTF using the impedance monitor located on the LArTF platform.

## 27 **7.2 Slow monitoring and control system**

28 MicroBooNE uses the Experimental Physics and Industrial Control System (EPICS) [83] for con-  
29 trolling and monitoring most devices and conditions important to the experiment. These include  
30 power supply controls, temperatures, fan speeds, rack protection interlock status, and various en-  
31 vironmental conditions. The DAQ, cryogenics systems, and beam data collection systems operate  
32 independently of the EPICS slow monitoring, but export data which are imported into EPICS for  
33 archiving and status displays. Applications from the Control System Studio software collection  
34 [84] are used for providing displays, alarm notifications, and data archiving.

35 An EPICS system consists of any number of server programs implementing the EPICS Chan-  
36 nel Access (CA) protocol [85] to provide client programs access to any number of process vari-  
37 ables, where each process variable represents a quantity being controlled (an output) or measured  
38 (an input). The EPICS base distribution provides a standard type of channel access server called an  
39 Input/Output Controller (IOC), which can be extended to support specific hardware as desired.

40 Most power supplies are controllable over the network through the NetSNMP protocol [86].  
41 Several EPICS driver modules are available for SNMP, and MicroBooNE utilizes one written at

1 NSCL [87]. An IOC with this SNMP module runs on a central computer and contacts the power  
2 supplies over a private network for monitoring and control. The photomultiplier power supplies are  
3 reused from the D0 experiment and have custom IOCs running in their own controllers [?]. The  
4 main high voltage power supply has only a simple RS-232 serial interface; control and monitoring  
5 for it is provided by a nearby computer running an IOC with the EPICS asynDriver [88] and  
6 StreamDevice [89] modules.

7 MicroBooNE has a number of racks in various positions above the detector and in an adjacent  
8 server room. Each is equipped with a rack-protection system and multiple digital temperature sen-  
9 sors, and most contain one or two fan packs, each containing 6 fans. To monitor and control these  
10 devices, each rack has an 1U rack-mount enclosure containing an ARM-based single-board com-  
11 puter (SBC) running Linux. An off-the-shelf GESBC-9G20 from Glomation Inc. [90] is utilized  
12 for the SBC. A custom interface board [91] connects the SBC to front panel LEDs, temperature  
13 probes, fan packs, and rack-protection-status input. The temperature sensors are DS1621 chips,  
14 controlled and read out over an I2C bus by the SBC’s I2C controller. The DS1621 also has a ther-  
15 mostat output with programmable trip and reset temperatures, which are connected via the interface  
16 board to outputs that can be used to interlock devices in the racks, such as power supplies. The fans  
17 provide pulse-per-rotation outputs, which are monitored by a 12-channel tachometer implemented  
18 via a PIC16F887 microcontroller, and also read out by the I2C bus. An EPICS IOC runs in each  
19 SBC, with custom device drivers for reading all status information and controlling the heartbeat  
20 LED and temperature sensor trip and reset points.

21 Data are imported into EPICS channels from a number of external sources. The primary rea-  
22 son for duplicating these data in EPICS is to integrate displays and warnings into one system for  
23 the experiment operators, and to provide integrated archiving for sampled data in the archived  
24 database. An IOC running on a central computer provides “soft” process-variables channels for  
25 these data. The data acquisition system provides many metrics describing its operation via the  
26 Ganglia system[92, 93], which makes the data available in an XML format easily read by a Python  
27 script, which in turn writes to EPICS using the PyEPICS module [94]. The hardware and sys-  
28 tem status of the DAQ computers is monitored through the industry standard Intelligent Platform  
29 Management Interface (IPMI); rather than writing a script to import data from IPMI directly into  
30 EPICS, a IPMI-to-Ganglia interface provided by the FreeIPMI’s “ipmi-sensors” package [95] is  
31 used, allowing data to be imported via the same mechanism used for the DAQ metrics. Separate  
32 Python scripts periodically retrieve data about outside weather conditions from various sources,  
33 cryogenics system data from a file retrieved non-intrusively from the IFIX cryogenics control sys-  
34 tem, and beam data from Fermilab’s Intensity Frontier Beam Database (IFDB) [96]. It should be  
35 noted that there is also a separate process that integrates pulse-by-pulse beam data with detector  
36 data.

### 37 **7.3 Beam Monitoring**

38 The primary source of neutrinos for the MicroBooNE experiment is the BNB. The primary beam-  
39 line is lined with instrumentation including toroids which indicate beam intensity, “multiwires”  
40 showing beam profile in the horizontal and vertical planes, and beam position monitors measuring  
41 the mean beam position. Data from these monitors are stored on a spill-by-spill basis in the IFDB.

1 Many of MicroBooNE's physics analyses require that beam data are recorded for each spill and  
2 matched to detector events.

3 Primary beam monitoring in MicroBooNE is done using a "dashboard" interface to IFDB.  
4 By using the IFBD instead of the accelerator control system, the experiment can also verify that  
5 data are being acquired by the IFBD. The dashboard is accessible over the network using a web  
6 browser. The final monitoring step includes a post-data-merge check, ensuring that beam data are  
7 successfully matched with detector data for all beam spills. This is done once the detector DAQ  
8 binary data file is closed.

9 The dashboard presents a graphic representation of the data, allowing for easy error identifica-  
10 tion, as shown in figure 70. The experiment monitors: two toroids which indicate beam intensity;  
11 three multiwires, each of which shows beam profile in each plane; and beam position monitors  
12 along the beamline which show the vertical and the horizontal position. Parameters pertaining to  
13 the target and horn, such as cooling air temperature and horn current, can also be monitored. The  
14 dashboard allows the experiment to easily add additional devices if experience demonstrates the  
15 need for their monitoring.

16 Data are monitored in near real-time. A reasonable history is also kept so that changes are  
17 easily identified. The accelerator control system provides detailed diagnostics tools to experts and  
18 can be used in case of any problems.

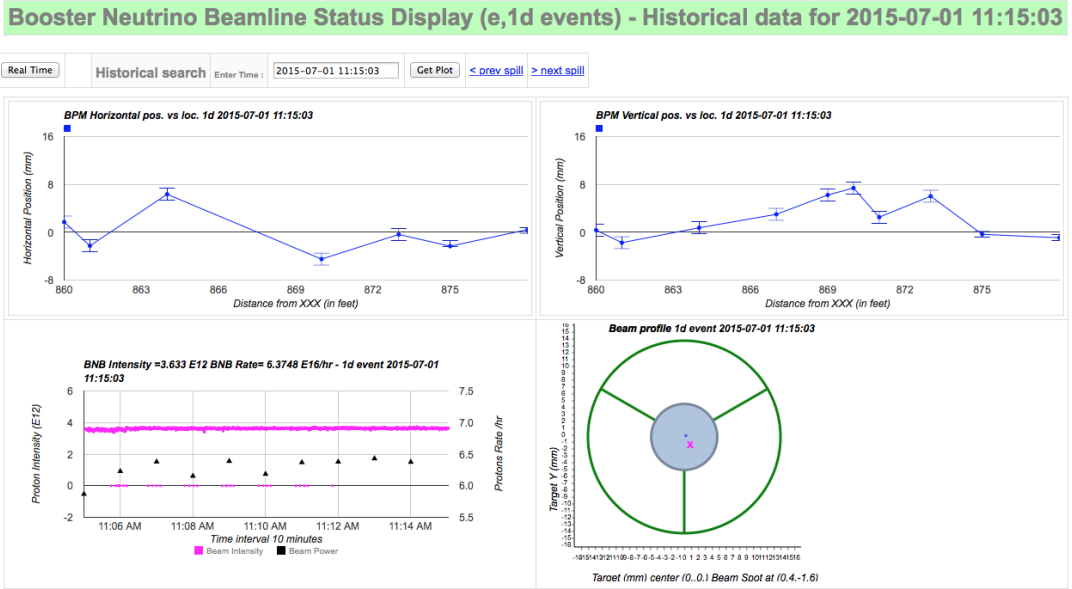


Figure 70: The BNB dashboard, showing graphical representation of beam instrumentation data, is used to monitor the beam. The top box shows the timestamp of the beam spill and indicates if data is stale by changing the color. The two top plots show the primary proton beam position along the BNB. The bottom left plot shows the recent beam spill intensity and rate. The bottom right plot shows the beam as projected onto the Beryllium target (the grey circle in the middle with radius of 0.5cm). The dashboard is accessible via web page providing both real time updates and the review of past data. The page can be easily extended to monitor additional beam devices.

## 8. UV Laser System

The knowledge of the electric field inside the drift volume of a LArTPC is a necessary aspect for performing subsequent event reconstruction. Distortions of particle tracks due to field non-uniformities affect the accuracy of the particle momentum reconstruction based on multiple scattering. Deviations from a uniform drift field may arise mainly due to accumulation of positive argon ions in the drift volume. These ions are produced by ionizing particles from neutrino interactions, as well as by cosmic rays. While electrons produced by ionizing particles are quickly (within few milliseconds) swept towards the readout system, ions have significantly lower mobility. Their drift velocity in the MicroBooNE detector at nominal drift field is of the order of 0.8 cm/s. The rate of cosmic muons in the LArTPC volume is estimated to be 11,000 muons/s within the active volume (assuming a cosmic rate of 200 muons/m<sup>2</sup>/s through a horizontal plane at the earth's surface and 63 muons/m<sup>2</sup>/s through a vertical plane), traversing a combined length of  $1.9 \times 10^4$  m through the liquid argon. Assuming that cosmic muons are minimum-ionizing (2.1 MeV/cm) and produce 23.6 eV per ion pair, positive ion charge is produced at a rate of  $2.8 \times 10^{-8}$  C/s in the MicroBooNE TPC. These ions are continuously neutralized at the cathode. The resulting charge distribution in equilibrium is shown in figure 71. Such accumulated space charge leads to noticeable distortion of the drift field and, consequently, to deviations of reconstructed track coordinates by up to 10cm (see figure 72). The ion drift velocity is comparable to local argon flow velocities, produced by global argon recirculation flow and thermal convection. Therefore the distribution of positive space charge inside the drift volume may be not only nonuniform (figure 73), but also non-stationary.

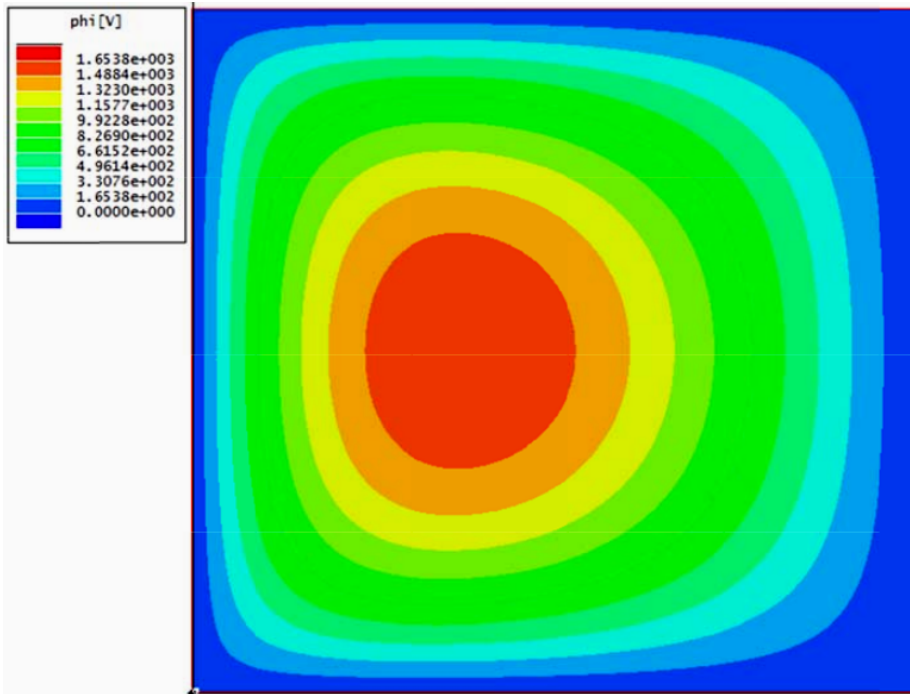


Figure 71: Distorting potential distribution due to positive space charge in equilibrium in the MicroBooNE detector.

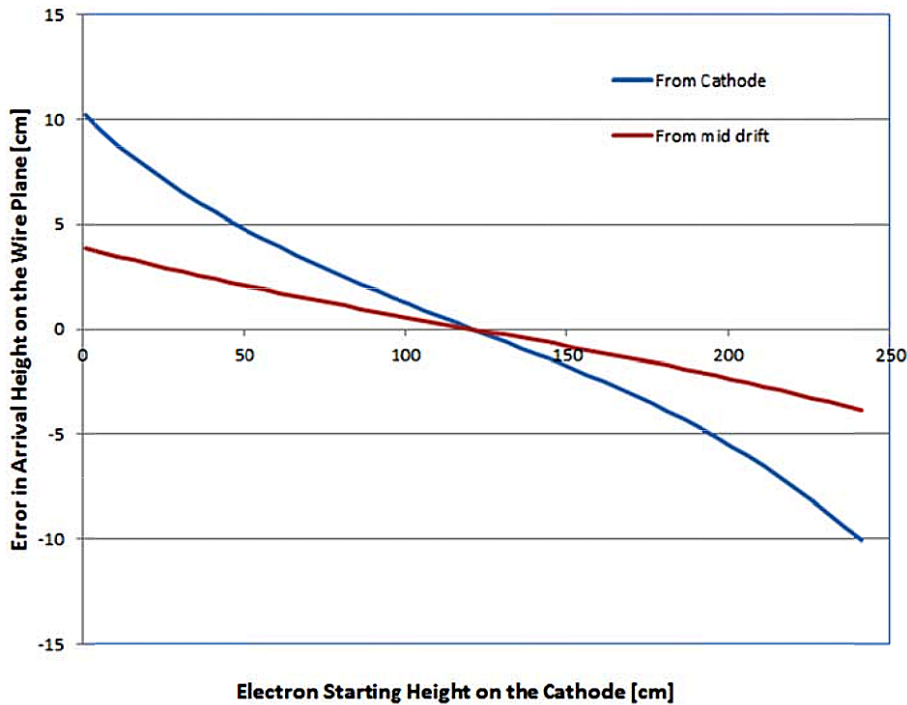


Figure 72: Deviation of a crossing track from its true coordinates due to positive ion space charge.

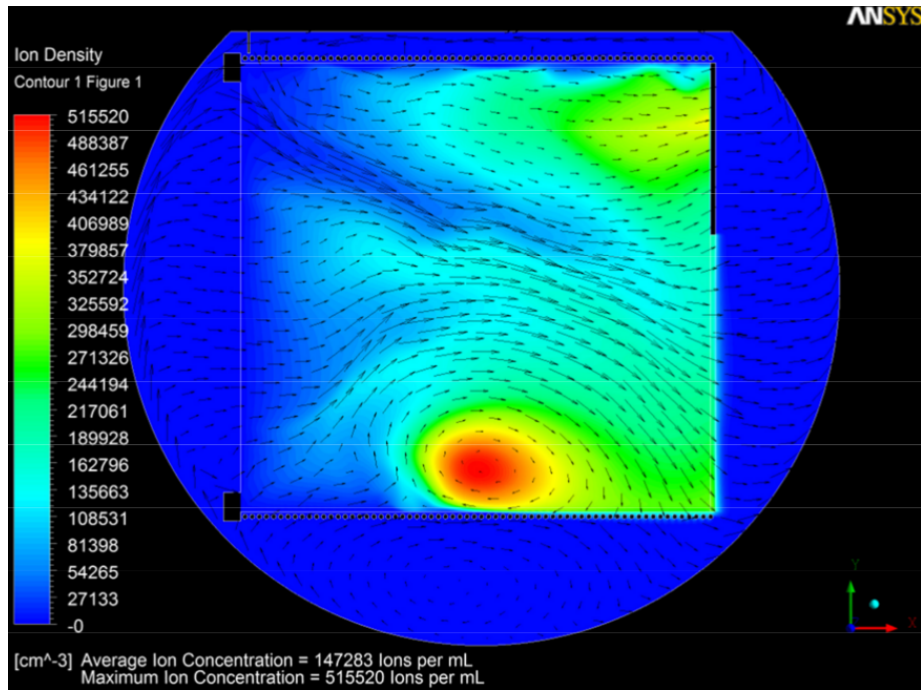


Figure 73: Distribution of the positive space charge in presence of argon circulation.

1      A nonuniform drift field in the LArTPC leads to bending of initially straight tracks of high-  
2      momentum ionizing particles. In principle, a set of events from such particles allows for the re-

1 construction of the field in any small region of the LArTPC drift volume, using the systematic  
2 apparent curvature of tracks at different angles passing through that region. In practice, the rate  
3 of such events from cosmic muons is too low to acquire sufficient statistics in reasonable time. A  
4 method to generate straight ionization tracks at a defined location in liquid argon is described in  
5 [97]. A collimated photon beam from a pulsed UV laser with  $\lambda=266$  nm can ionize liquid argon  
6 via multi-photon absorption. The resulting ionization track is straight, characterized by low elec-  
7 tron density, therefore featuring little charge recombination loss, unlike cosmic muon tracks. Laser  
8 tracks are also free from  $\delta$ -electrons, which complicate track reconstruction in the case of muons.  
9 The method was successfully exploited in the Argontube long drift LArTPC [25 – 27] to derive the  
10 non-uniformity of the electric field along its 5 m long drift volume (see [98]). The MicroBooNE  
11 LArTPC requires a set of such tracks in order to cover the whole sensitive volume to reconstruct  
12 field distortions. Tracks are generated one at a time by steering a pulsed laser beam with the use of  
13 a custom-designed opto-mechanical feedthrough (see [99]). The pulse rate of the laser generator is  
14 10 Hz. This allows production of a minimum required set of 100 tracks within one minute (taking  
15 into account steering time). Details of this solution are described in the following sections.

### 16 **8.1 UV Laser Calibration**

17 In order to unambiguously reconstruct a drift field vector at any point within the detector fiducial  
18 volume, a minimum of two ionization tracks are required to cross in the region of interest. The  
19 total number of crossing points is determined by the required reconstruction granularity. In Micro-  
20 BooNE the initial scenario is to acquire 100 tracks from each direction, producing a reconstructed  
21 3-D map with voxels that are approximately  $10 \times 10 \times 50$  cm<sup>3</sup> in volume. This map provides a rough  
22 picture of the space charge distribution. Depending on the results of this measurement, areas of  
23 interest can be studied in more detail. Repetitive study of small volumes may reveal dynamics in  
24 the space charge distribution due to turbulent circulation, and should further inform an optimized  
25 scenario for a standard UV laser calibration procedure.

26 An algorithm of drift field calibration utilizes an input array of detector events with one straight  
27 ionization track in each element of the array. The result of the calibration is a coordinate correction  
28 map, to be applied to each track, which converts apparently curved track images back to the true  
29 coordinate system where they are straight. The algorithm is iterative with an optimizable iteration  
30 step and required accuracy. An example of simulated reconstruction in 2-D space is depicted in  
31 figure 74, showing that the magnitude of the field distortions is reduced from 10 cm down to several  
32 millimeters in 99% of the detector volume.

### 33 **8.2 Laser Source and Optics**

34 A Nd:YAG laser emitting light at a wavelength of 1024 nm is used as the primary light source  
35 [?]. Inside the laser head, nonlinear crystals are installed in the beam line for frequency doubling  
36 and summing, resulting in a wavelength of 266 nm needed for ionization of liquid argon. For this  
37 wavelength, the Nd:YAG laser is specified to produce an output energy of 60 mJ for each 4 to 6 ns  
38 long pulse and a horizontal polarization. The maximal repetition rate is 10 Hz; the beam has a  
39 divergence of 0.5 mrad.

40 An optical table, as seen in figure 75, was developed to introduce the necessary parts in a  
41 stable and compact environment. With regard to the operation of the optical table on MicroBooNE,

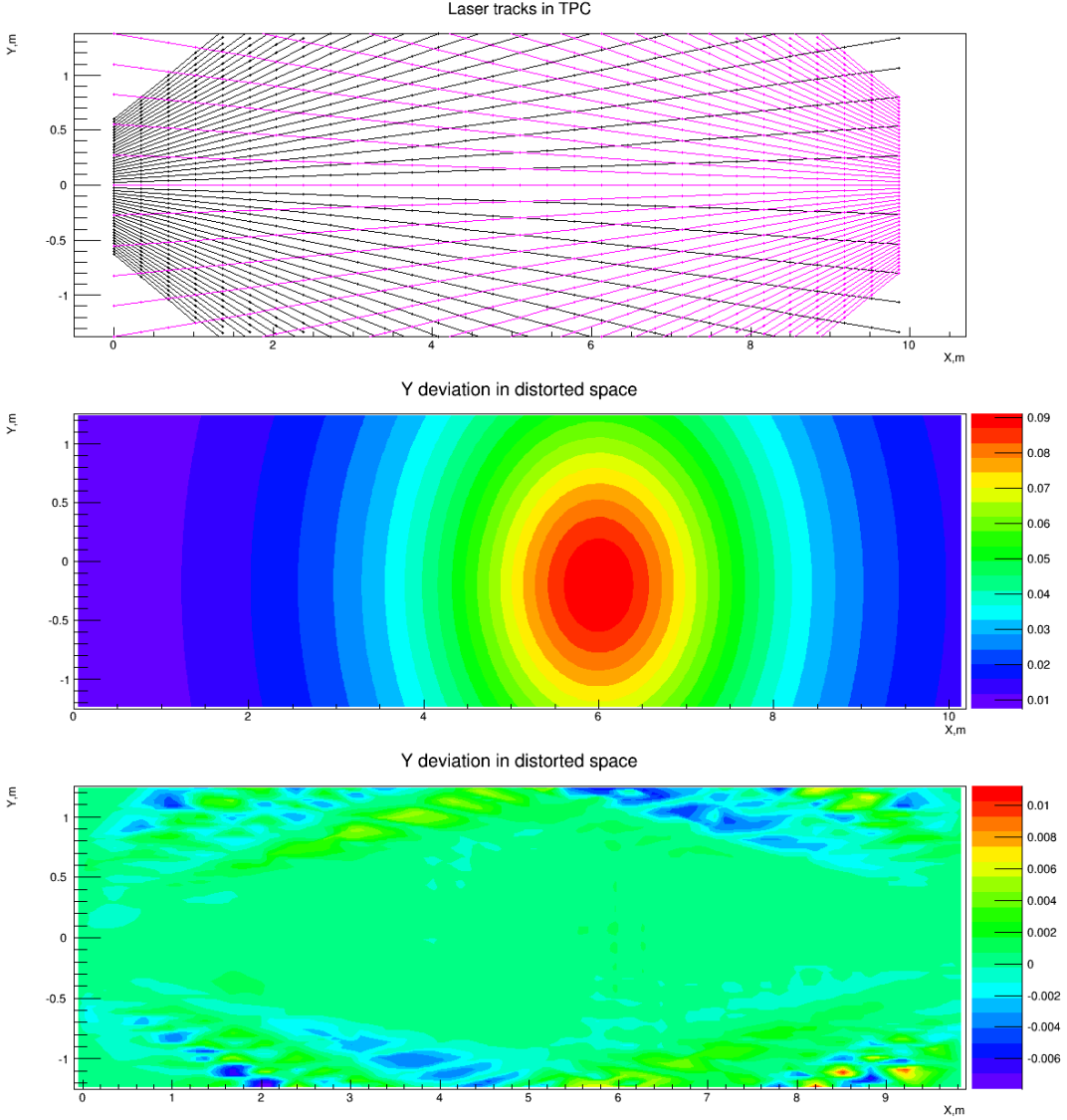


Figure 74: Top: Simulated true laser beam trajectories in the detector; Middle: map of Y coordinate of track deviation under influence of non-uniform electric field; Bottom: residual map of reconstructed track Y-coordinates versus true ones.

the parts were chosen to be accessible remotely where necessary. The emitted laser beam contains not only ultraviolet light but also all other harmonics generated in the crystal and the primary light of 1024 nm. Dichroic Mirrors optimized to reflect only wavelengths in the UV region are used to filter higher wavelengths out. To absorb the transmitted wavelength behind the mirrors, glass-ceramic plates are installed. The beam leaving the laser head is reflected by the first  $45^\circ$ -mirror into an attenuator. For optical adjustment and verification of the non-visible UV-beam, a green alignment laser is placed behind this mirror and adjusted such that its path is coincident with the UV-laser beam. In the attenuator (Altechna Wattpilot) a turnable  $\lambda/2$ -plate enables rotation of the orientation of the laser beam polarization. Behind the attenuator two parallel plates are installed

such that the angle of the incident beam matches the Brewster angle of the reflector. Modulating the polarization of the beam adjusts the intensity of the reflected beam. After the attenuator an aperture is put in the optical path of the beam to control the beam diameter. The last part in the beam line is a remotely-controllable mirror mount (Zaber T-OMG), which directs the beam to the laser feedthrough on the cryostat. A photodiode (Thorlabs DET10A/M), which is sensitive in the ultraviolet region, detects the scattered light when a laser pulse is fired. Its signal is then used as a trigger for data taking. Both the UV-laser head and the optical table are mounted on a 15 mm thick aluminum plate.

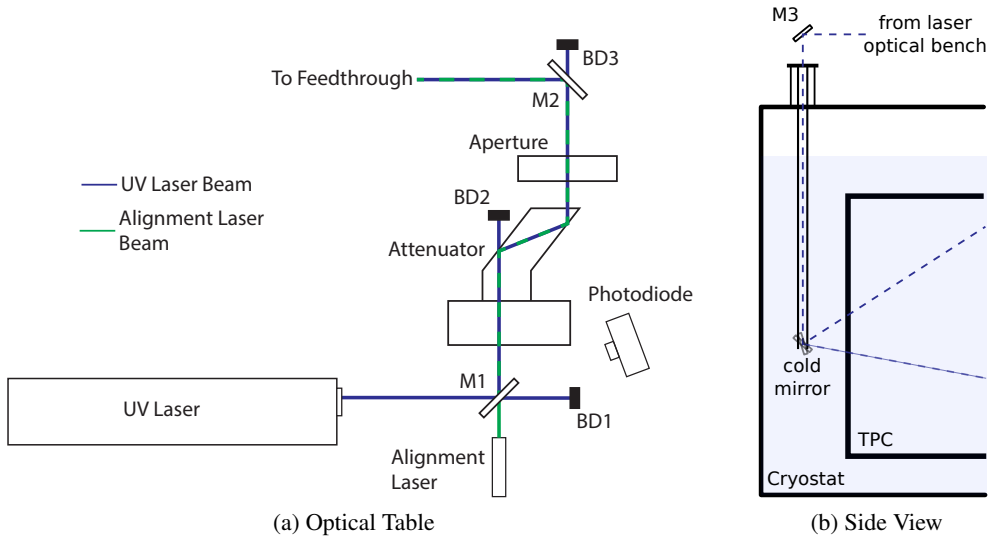


Figure 75: (a) A schematic drawing (not to scale) of the components used for laser beam configuration. An alignment laser (visible light) is introduced along the UV-laser path at the first dichroic mirror (M1), such that the paths overlap. In the attenuator the UV-laser beam intensity can be adjusted to the desired level, and the diameter of the beam is controlled by an aperture. A motorized mirror (M2) deflects the light into the direction of the feedthrough. Beam dumps (BD) are installed behind all mirrors to absorb the non-reflected laser light. (b) Side view of the cryostat indicating the mirror support structure with respect to the LArTPC.

### 8.3 Steering System

One of the main challenges of the laser calibration system is the introduction of a steerable laser beam into the detector. Earlier, an evacuated quartz-glass [100] was utilized to introduce a laser beam into liquid argon, however this beam had a fixed path through the detector. For the purpose of scanning the full detector a fully steerable mirror in liquid argon is necessary. In the MicroBooNE detector, this is achieved by mounting a mirror on a horizontally-rotatable support structure. A rack and pinion construction, where the mirror is mounted on the frontside of a half gear (pinion), provides the necessary freedom for the vertical movement (see figure 76 right). To steer the horizontal movement from outside the cryostat, a commercial differentially-pumped rotational feedthrough is deployed (see figure 76 left). The rack and pinion construction is attached to a linear feedthrough. Both feedthroughs are motorized to allow for remote control and automation of the

1 mirror movement. The mirror support structure was fabricated out of polyamide-imide (Duratron  
 2 T4301 PAI), which has a very low outgassing rate and low thermal expansion coefficient, and is  
 3 certified for operation at 87 K. To minimize the probability of discharges due to the close loca-  
 4 tion of the feedthrough to the field cage structure in MicroBooNE, no conductive parts were used  
 5 in the support structure. The support structure has a total length of 2.5 m in MicroBooNE. Both  
 6 feedthroughs are equipped with high precision position encoders from Heidenhain. The accuracy  
 7 of the encoders is chosen such that a position accuracy of 2 mm for the laser beam spot over 10 m  
 8 distance is achieved. An external interface box controls the encoders and records a position reading  
 9 upon receiving a trigger signal from the photodiode. The DAQ computer accesses the position in-  
 10 formation over an ethernet connection. The same computer is also used for steering the two motors  
 11 via a motor driver system (over a RS232 interface).

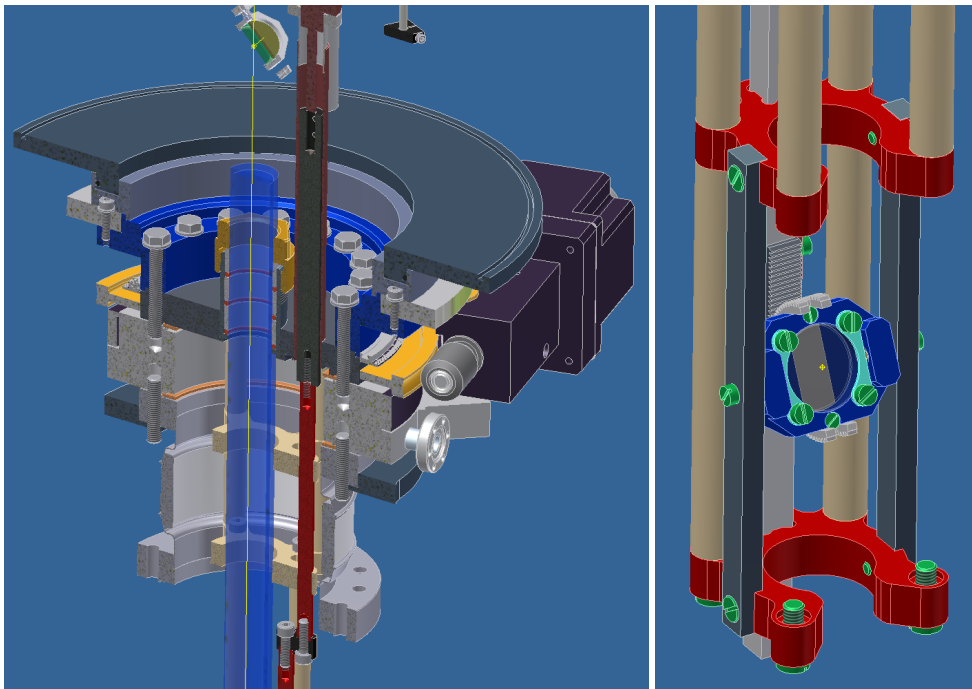


Figure 76: Left: CAD cutaway drawing of the feedthrough construction is shown. The yellow line indicates the laser path. Right, CAD drawing of the cold mirror including the support structure.

#### 12 **8.4 Performance Tests and Initial Operation**

13 A full performance test of the laser calibration system identical to the one installed in the Micro-  
 14 BooNE LArTPC was performed prior to the final installation. Apart from the general proof-of-  
 15 principle of the laser calibration system, several operationally relevant parameters were identified.  
 16 These include scanning speed, positioning accuracy, positioning limits, optimal laser beam inten-  
 17 sity, beam diameter, and the minimal achievable field distortion which can be resolved. The test  
 18 system consists of a LArTPC equipped with 64 readout channels and an active area of about 400  
 19  $cm^2$ , with a drift distance of 40 cm (see [101] for further details).

1 Several tests of the motorized feedthrough were performed under warm conditions before cold  
2 tests were conducted. One crucial parameter for the quality of the electric field calibration is the  
3 resolution at which laser tracks can be aimed in the detector. For the rotational axis this angle  
4 is directly measured on a circular scale. For the vertical movement the linear displacement of  
5 the bellow is translated into a rotation inside the cryostat, as can be seen in the CAD drawing in  
6 figure 76. This construction introduces uncertainties to the measurement position and backlash.  
7 The backlash can be compensated by always approaching positions from the same direction. For  
8 the translation of the linear movement  $\Delta L$  into a rotation  $\Delta\phi$  the translation ratio  $s$  according to  
9  $\Delta L = s \cdot \Delta\phi$  was measured with a laser alignment device<sup>3</sup>. The obtained ratio is  $s = 0.3499 \pm$   
10  $0.0002 \text{ mm/}^\circ$ . The dominant uncertainty in the vertical position measurement is the accuracy  
11 of the encoder  $\sigma_{\text{linear}} = \pm 1 \mu\text{m}$ , which translates into a vertical rotation measurement accuracy  
12  $\sigma_{\text{vertical}} = 10.29''$ .

13 Horizontal movement limitations arise from the construction of the feedthrough system, namely  
14 the warm mirror support structure. This limit has its origins in the way of mounting the laser ta-  
15 ble relative to the feedthrough on the MicroBooNE cryostat. Vertically the mirror can be rotated  
16 more than  $45^\circ$  relative to the horizon in both directions. In an upward looking configuration, no  
17 limitations arise which would affect the coverage of the detector with the beam. A limit arises  
18 when the mirror faces the opposite downward direction, when properly aligned onto the centre of  
19 the mirror the laser diameter and the size of the mirror limits the achievable coverage. However  
20 slight misalignment will affect this limit, since the beam will not be in the optimal spot anymore.  
21 In warm tests an maximal downward angle of the beam of  $52.5^\circ$  with respect to the horizon was  
22 achieved. During the cold tests the horizontal movement speed was set to  $2.6 \text{ }^\circ/\text{s}$  and the vertical  
23 speed to  $1 \text{ }^\circ/\text{s}$ , horizontally an angle of  $81^\circ$  was covered and  $22^\circ$  vertically, respectively. Tests in  
24 warm of the fully expanded setup showed vibrations if to high speed was chosen. The vibrations  
25 are expected to be damped with a more stable fixation on the detector and the immersion of the  
26 setup in liquid argon.

27 Modulation of the beam energy with respect to the vertical alignment of the cold mirror was  
28 found to be crucial for obtaining sufficient ionization in the detector. Investigations showed that  
29 the reflectivity of the selected dielectric mirrors, which were optimized for  $45^\circ$  in air, are very  
30 sensitive to the angle of incidence in liquid argon. Therefore during a calibration run, the beam  
31 energy has to be controlled. The emitted UV-laser beam has a diameter of 6 mm and will spatially  
32 diverge during propagation. A beam with this diameter will produce an ionization signal larger  
33 than the wire spacing, which will limit the capabilities of the full system. With the aperture a small  
34 as possible diameter of the laser was selected to enter the detector. Measurements of the diameter  
35 were performed with thermal paper (used for thermal printing) on which the selected beam spot  
36 burns in. The minimal achieved diameter was 1 mm.

## 37 **9. Conclusion**

38 The MicroBooNE detector is the culmination of several years of development and construction. It  
39 is the largest LArTPC ever constructed in the U.S., and represents a major technological advance  
40 that future experiments will build upon.

---

<sup>3</sup>Bosch GPL3.

<sup>1</sup> **Acknowledgments**

<sup>2</sup> We gratefully acknowledge support from the National Science Foundation, the United States De-  
<sup>3</sup> partment of Energy, and the EU funding gods.

<sup>4</sup> **References**

- <sup>5</sup> [1] T. Doke, *A historical view on the r&d for liquid rare gas detectors*, *Nuclear Instruments and*  
<sup>6</sup> *Methods in Physics Research Section A* **327** (1993), no. 1 113 – 118.
- <sup>7</sup> [2] W. Willis and V. Radeka, *Liquid-argon ionization chambers as total-absorption detectors*, *Nuclear*  
<sup>8</sup> *Instruments and Methods* **120** (1974), no. 2 221 – 236.
- <sup>9</sup> [3] C. Rubbia, *The liquid-argon time projection chamber: A new concept for neutrino detectors*, EP  
<sup>10</sup> Internal Report 77-8, CERN, May, 1977.
- <sup>11</sup> [4] P. Benetti et al., *A three-ton liquid argon time projection chamber*, *Nuclear Instruments and Methods*  
<sup>12</sup> *in Physics Research Section A: Accelerators, Spectrometers, Detectors and Associated Equipment*  
<sup>13</sup> **332** (1993), no. 3 395 – 412.
- <sup>14</sup> [5] P. Cennini et al., *Performance of a three-ton liquid argon time projection chamber*, *Nuclear*  
<sup>15</sup> *Instruments and Methods in Physics Research Section A: Accelerators, Spectrometers, Detectors*  
<sup>16</sup> *and Associated Equipment* **345** (1994), no. 2 230 – 243.
- <sup>17</sup> [6] F. Arneodo et al., *The ICARUS 50-l LAr TPC in the CERN ν beam*, hep-ex/9812006.
- <sup>18</sup> [7] S. Amerio et al., *Design, construction and tests of the ICARUS T600 detector*, *Nuclear Instruments*  
<sup>19</sup> *and Methods in Physics Research Section A: Accelerators, Spectrometers, Detectors and Associated*  
<sup>20</sup> *Equipment* **527** (2004), no. 3 329 – 410.
- <sup>21</sup> [8] S. Amoruso et al., *Measurement of the muon decay spectrum with the icarus liquid argon tpc*, *The*  
<sup>22</sup> *European Physical Journal C - Particles and Fields* **33** (2004), no. 2 233–241.
- <sup>23</sup> [9] S. Amoruso et al., *Study of electron recombination in liquid argon with the {ICARUS} {TPC}*,  
<sup>24</sup> *Nuclear Instruments and Methods in Physics Research Section A: Accelerators, Spectrometers,*  
<sup>25</sup> *Detectors and Associated Equipment* **523** (2004), no. 3 275 – 286.
- <sup>26</sup> [10] M. Antonello et al., *Detection of cherenkov light emission in liquid argon*, *Nuclear Instruments and*  
<sup>27</sup> *Methods in Physics Research Section A: Accelerators, Spectrometers, Detectors and Associated*  
<sup>28</sup> *Equipment* **516** (2004), no. 2–3 348 – 363.
- <sup>29</sup> [11] S. Amoruso et al., *Analysis of the liquid argon purity in the ICARUS T600 TPC*, *Nuclear Instruments*  
<sup>30</sup> *and Methods in Physics Research Section A: Accelerators, Spectrometers, Detectors and Associated*  
<sup>31</sup> *Equipment* **516** (2004), no. 1 68 – 79.
- <sup>32</sup> [12] F. Arneodo et al., *Observation of long ionizing tracks with the ICARUS T600 first half-module*,  
<sup>33</sup> *Nuclear Instruments and Methods in Physics Research Section A: Accelerators, Spectrometers,*  
<sup>34</sup> *Detectors and Associated Equipment* **508** (2003), no. 3 287 – 294.
- <sup>35</sup> [13] P. Aprili et al., *The ICARUS experiment: A second-generation proton decay experiment and neutrino*  
<sup>36</sup> *observatory at the gran sasso laboratory. cloning of t600 modules to reach the design sensitive mass.*  
<sup>37</sup> *(addendum)*, LNGS-EXP 13/89 add.2/01 CERN-SPSC-2002-027, CERN, 2002.

- 1 [14] D. B. Cline, J. G. Learned, K. McDonald, and F. Sergiampietri, *LANNDD—a massive liquid argon*  
 2 *detector for proton decay, supernova and solar neutrino studies and a neutrino factory detector*,  
 3 *Nuclear Instruments and Methods in Physics Research Section A: Accelerators, Spectrometers,*  
 4 *Detectors and Associated Equipment* **503** (2003), no. 1–2 136 – 140. Proceedings of the 3rd  
 5 International Workshop on Neutrino Factories based on Muon Storage Rings.
- 6 [15] A. Rubbia, *Experiments for CP violation: A Giant liquid argon scintillation, Cerenkov and charge*  
 7 *imaging experiment?*, hep-ph/0402110.
- 8 [16] A. Rubbia, *Underground Neutrino Detectors for Particle and Astroparticle Science: The Giant*  
 9 *Liquid Argon Charge Imaging ExpeRiment (GLACIER)*, *J.Phys.Conf.Ser.* **171** (2009) 012020,  
 10 [arXiv:0908.1286].
- 11 [17] **LAGUNA** Collaboration. <http://laguna.ethz.ch/LAGUNA/Welcome.html>.
- 12 [18] A. Stahl et al., *Expression of Interest for a very long baseline neutrino oscillation experiment*  
 13 (*LBNO*), Tech. Rep. CERN-SPSC-2012-021. SPSC-EOI-007, CERN, Geneva, Jun, 2012.
- 14 [19] S. Agarwalla et al., *The mass-hierarchy and CP-violation discovery reach of the LBNO*  
 15 *long-baseline neutrino experiment*, *JHEP* **1405** (2014) 094, [arXiv:1312.6520].
- 16 [20] “WA105.” <http://laguna.ethz.ch:8080/Plone/wa105>.
- 17 [21] C. Adams et al., *The Long-Baseline Neutrino Experiment: Exploring Fundamental Symmetries of*  
 18 *the Universe*, arXiv:1307.7335.
- 19 [22] A. Ereditato and A. Rubbia, *Ideas for future liquid argon detectors*, *Nucl.Phys.Proc.Suppl.* **139**  
 20 (2005) 301–310, [hep-ph/0409143].
- 21 [23] A. Ereditato and A. Rubbia, *The Liquid Argon TPC: A Powerful detector for future neutrino*  
 22 *experiments and proton decay searches*, *Nucl.Phys.Proc.Suppl.* **154** (2006) 163–178,  
 23 [hep-ph/0509022].
- 24 [24] B. Rossi et al., *A Prototype liquid Argon Time Projection Chamber for the study of UV laser*  
 25 *multi-photonic ionization*, *JINST* **4** (2009) P07011, [arXiv:0906.3437].
- 26 [25] I. Badhrees et al., *Argontube: An R&D Liquid Argon Time Projection Chamber*, *JINST* **7** (2012)  
 27 C02011.
- 28 [26] A. Ereditato et al., *Design and operation of ARGONTUBE: a 5 m long drift liquid argon TPC*, *JINST*  
 29 **8** (2013) P07002, [arXiv:1304.6961].
- 30 [27] M. Zeller et al., *First measurements with ARGONTUBE, a 5m long drift Liquid Argon TPC*,  
 31 *Nucl.Instrum.Meth.* **A718** (2013) 454–458.
- 32 [28] S. Horikawa et al., *Feasibility of high-voltage systems for a very long drift in liquid argon TPCs*,  
 33 *J.Phys.Conf.Ser.* **308** (2011) 012027, [arXiv:1009.4908].
- 34 [29] A. Badertscher et al., *First operation of a double phase LAr large electron multiplier time projection*  
 35 *chamber with a 2d projective readout anode*, *Nuclear Instruments and Methods in Physics Research*  
 36 *Section A: Accelerators, Spectrometers, Detectors and Associated Equipment* **641** (2011), no. 1 48 –  
 37 57.
- 38 [30] A. Badertscher et al., *First operation and drift field performance of a large area double phase LAr*  
 39 *Electron Multiplier Time Projection Chamber with an immersed Greinacher high-voltage multiplier*,  
 40 *JINST* **7** (2012) P08026, [arXiv:1204.3530].

- 1 [31] C. Cantini et al., *Long-term operation of a double phase LAr LEM Time Projection Chamber with a*  
 2 *simplified anode and extraction-grid design*, *JINST* **9** (2014) P03017, [[arXiv:1312.6487](#)].
- 3 [32] B. Baller et al., *Liquid Argon Time Projection Chamber Research and Development in the United*  
 4 *States*, *JINST* **9** (2013) T05005, [[arXiv:1307.8166](#)].
- 5 [33] C. Anderson et al., *The ArgoNeuT Detector in the NuMI Low-Energy beam line at Fermilab*, *JINST* **7**  
 6 (2012) P10019, [[arXiv:1205.6747](#)].
- 7 [34] R. Acciarri et al., *A study of electron recombination using highly ionizing particles in the ArgoNeuT*  
 8 *Liquid Argon TPC*, *JINST* **8** (2013) P08005, [[arXiv:1306.1712](#)].
- 9 [35] C. Anderson et al., *First Measurements of Inclusive Muon Neutrino Charged Current Differential*  
 10 *Cross Sections on Argon*, *Phys.Rev.Lett.* **108** (2012) 161802, [[arXiv:1111.0103](#)].
- 11 [36] R. Acciarri et al., *Measurements of Inclusive Muon Neutrino and Antineutrino Charged Current*  
 12 *Differential Cross Sections on Argon in the NuMI Antineutrino Beam*, *Phys.Rev.* **D89** (2014) 112003,  
 13 [[arXiv:1404.4809](#)].
- 14 [37] R. Acciarri et al., *First Measurement of Neutrino and Antineutrino Coherent Charged Pion*  
 15 *Production on Argon*, [arXiv:1408.0598](#).
- 16 [38] R. Acciarri et al., *LArIAT: Liquid Argon In A Testbeam*, [arXiv:1406.5560](#).
- 17 [39] A. Szeli, *The LArIAT light readout system*, *JINST* **8** (2013) C09011.
- 18 [40] M. Adamowski et al., *The Liquid Argon Purity Demonstrator*, *JINST* **9** (2014) P07005,  
 19 [[arXiv:1403.7236](#)].
- 20 [41] B. Rebel et al., *Results from the Fermilab materials test stand and status of the liquid argon purity*  
 21 *demonstrator*, *J.Phys.Conf.Ser.* **308** (2011) 012023.
- 22 [42] D. Montanari et al., *First scientific application of the membrane cryostat technology.*, .
- 23 [43] **HEPAP Subcommittee** Collaboration, S. Ritz et al., *Building for Discovery: Strategic Plan for U.S.*  
 24 *Particle Physics in the Global Context*, .
- 25 [44] A. Marchionni, *Status and New Ideas Regarding Liquid Argon Detectors*, *Ann.Rev.Nucl.Part.Sci.* **63**  
 26 (2013) 269–290, [[arXiv:1307.6918](#)].
- 27 [45] **MiniBooNE** Collaboration, A. Aguilar-Arevalo et al., *The Neutrino Flux prediction at MiniBooNE*,  
 28 *Phys.Rev.* **D79** (2009) 072002, [[arXiv:0806.1449](#)].
- 29 [46] E. Aprile, K. Giboni, and C. Rubbia, *A study of ionization electrons drifting large distances in liquid*  
 30 *and solid argon*, *Nuclear Instruments and Methods in Physics Research Section A: Accelerators,*  
 31 *Spectrometers, Detectors and Associated Equipment* **241** (1985), no. 1 62 – 71.
- 32 [47] B. Jones, C. Chiu, J. Conrad, C. Ignarra, T. Katori, et al., *A Measurement of the Absorption of Liquid*  
 33 *Argon Scintillation Light by Dissolved Nitrogen at the Part-Per-Million Level*, *JINST* **8** (2013)  
 34 P07011, [[arXiv:1306.4605](#)].
- 35 [48] Barber-Nichols Inc., 6325 West 55th Avenue, Arvada, CO 80002 USA.
- 36 [49] Sigma-Aldrich, P.O. Box 14508, St. Louis, MO 63178 USA.
- 37 [50] BASF Corp., 100 Park Avenue, Florham Park, NJ 07932 USA.
- 38 [51] Aspen Aerogels, Inc., 30 Forbes Road, Building B, Northborough, MA 01532 USA.

- 1 [52] G. Carugno et al., *Electron lifetime detector for liquid argon*, *Nuclear Instruments and Methods in*  
 2 *Physics Research Section A: Accelerators, Spectrometers, Detectors and Associated Equipment* **292**  
 3 (1990) 580.
- 4 [53] *Citranox acid detergent*, .  
 5 [http://www.alconox.com/resources/StandardDocuments/MSDS/msds\\_citranox\\_english\\_ghs.pdf](http://www.alconox.com/resources/StandardDocuments/MSDS/msds_citranox_english_ghs.pdf).
- 6 [54] *Simple Green detergent*, . [http://simplegreen.com/pdfs/MSDS\\_EN-US\\_AllPurposeCleaner.pdf](http://simplegreen.com/pdfs/MSDS_EN-US_AllPurposeCleaner.pdf).
- 7 [55] **MicroBooNE** Collaboration, T. Katori, *The MicroBooNE light collection system*, *JINST* **8** (2013)  
 8 C10011, [[arXiv:1307.5256](https://arxiv.org/abs/1307.5256)].
- 9 [56] L. Bugel, J. M. Conrad, C. Ignarra, B. J. P. Jones, T. Katori, T. Smidt, and H. K. Tanaka,  
 10 *Demonstration of a Lightguide Detector for Liquid Argon TPCs*, *Nucl. Instrum. Meth. A* **640** (2011)  
 11 69–75, [[arXiv:1101.3013](https://arxiv.org/abs/1101.3013)].
- 12 [57] **MicroBooNE** Collaboration, T. Katori, *MicroBooNE, A Liquid Argon Time Projection Chamber*  
 13 (*LArTPC*) *Neutrino Experiment*, *AIP Conf. Proc.* **1405** (2011) 250–255, [[arXiv:1107.5112](https://arxiv.org/abs/1107.5112)].
- 14 [58] T. Briese, L. Bugel, J. Conrad, M. Fournier, C. Ignarra, et al., *Testing of Cryogenic Photomultiplier*  
 15 *Tubes for the MicroBooNE Experiment*, *JINST* **8** (2013) T07005, [[arXiv:1304.0821](https://arxiv.org/abs/1304.0821)].
- 16 [59] B. Jones, T. Alexander, H. Back, G. Collin, J. Conrad, et al., *The Effects of Dissolved Methane upon*  
 17 *Liquid Argon Scintillation Light*, *JINST* **8** (2013) P12015, [[arXiv:1308.3658](https://arxiv.org/abs/1308.3658)].
- 18 [60] B. Baller, N. Buchanan, F. Cavanna, H. Chen, E. Church, et al., *Liquid Argon Time Projection*  
 19 *Chamber Research and Development in the United States*, *JINST* **9** (2014) T05005,  
 20 [[arXiv:1307.8166](https://arxiv.org/abs/1307.8166)].
- 21 [61] Z. Moss, L. Bugel, G. Collin, J. Conrad, B. Jones, et al., *Improved TPB-coated Light Guides for*  
 22 *Liquid Argon TPC Light Detection Systems*, [arXiv:1410.6256](https://arxiv.org/abs/1410.6256).
- 23 [62] **MicroBooNE** Collaboration, J. Conrad, B. Jones, Z. Moss, T. Strauss, and M. Toups, *The*  
 24 *Photomultiplier Tube Calibration System of the MicroBooNE Experiment*, *JINST* **10** (2015), no. 06  
 25 T06001, [[arXiv:1502.0415](https://arxiv.org/abs/1502.0415)].
- 26 [63] R. Acciarri, M. Adamowski, D. Artrip, B. Baller, C. Bromberg, et al., *Summary of the Second*  
 27 *Workshop on Liquid Argon Time Projection Chamber Research and Development in the United*  
 28 *States*, [arXiv:1504.0560](https://arxiv.org/abs/1504.0560).
- 29 [64] Z. Moss, M. Toups, L. Bugel, G. Collin, and J. Conrad, *Anode-Coupled Readout for Light Collection*  
 30 *in Liquid Argon TPCs*, [arXiv:1507.0199](https://arxiv.org/abs/1507.0199).
- 31 [65] Hamamatsu, “Large area photomultiplier tubes.” Specification for R5912 and R5912-02  
 32 photomultiplier tubes:  
 33 [http://www.hamamatsu.com/resources/pdf/etd/LARGE\\_AREA\\_PMT TPMH1286E05.pdf](http://www.hamamatsu.com/resources/pdf/etd/LARGE_AREA_PMT TPMH1286E05.pdf).
- 34 [66] E. H. Bellamy, G. Bellettini, F. Gervelli, M. Incagli, D. Lucchesi, C. Pagliarone, F. Zetti,  
 35 Yu. Budagov, I. Chirikov-Zorin, and S. Tokar, *Absolute calibration and monitoring of a*  
 36 *spectrometric channel using a photomultiplier*, *Nucl. Instrum. Meth. A* **339** (1994) 468–476.
- 37 [67] H. O. Meyer, *Dark Rate of a Photomultiplier at Cryogenic Temperatures*, [arXiv:0805.0771](https://arxiv.org/abs/0805.0771).
- 38 [68] H. Meyer, *Spontaneous electron emission from a cold surface*, *EPL* (2010), no. 89 58001.
- 39 [69] Hamamatsu Photonics, *Photomultiplier Tubes, Basics and Applications, Third Edition, Chapter*  
 40 *13.9*, . [https://www.hamamatsu.com/resources/pdf/etd/PMT\\_handbook\\_v3aE.pdf](https://www.hamamatsu.com/resources/pdf/etd/PMT_handbook_v3aE.pdf).

- 1 [70] W. Burton and B. Powell, *Fluorescence of tetraphenyl-butadiene in the vacuum ultraviolet.*, *Appl  
Opt.* **12** (1973), no. 1 87–9.
- 2 [71] C. Ignarra, “Sterile Neutrino Searches in MiniBooNE and MicroBooNE.” PhD Thesis - I would like  
a URL for this.
- 3 [72] V. Gehman, S. Seibert, K. Rielage, A. Hime, Y. Sun, et al., *Fluorescence Efficiency and Visible  
Re-emission Spectrum of Tetraphenyl Butadiene Films at Extreme Ultraviolet Wavelengths*,  
*Nucl.Instrum.Meth.* **A654** (2011) 116–121, [[arXiv:1104.3259](https://arxiv.org/abs/1104.3259)].
- 4 [73] R. Francini, R. Montereali, E. Nichelatti, M. Vincenti, N. Canci, et al., *VUV-Vis optical  
characterization of Tetraphenyl-butadiene films on glass and specular reflector substrates from room  
to liquid Argon temperature*, *JINST* **8** (2013) P09006.
- 5 [74] C. Chiu, C. Ignarra, L. Bugel, H. Chen, J. Conrad, et al., *Environmental Effects on TPB  
Wavelength-Shifting Coatings*, *JINST* **7** (2012) P07007, [[arXiv:1204.5762](https://arxiv.org/abs/1204.5762)].
- 6 [75] B. J. P. Jones, *A simulation of the optical attenuation of TPB coated light-guide detectors*, *JINST* **8**  
(2013) C10015, [[arXiv:1307.6906](https://arxiv.org/abs/1307.6906)].
- 7 [76] Sundance Supply, “Lexan Thermoclear Multiwall Polycarbonate Sheet.”  
<https://www.sundancesupply.com/Lexan.pdf>.
- 8 [77] B. Baptista, L. Bugel, C. Chiu, J. Conrad, C. Ignarra, et al., *Benchmarking TPB-coated Light Guides  
for Liquid Argon TPC Light Detection Systems*, [arXiv:1210.3793](https://arxiv.org/abs/1210.3793).
- 9 [78] J. B. Birks and K. N. Kuchela, *Energy transfer in fluorescent plastic solutions*, *Disc. Faraday. Soc* **27**  
(1959) 57–63.
- 10 [79] J. B. Birks and K. N. Kuchela, *Energy transfer in organic systems ii: Solute-solute transfer in liquid  
solutions*, *Proc. Phys.Soc* **77** (1961) 1083.
- 11 [80] S. Hanagodimath, B. Siddlingeshwar, J. Thipperudrappa, S. Kumar, and B. Hadimani,  
*Fluorescence-quenching studies and temperature dependence of fluorescence quantum yield, decay  
time and intersystem crossing activation energy of tpb*, *J. Lumin* **129** (2008), no. 4 335–339.
- 12 [81] L. Liu, “Time resolved fluorescence studies of dye-polymers as excited by laser and beta radiation.”  
PhD Thesis at Texas Tech University -  
<http://repositories.tdl.org/ttu-ir/bitstream/handle/2346/13744/31295012500558.pdf?sequence=1>.
- 13 [82] Hamamatsu, “Photomultipler tube r7723, r7724, r7725.”  
<http://www.hamamatsu.com/resources/pdf/etd/R7723 TPMH1315E01.pdf>.
- 14 [83] “Experimental physics and industrial control system.” <http://www.aps.anl.gov/epics/>.
- 15 [84] “Control system studio.” <http://controlsystemstudio.org/>; developer’s manual:  
<http://cs-studio.sourceforge.net/docbook/>.
- 16 [85] *Channel access protocol specification*, September, 2014. <http://www.aps.anl.gov/epics/docs/ca.php>.
- 17 [86] “Net-snmp.” <http://www.net-snmp.org>.
- 18 [87] J. Priller, *Epics snmp device support module: Release 1.0.0*, April, 2014.  
<https://groups.nscl.msu.edu/controls/>.
- 19 [88] M. Rivers, *asyndriver: Asynchronous driver support*, September, 2014.  
<http://www.aps.anl.gov/epics/modules/soft/async/>.

- 1 [89] D. Zimoch, *Epics streamdevice*, September, 2014.  
 2 http://epics.web.psi.ch/software/streamdevice/doc/.
- 3 [90] *Glomation, inc., gesbc-9g20 user's manual, version 0.2*, June, 2009.  
 4 http://www.glomationinc.com/GESBC-9G20-user-manual.pdf.
- 5 [91] D. Huffman, *Peripheral interface: Fan and temperature probe*, September, 2014.  
 6 http://www-ppd.fnal.gov/EEDOffice-W/Infrastructure\_group/Huffman/WEB/uboone/pia.html.
- 7 [92] M. Massie et al., *Monitoring with Ganglia: Tracking Dynamic Host and Application Metrics at Scale*. O'Reilly Media, 2012.
- 9 [93] *Ganglia*, September, 2014. http://ganglia.info/.
- 10 [94] M. Newville, *Pyepics: Epics channel access for python*, September, 2014.  
 11 http://cars9.uchicago.edu/software/python/pyepics3/.
- 12 [95] *Gnu freeipmi*, September, 2014. http://www.gnu.org/software/freeipmi/.
- 13 [96] I. Mandrichenko, A. Norman, A. Petrov, and V. Podstavkov, *Implementation of beam conditions database for intensity frontier experiments*, June, 2012.  
 14 http://cd-docdb.fnal.gov/cgi-bin>ShowDocument?docid=4781.
- 16 [97] I. Badhrees et al., *Measurement of the two-photon absorption cross-section of liquid argon with a time projection chamber*, *New J.Phys.* **12** (2010) 113024, [[arXiv:1011.6001](#)].
- 18 [98] A. Ereditato et al., *Measurement of the drift field in the ARGONTUBE LAr TPC with 266 nm pulsed laser beams*, [arXiv:1408.6635](#).
- 20 [99] A. Ereditato et al., *A steerable UV laser system for the calibration of liquid argon time projection chambers*, [arXiv:1406.6400](#).
- 22 [100] I. Badhrees, A. Ereditato, I. Kreslo, M. Messina, U. Moser, B. Rossi, M. S. Weber, M. Zeller,  
 23 C. Altucci, S. Amoruso, R. Buzzese, and R. Velotta, *Measurement of the two-photon absorption cross-section of liquid argon with a time projection chamber*, *New Journal of Physics* **12** (2010),  
 24 no. 11 113024.
- 26 [101] A. Ereditato, I. Kreslo, M. LÄijthi, C. R. von Rohr, M. Schenk, T. Strauss, M. Weber, and M. Zeller,  
 27 *A steerable uv laser system for the calibration of liquid argon time projection chambers*, *Journal of Instrumentation* **9** (2014), no. 11 T11007.